Draft version October 21, 2025
Typeset using LaTeX **twocolumn** style in AASTeX7.0.1

Unveiling Obscured Accretion in the Local Universe

I. Pal [1], S. Marchesi [2,1,3], R. Silver [4], M. Ajello [1], V. E. Gianolli [1], N. Torres-Albà [5], I. Cox [1], X. Zhao [6], D. Sengupta [7], A. Banerjee [1], K. Imam [1] and A. Pizzetti [8]

[1] Department of Physics and Astronomy, Clemson University, Kinard Lab of Physics, Clemson, SC 29634, USA
[2] Dipartimento di Fisica e Astronomia (DIFA), Università di Bologna, via Gobetti 93/2, I-40129 Bologna, Italy
[3] INAF - Osservatorio di Astrofisica e Scienza dello Spazio di Bologna, Via Piero Gobetti, 93/3, 40129, Bologna, Italy
[4] NASA Goddard Space Flight Center, Greenbelt, MD 20771, USA
[5] Department of Astronomy, University of Virginia, P.O. Box 400325, Charlottesville, VA 22904, USA
[6] Cahill Center for Astrophysics, California Institute of Technology, 1216 East California Boulevard, Pasadena, CA 91125, USA
[7] Center for Space Science and Technology, University of Maryland Baltimore County, 1000 Hilltop Circle, Baltimore, MD 21250, USA
[8] European Southern Observatory, Alonso de Còrdova 3107, Casilla 19, Santiago, 19001, Chile

ABSTRACT

Heavily obscured Active Galactic Nuclei (AGN), especially Compton-thick sources with line-of-sight column density ($N_{\rm H,los}$) $> 10^{24}$ cm^{-2}, are critical to understanding supermassive black hole (SMBH) growth and the origin of the Cosmic X-ray Background (CXB). However, their observed fraction remains significantly below model predictions, due to strong absorption bias, even in the hard X-ray (i.e., above 10 keV) band. We analyze a sample of 26 nearby ($z < 0.1$) AGN from the *Swift*-BAT 150-month catalog, selected via mid-IR to X-ray diagnostics and observed with *NuSTAR* and soft X-ray telescopes (XMM-*Newton*, *Chandra*, or *Swift*-XRT). Using self-consistent torus models (`MyTorus`, `Borus02`, and `UXCLUMPY`), we aim to constrain $N_{\rm H,los}$, the average torus column density, and other geometrical parameters of the obscuring medium. A comparative analysis among the three torus models showed that while estimates of $N_{\rm H,los}$ were generally in agreement, `Borus02` tended to classify a slightly larger number of sources as Compton-thick AGN (CT-AGN). Building on this comparison, we benchmark two prediction schemes – a mid-IR/X-ray relation and a machine-learning model – against our broadband best-fit $N_{\rm H,los}$ measurements to assess which approach more effectively bridges the gap between predicted and measured obscuration, finding that while the former works effectively in the heavily obscured region ($\log N_{\rm H} \gtrsim 23.5$ cm^{-2}), the latter provides improved accuracy, particularly for Compton-thin to moderately thick regimes ($\log N_{\rm H} \lesssim 23.5$ cm^{-2}).

Keywords: Active galaxies (17) — X-ray active galactic nuclei (2035) — High Energy astrophysics (739) — galaxy nuclei (609)

1. INTRODUCTION

Active Galactic Nuclei (AGN) are among the most luminous persistent sources in the Universe, with their integrated emission dominating the Cosmic X-ray Background (CXB) from 1 to $\sim$ 200–300 keV (Alexander et al. 2003; Gilli et al. 2007; Treister et al. 2009). A substantial share of CXB is expected to arise from heavily obscured AGN, in particular Compton-thick (CT-) systems with the line-of-sight (los) column density ($N_{\rm H,los}$) $\gtrsim 10^{24}$ cm^{-2} (Ueda et al. 2014; Buchner et al. 2015). While unobscured AGN dominate the CXB below $\sim$10 keV and are largely resolved, only a small fraction of the emission near the CXB peak at $\sim$ 30 keV has been directly attributed to discrete sources (Ajello et al. 2008). Population-synthesis models therefore require a sizable, still-hidden Compton-thick population of order $\sim$ 30-50% of all AGN to reproduce both the shape and normalization of the CXB (Gilli et al. 2007; Ananna et al. 2019). In contrast, observational estimates in the local Universe find markedly lower CT fractions, typically $\sim$ 5-35% (e.g., Burlon et al. 2011; Ricci et al. 2015; Torres-Albà et al. 2021; Boorman et al. 2025), underscoring a persistent gap between models and data.

The shortfall is chiefly a selection problem: extreme photoelectric absorption and Compton scattering sup-

Email: ipal@clemson.edu, smarche@clemson.edu

press the nuclear signal from the optical through the hard X-ray bands, making CT-AGN intrinsically difficult to find even with high-energy instruments (Gilli et al. 2007; Ajello et al. 2008; Ananna et al. 2019). The obscurer – often dubbed the "dusty torus" – likely sits on parsec scales (Jaffe et al. 2004; Nenkova et al. 2008) and is clumpy and anisotropic rather than smooth (Elitzur & Shlosman 2006; Risaliti et al. 2007). In such geometries, modest changes in viewing angle or cloud statistics can shift sources across the Compton-thick boundary, diluting flux-limited samples and biasing traditional hardness-ratio or soft-X-ray selections. In this context, closing the observed-versus-predicted gap is thus necessary and it demands strategies that are less biased against obscuration. Accurately identifying and characterizing these obscured AGN is essential for tracing the full accretion history of SMBH and understanding the co-evolution of black holes and their host galaxies (Tombesi et al. 2015; Gaspari & Sądowski 2017).

To address the observational challenges of identifying and characterizing obscured AGN, various methods have been proposed for predicting column densities ($N_{\rm H}$) using indirect indicators. Traditional approaches rely on empirical correlations–such as mid-infrared (MIR) to X-ray flux ratios–to identify obscured sources. For example, Asmus et al. (2015) introduced a diagnostic based on WISE 12 μm to 2-10 keV flux ratios, which is effective for sources with $\log N_{\rm H} \gtrsim 23$, but less so for less obscured AGN. Improvements have been proposed using luminosity ratios (Pfeifle et al. 2022) and hard X-ray spectral curvature (Koss et al. 2016), yet these methods still suffer from limitations in accuracy and contamination. More recently, Silver et al. (2023) developed a machine learning (ML) model using multiple observational features, achieving high correlation with spectroscopically measured $N_{\rm H}$ and robust classification across obscuration regimes.

Despite these advancements, there has been limited systematic testing of predictive methods against detailed spectral modeling for well-defined AGN samples. Moreover, the physical interpretation of torus parameters such as covering fraction (c_f), $N_{\rm H,los}$, and the average torus column density ($N_{\rm H,avg}$) remains uncertain, particularly in terms of how they relate to one another and to source properties like luminosity and accretion rate.

This work presents a focused investigation aimed at exploring some of these open questions using a well-defined subset of nearby, obscured AGN. The sample is selected using the IR–to-X-ray flux criteria of Asmus et al. (2015), and is observed with the Nuclear Spectroscopic Telescope Array (*NuSTAR*; Harrison et al. 2013), which provides high-sensitivity coverage in the 3-79 keV band. This enables robust measurement of the Compton hump and intrinsic continuum components, essential for accurate determination of $N_{\rm H,los}$ and other torus properties (Brightman et al. 2015; Marchesi et al. 2019).

We evaluate the performance of IR–X-ray diagnostics and machine learning models in predicting $N_{\rm H}$ by comparing their outputs to values derived from high-quality X-ray spectral fitting. Additionally, we investigate possible correlations between torus parameters, including the covering fraction, $N_{\rm H,los}$, and $N_{\rm H,avg}$, to explore the structure and geometry of the obscuring material. We also test the relationship between the covering fraction and key AGN properties such as intrinsic 2–10 keV luminosity and Eddington ratio.

The manuscript is arranged as follows: the selection criteria and construction of the source sample are described in Section 2. Section 3 outlines the data reduction process, while Section 4 details the spectral modeling procedures. The results of the spectral fitting analysis are presented in Section 5. In Section 6, we compare the best-fit parameters obtained from different models, assess the agreement between predicted and measured $N_{\rm H}$ and examine correlations between torus properties. Finally, our findings and conclusions are summarized in Section 7. A description of the fit results and the tabulated fit parameters are outlined in Appendix A and Appendix B.

2. SAMPLE SELECTION

Our study focuses on a sample of 26 AGN at redshift $z < 0.1$, selected from the 150-month *Swift*-BAT catalog (Imam et al., submitted). These sources were chosen to represent obscured AGN candidates based on a set of well-defined criteria. First, each target is predicted to be significantly obscured, with line-of-sight column densities $N_{\rm H,los} > 10^{23}$ cm^{-2}, as inferred from the MIR to X-ray flux correlation established by Asmus et al. (2015). The details of the selected sources including their positions, type and predicted $N_{\rm H,los}$ values from Asmus et al. (2015) are given in Table 1. Second, all selected sources have at least one archival observation with *NuSTAR*, providing high-quality coverage in the 3-50 keV band. The log of observations are given in Table 2. The redshift distribution and the distribution of the selected sources with the predicted $N_{\rm H,los}$ values against the mid-IR to X-ray flux ratio as obtained from Asmus et al. (2015) are plotted in Fig. 1.

To complement the *NuSTAR* data and ensure broad energy coverage, we also associate each target with archival 0.5-10 keV observations from soft X-ray telescopes. When available, we prioritize data from XMM-*Newton*, due to its superior effective area. If XMM-

Newton data are unavailable, we include observations from *Chandra*, and when both XMM-*Newton*, and *Chandra* are unavailable, we incorporate data from *Swift*-XRT. Therefore, the dataset includes archival observations from several X-ray observatories spanning a few years, and thus, the spectra are generally non-simultaneous. To ensure consistency, we verified that the individual spectra have consistent shapes (see Section C, Fig. 14) and show only modest variability; we therefore fit them together with a standard set of inter-instrument cross-normalization constants, fixing one instrument to unity and allowing the others to vary (see Section 4). This multi-instrument approach allows us to construct high-quality, broadband (0.5-50 keV) spectra for each source, enabling a robust and self-consistent modeling of the obscuring material and its interaction with the AGN emission. We note that a systematic investigation of possible variations in $N_{\rm H,los}$ across different observations is not carried out in this work, as it lies beyond the scope of the present study; moreover, the available broad-band (0.5-50 keV) datasets are non-simultaneous for the majority of sources.

3. DATA REDUCTION

The log of all the observations analyzed in this work is provided in Table 2. The data reduction process is detailed in the following subsections.

3.1. *NuSTAR*

We reduced the *NuSTAR* data in the 3−79 keV band using the standard *NuSTAR* data reduction software NuSTARDAS[9] v0.4.12 distributed by HEASARC within HEASoft v6.34. The calibrated, cleaned, and screened event files were generated by running the `nupipeline` task using the CALDB release 20240405. To extract the source counts from both modules (FPMA and FPMB), we chose circular regions of radii between 40″ and 100″ centred on the source, depending on the observations, while requiring a minimum S/N of 4 per energy bin. Similarly, to extract the background counts, we selected a circular region of the same radius away from the source on the same chip to avoid contamination from source photons. We then used the `nuproducts` task to generate energy spectra, response matrix files (RMFs) and auxiliary response files (ARFs), for both the hard X-ray detectors housed inside the corresponding focal plane modules, FPMA and FPMB. The data from FPMA and FPMB are analyzed jointly, and they are not combined.

[9] https://heasarc.gsfc.nasa.gov/docs/nustar/analysis/nustar_swguide.pdf

3.2. *XMM-Newton*

We carried out our analysis with the data from the pn and MOS cameras (when available) (Strüder et al. 2001). We used SAS v1.3 for the data reduction (Gabriel et al. 2004). The event files were filtered to exclude background flares selected from time ranges where the 10-15 keV count rates in the PN camera exceeded 0.7 cts/s. The source spectra were extracted from a circular region with a radius between 30″ and 50″ centered on the nucleus. Background photons were selected from a source-free region of equal area on the same chip as the source. We checked for pileup using the `EPATPLOT` task. We did not find any of the sources that suffered from pileup. We constructed RMFs and ARFs using the tasks *RMFGEN* and *ARFGEN* for each observation.

3.3. *Chandra*

The *Chandra* (Weisskopf et al. 2000) data have been reduced using the CIAO 4.7 software and the *Chandra* Calibration Data Base (`caldb`) 4.6.9, adopting standard procedures; no source shows significant pile-up, as measured by the CIAO PILEUP_MAP tool. We used the CIAO `specextract` tool to extract both the source and the background spectra. Source spectra have been extracted in circular regions of 4″, while background spectra have been extracted from annuli having inner radius $r_{\rm int}$=10″ and outer radius $r_{\rm out}$=25″: regions inside the background area have been visually inspected to avoid contamination from nearby sources.

3.4. *Swift-XRT*

Eight sources in our sample (2MASX J09261742-8421330, MRK 376, NGC 7378, 2MASX J11462959+7421289, SWIFT J2006.5+5619, 2MASX J06363227-2034532, 2MASX J09034285-7414170, and 2MASX J00091156-0036551) have not been observed with either XMM-*Newton* or *Chandra*. For these sources, we used archival *Swift*-XRT(Burrows et al. 2005) observations from the Neil Gehrels Swift Observatory (Gehrels et al. 2004) taken simultaneously / quasi-simultaneously with the *NuSTAR*observations. In cases where multiple observations were obtained within a short time interval, the *Swift*-XRT data were combined to produce a single 0.5–10 keV spectrum, following standard procedures of the UK Swift Science Data Centre (Evans et al. 2009).

4. SPECTRAL FITTING PROCEDURE

The spectral fitting procedure is performed using the XSPEC software (Arnaud 1996); the Galactic absorption values are the one measured by Willingale et al. (2013). We use the solar abundances from Wilms et al.

Table 1. Properties of the 26 sources analyzed in this work. The columns are (1) serial number of the source, (2) name of the source, (3) right ascension (h:m:s), (4) declination (d:m:s), (5) redshift, (6) optical/near infrared classification of the source, (7) predicted $N_{\rm H,los}$ from Asmus et al. (2015), (8) predicted $N_{\rm H,los}$ from Silver et al. 2023 (9) black hole mass, and (10) Eddington ratio. Some of the information, including the right ascension, declination, z and type of the sources, are from SIMBAD[a]. Details regarding the black hole mass references can be found in Section A.

Index	**Name**	**RA**	**DEC**	**z**	**Type**	**Asmus log $N_{\rm H,los}$**	**ML log $N_{\rm H,los}$**	**log $\left(\frac{M_{BH}}{M_\odot}\right)$**	**log $\lambda_{\rm Edd}$**
		(h:m:s)	(d:m:s)			($\rm cm^{-2}$)	($\rm cm^{-2}$)		
1	MRK 1073	03 15 01.43	+42 02 08.82	0.023	Sy2	24.450	23.012	7.78	−1.63
2	UGC 5101	09 35 51.60	+61 21 11.59	0.039	Sy1.5	24.459	23.209	8.35	−2.00
3	NGC 7674	23 27 56.70	+08 46 44.25	0.029	Sy2	24.311	23.390	7.73	−1.90
4	IC 2227	08 07 07.19	+36 14 00.46	0.032	Sy2	24.445	23.597	—	—
5	ESO 362−8	05 11 09.09	-34 23 36.74	0.016	Sy2	24.193	23.332	—	—
6	ESO 406-4	22 42 33.37	-37 11 07.57	0.029	Sy2	24.279	23.360	8.02	−2.49
7	2MFGC 13496	16 51 05.68	-01 27 48.23	0.041	Emission Line	23.993	23.641	—	—
8	2MASX J03585442+1026033	03 58 54.44	+10 26 02.79	0.031	Sy2	23.058	23.246	7.75	−1.20
9	M 58	12 37 43.59	+11 49 05.12	0.005	Sy2	–	–	8.10	−3.44
10	3C 371	18 06 50.68	+69 49 28.11	0.049	BL LAC	23.139	22.101	—	—
11	IC 1198	16 08 36.38	+12 19 51.60	0.034	Sy1	23.296	23.048	7.51	−0.41
12	2MASX J09261742-8421330	09 26 17.43	-84 21 33.09	0.064	Sy2	23.331	22.381	7.10	−0.06
13	UGC 12348	23 05 18.83	+00 11 22.15	0.025	Sy2	23.349	22.711	—	—
14	2MASX J02420381+0510061	02 42 03.82	+05 10 06.18	0.073	Sy2	23.445	22.390	—	—
15	ESO 234-50	20 35 57.87	-50 11 32.17	0.009	Sy2	23.495	23.211	6.04	−1.47
16	NGC 2273	06 50 08.67	+60 50 44.86	0.006	Sy2	24.184	23.828	8.22	−2.68
17	FRL 265	06 56 29.79	-65 33 37.73	0.029	Sy1	–	—	—	—
18	MRK 231	12 56 14.23	+56 52 25.24	0.042	Sy1	24.692	24.343	7.94	−1.41
19	PG 1211+143	12 14 17.67	+14 03 13.18	0.081	Sy1	23.249	21.986	8.60	−1.82
20	MRK 376	07 14 15.08	+45 41 55.90	0.056	Sy1.5	23.511	22.480	8.22	−0.46
21	NGC 7378	22 47 47.69	-11 48 59.86	0.009	Sy2	23.184	22.853	5.49	−0.08
22	2MASX J11462959+7421289	11 46 29.54	+74 21 29.04	0.058	Sy2	23.049	21.891	8.22	−1.80
23	SWIFT J2006.5+5619	20 06 33.32	+56 20 36.40	0.044	Sy2	23.083	23.062	7.07	−0.62
24	2MASX J06363227−2034532	06 36 32.25	-20 34 53.18	0.056	Sy2	24.147	23.340	8.44	−1.65
25	2MASX J09034285−7414170	09 03 42.89	-74 14 17.42	0.093	Sy2	23.252	23.074	7.88	−1.88
26	2MASX J00091156−0036551	00 09 11.60	-00 36 54.78	0.073	Sy2	23.369	23.708	8.54	−1.58

[a]https://simbad.cds.unistra.fr/simbad/sim-fbasic

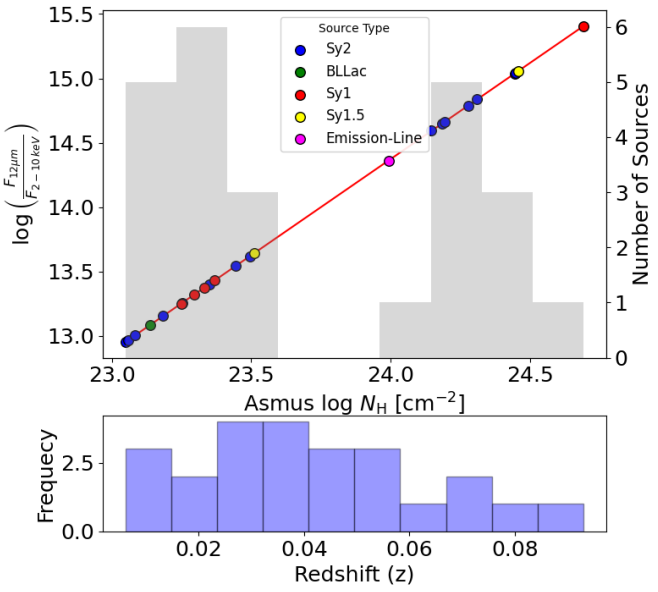

Figure 1. Upper panel: Distribution of the 26 sources with predicted line-of-sight column densities ($N_{\rm H,los}$) based on the empirical relation from Asmus et al. (2015). The histogram in the background shows the number of sources in each $N_{\rm H}$ bin. The scatter points represent the logarithmic ratio of mid-infrared (12 μm) to observed 2–10 keV X-ray flux plotted against the predicted $N_{\rm H}$ (x-axis), with different AGN types indicated by color. The red line shows the linear regression fit, illustrating the correlation between the flux ratio and the Asmus-predicted column density. Lower panel: Distribution of source redshifts.

(2000), and the Verner et al. (1996) photoelectric absorption cross-section.

Heavily obscured AGN have complex spectra, where the contribution of the Compton scattering and of the fluorescent iron line becomes significant with respect to less obscured AGN spectra. Consequently, these sources should be treated in a self-consistent way, that allows one to properly measure the line-of-sight column densities, using models developed specifically for this purpose. To analyze these complex spectra in a more self-consistent way, we use three torus models: `MyTorus` (Murphy & Yaqoob 2009; Yaqoob 2012; Yaqoob et al. 2015), `Borus02` (Baloković et al. 2018), and `UXCLUMPY` (Buchner et al. 2019a). Three best-fitted unfolded spectra with the data-to-model residuals are presented in Fig. 2, in which the *NuSTAR*, XMM-*Newton*, and *Chandra* observations of one of the sources (IC 2227) from our sample are jointly fitted using `MyTorus`, `Borus02`, and `UXCLUMPY`, respectively. The best-fit unfolded spectra, along with the corresponding data-to-model residuals for the remaining 25 sources, are shown in Appendix C, Fig. 14. All source spectra were binned with the `grppha` task to achieve a minimum of 20 counts per bin, ensuring the applicability of χ^2 statistics in the spectral analysis. For sources with only *Swift*-XRT data, we instead adopted a minimum of 5 counts per bin and employed Cash statistics (C-stat) as the fit-statistics for spectral fitting. A brief description of each model used in this analysis is given below.

4.1. *MyTorus*

The `MyTorus` (Murphy & Yaqoob 2009; Yaqoob 2012; Yaqoob et al. 2015) model is divided into three distinct components.

1. A multiplicative component (`MYTZ`) containing photoelectric absorption and Compton scattering attenuation. This component is applied to the main power law continuum. The viewing angle of `MYTZ` is fixed to 90°, so its N_H corresponds to the los value.

2. A scattered continuum, also known as "reprocessed component" (`MYTS`). This component models those photons that are observed after one or more interactions with the material surrounding the SMBH. The normalization of the reprocessed component with respect to the main continuum is hereby denoted as $\rm A_S$.

3. The neutral Fe fluorescent emission lines, more in detail the Fe Kα line at 6.4 keV and the Kβ at 7.06 keV (`MYTL`). We denote the normalization of these lines with respect to the main continuum as $\rm A_L$.

In `MyTorus`, the obscuring material surrounding the SMBH is assumed to have a toroidal, azimuthally symmetric shape. The torus covering factor, c_f, is not a free parameter and is fixed to c_f=cos($\theta_{\rm OA}$)=0.5, where $\theta_{\rm OA}$=60° is the torus half-opening angle. The angle between the torus axis and the observer is free to vary, within the range $\theta_{\rm obs}$=[0–90]°. In our analysis, we use `MyTorus` in the so-called "decoupled mode" (Yaqoob et al. 2015): for the main continuum, we fix $\theta_{\rm obs}$=90°, while for the reprocessed component we test two different scenarios, one with $\theta_{\rm obs,A_S,A_L} = 90°$ (near-side of the torus), the other with $\theta_{\rm obs,A_S,A_L} = 0°$ (far-side of the torus). The relative weights for the MYTS and MYTL components are tied together ($A_S = A_L$) and denoted as A_{90} and A_0 for $\theta_{obs} = 90°$ and 0°, respectively. The `MyTorus` decoupled configuration allows for the separate measurement of $N_{\rm H,los}$, and the average torus column density, $N_{\rm H,avg}$, thus mimicking a clumpy torus distribution. In this configuration, while the column density

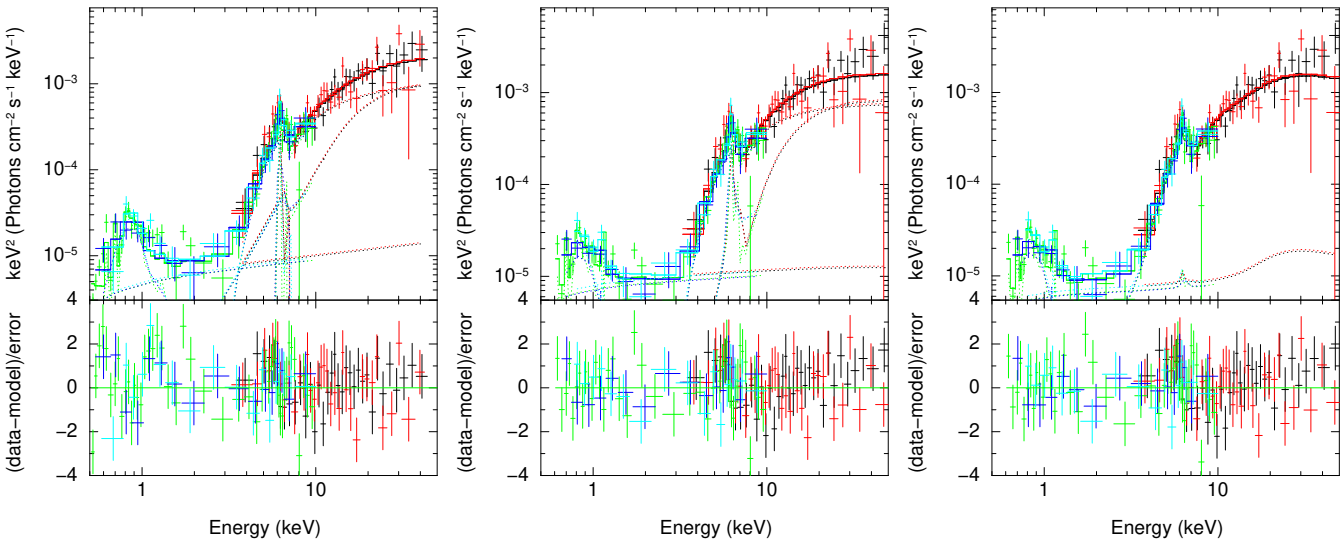

Figure 2. Unfolded spectra and model-to-data ratio for IC 2227 using `MyTorus` (left panel), `Borus02` (middle panel), and `UXCLUMPY` (right panel).

associated with the transmitted component (`MYTZ`) is the line of sight one, the column densities associated with `MYTS` and `MYTL` are tied together to estimate $N_{\rm H,avg}$.

4.2. *Borus02*

`Borus02` (Baloković et al. 2018) is an updated and improved version of the widely used `BNTorus` model (Brightman & Nandra 2011). This radiative transfer code models the reprocessed emission component of an AGN X-ray spectrum, i.e., following the `MyTorus` nomenclature we introduced in the previous section, the "reprocessed component" and the neutral Fe emission lines.

In `Borus02`, the obscuring material has a quasi–toroidal geometry, with conical polar cutouts. Both the average torus column density ($N_{\rm H,avg}$) and the torus covering factor are free parameters in the model: the torus covering factor value can vary in the range c_f=[0.1–1.0], corresponding to a torus opening angle range $\theta_{\rm OA}$=[84–0]°. In principle, the angle between the torus axis and the observer is a free parameter of this model, but in our analysis we fix it to $\theta_{\rm obs}$=60° and 30°, a common assumption for the type 2 (Corral et al. 2011; Zhao et al. 2020) and type 1 (Matt et al. 2006; Decarli et al. 2008; Ricci et al. 2010) sources.

Finally, since the `Borus02` models itself does not take into account line-of-sight absorption, we follow the Baloković et al. (2018) approach and derive $N_{\rm H,los}$ in XSPEC using the components `zphabs` × `cabs`, to properly model Compton scattering losses out of the line of sight. In the overall fitting model, the $N_{\rm H,z}$ value is a free parameter, independent from $N_{\rm H,avg}$, and assumed to be identical in `zphabs` and `cabs`.

4.2.1. *UXCLUMPY*

Unlike `Borus02` and `MyTorus`, `UXCLUMPY` (Buchner et al. 2019a) does not assume a uniform torus. Instead, `UXCLUMPY` is a physically motivated model that reproduces the X-ray data by simulating different cloud sizes and distributions.

The first table accounts for the transmitted and reflection components, including fluorescent lines. `UXCLUMPY` produces the reflection component through the cloud distribution it generates. However, for some sources that are reflection-dominated, a Compton-thick reflector near the corona can be added. This can be thought of as an inner wall that blocks the line of sight to the corona while also reflecting its emission. The second table reproduces the intrinsic continuum that leaks through the clumps of the torus.

`UXCLUMPY` differs from `Borus02` in that it does not include a parameter to measure the average torus column density. However, it measures other torus parameters such as the inclination angle (with a slightly larger range than `Borus02` $\cos[\theta_{obs}] = 0 - 1.00$), the dispersion of the cloud distribution `TORsigma` (ranges from 6° to 90°), and the covering factor of the inner reflector `CTKcover` (ranges from 0 to 0.6).

4.3. *Additional components to the best-fit model*

Besides using `MyTorus`, `Borus02`, and `UXCLUMPY` in the configurations described in the previous sections, we included the following components in our best-fit model:

1. A second power law, with photon index Γ_2=Γ_1, where Γ_1 is the photon index of the primary power law. This second power law is introduced to take

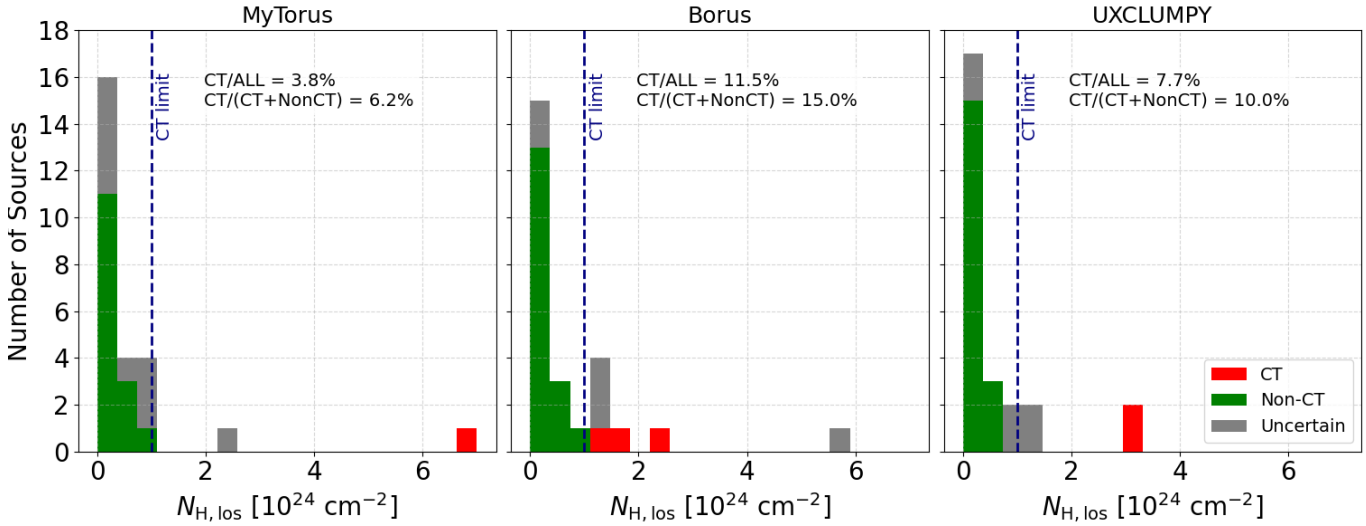

Figure 3. Fraction of CT-AGN (red bars) derived using `MyTorus` (left panel), `Borus02` (middle panel), and `UXCLUMPY` (right panel). In each panel, confirmed non-CT AGN are shown in green, while sources with uncertain values of $N_{\rm H,los}$ are indicated by gray bars. The blue dashed vertical line shows the CT limit.

into account the fraction (f_s) of accreting SMBH emission which is scattered, rather than absorbed, by the gas surrounding the SMBH. We assume this component to be unabsorbed.

2. A constant, $c_{instrument}$, allowing for a re-normalization of the *NuSTAR* FPMA spectrum with respect to the FPMB and the 0.5-10 keV soft X-ray data from XMM-*Newton*, *Chandra* or *Swift*-XRT. Such a component models both cross-calibration offsets between the instruments and potential flux variability between the different observations.

3. A `mekal` component, to account for the emission below 3 keV caused by diffuse hot gas.

The three torus models are implemented in `XSPEC` as follows:

$$Model\ A = constant \times phabs \times [MYTZ_{90} \times zpowerlw + A_{90} \times (MYTS_{90} + MYTL_{90}) + A_0 \times (MYTS_0 + MYTL_0) + f_s \times zpowerlw + mekal]. \quad (1)$$

$$Model\ B = constant \times phabs \times (borus02 + zphabs \times cabs \times zpowerlw + f_s \times zpowerlaw + mekal). \quad (2)$$

$$Model\ C = constant \times phabs \times (uxcl\_cutoff.fits + f_s \times uxcl\_cutoff\_omni.fits + mekal). \quad (3)$$

5. SPECTRAL FITTING RESULTS

The best-fit results including the photon index (Γ) $N_{\rm H,los}$, $N_{\rm H,avg}$, c_f, `TORsigma`, `CTKcover`, model normalizations, the 2-10 keV flux, and the 2-10 keV absorption corrected intrinsic luminosities as obtained from the spectral analysis using the three torus models of the 26 sources are given in Table 3. The description of the fitting process for the sources and a case study on comparing the measured column densities in this work with the previously obtained analysis are reported in the Appendix A.

Our analysis shows that a small fraction of sources are true CT-AGN. To classify CT-AGN across the three torus models – `MyTorus`, `Borus02`, and `UXCLUMPY` – we used the line-of-sight column densities, along with their associated asymmetric errors. A source was classified as CT if both the upper and lower bounds of the error interval placed at $N_{\rm H,los} > 10^{24}$ cm^{-2} . Conversely, a source was classified as Non-CT if both bounds were below the threshold. If the classification could not be determined unambiguously due to the error bars crossing the threshold or due to the presence of censoring indicators it was marked as Uncertain. In Fig. 3, we show the fraction of CT-AGN (red bars) obtained from the `MyTorus` (left), `Borus02` (middle), and `UXCLUMPY` (right) models. For comparison, the same panels also display confirmed non-CT AGN in green, while sources with uncertain $N_{\rm H,los}$ values are represented by gray bars.

We found 10 (38.5%), 6 (23.1%), and 6 (23.1%) sources classified as Uncertain by `MyTorus`, `Borus02`, and `UXCLUMPY`, respectively. Among the classified sources, `MyTorus` identified a single CT-AGN candi-

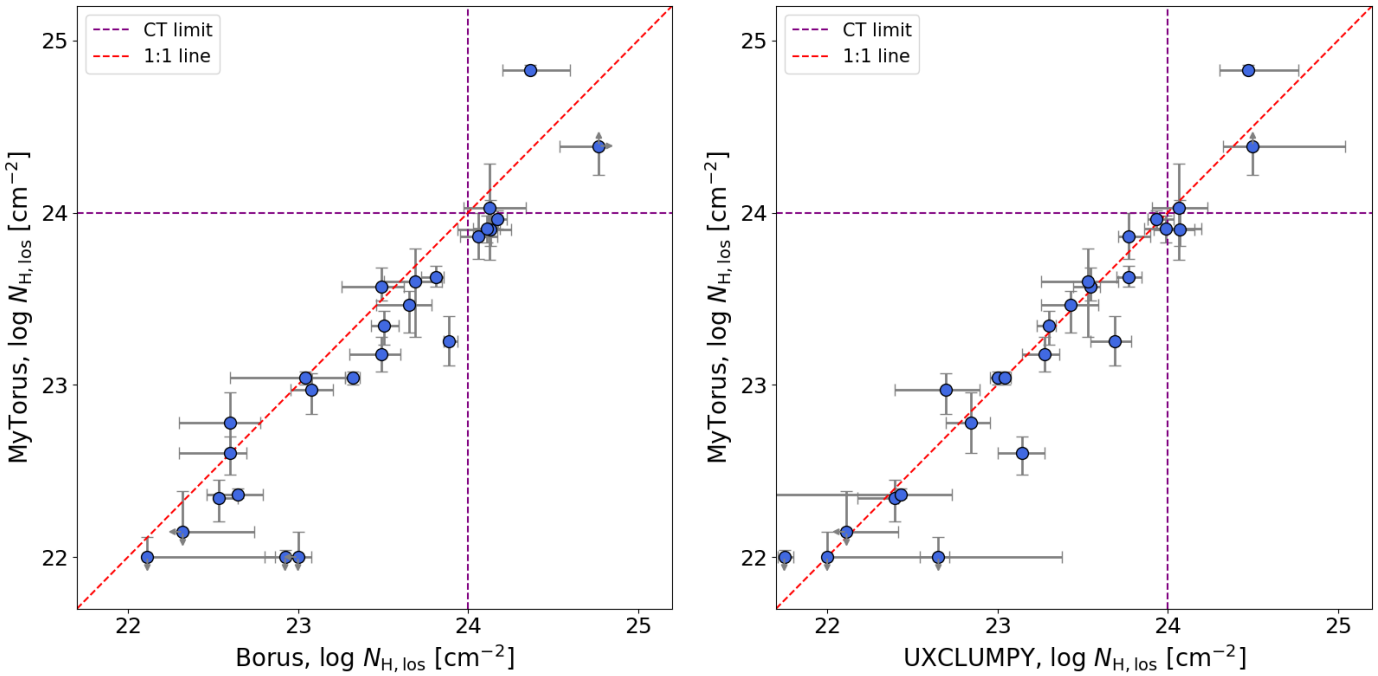

Figure 4. Comparison between the line-of-sight column densities obtained from `MyTorus`, `Borus02`, and `UXCLUMPY`. The red dashed line marks the 1:1 relation between the estimated $N_{\rm H,los}$ from different torus models, while the purple dashed lines indicate the Compton-thick boundary.

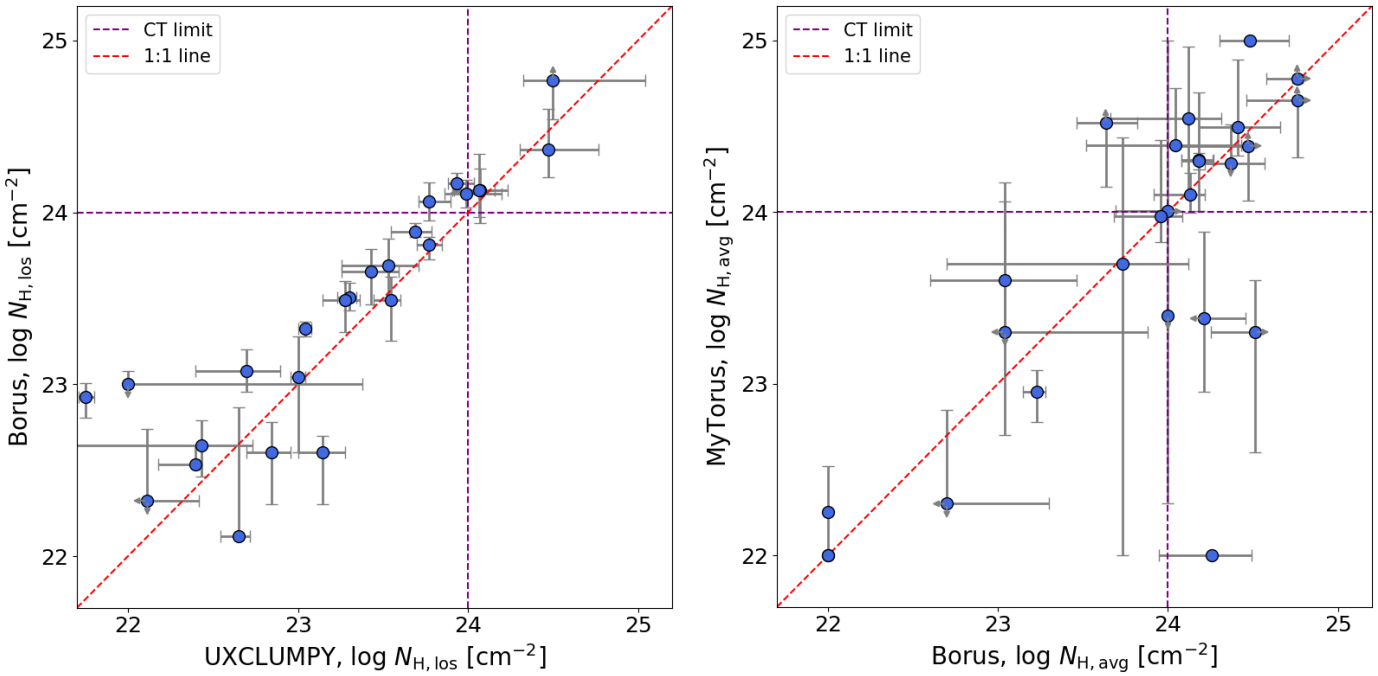

Figure 5. Comparison between the line-of-sight column densities obtained from `Borus02`, and `UXCLUMPY` (left panel). The right panel shows the comparison between average column densities inferred using `MyTorus`, and `Borus02`. The red dashed line denotes the 1:1 relation between the $N_{\rm H,los}$ values estimated from different torus models, and the purple dashed lines mark the Compton-thick threshold.

date (ESO 362−8; 3.8%), Borus02 identified three (ESO 362−8, 2MASX J02420381+0510061, and 2MASX J06363227−2034532; 11.5%), and UXCLUMPY identified two (MRK 1073 and ESO 362−8; 7.7%). The agreement across all three models highlights ESO 362−8 as a robust CT-AGN candidate, consistent with earlier findings (Silver et al. 2022). In addition to the CT classification, we examined the distribution of sources below the CT threshold (excluding the uncertain cases). We found that 10 (38.5%), 10 (38.5%), and 11 (42.3%) sources in MyTorus, Borus02, and UXCLUMPY, respectively, have $10^{23} \leq N_{\rm H,los} < 10^{24}$ cm^{-2}, while 5 (19.2%), 7 (26.9%), and 7 (26.9%) sources fall below 10^{23} cm^{-2}.

6. DISCUSSION

6.1. *Comparison among MyTorus, Borus02, and UXCLUMPY*

The comparison of $N_{\rm H,los}$ obtained for a sample of 26 AGN using three physically motivated X-ray torus models — MyTorus, Borus02, and UXCLUMPY — provides important insights into how different assumptions about torus geometry affect spectral fitting outcomes. Each of these models assumes distinct torus structures: MyTorus adopts a doughnut-shaped, azimuthally symmetric torus with a fixed opening angle and a uniform density distribution; Borus02 allows for a more flexible, quasi-spherical geometry with variable opening angles and covering factors; and UXCLUMPY models the torus as a clumpy, patchy distribution of obscuring material, thought to better represent a physically realistic torus structure in many AGN unification scenarios. Despite these significant differences in geometry and parameterization, Fig. 4, and 5 (left panel) show that the majority of the best-fit $N_{\rm H,los}$ values are in reasonably good agreement across the three models, with all of them capturing similar trends in obscuration level among sources. The spearman rank correlation performed between $N_{\rm H,los}$ values yields the coefficients (ρ) = 0.95, 0.97 and 0.93, respectively, for MyTorus vs. Borus02, MyTorus vs. UXCLUMPY, and Borus02 vs. UXCLUMPY. This suggests that the line-of-sight column density, being a robust quantity, is relatively well constrained by the data regardless of torus geometry assumptions.

However, some discrepancies still emerge. For example, Fig. 3 reveals that Borus02 tends to identify a larger fraction of sources as CT-AGN, defined as having $N_{\rm H,l.o.s} > 10^{24}$ cm^{-2}, compared to MyTorus and UXCLUMPY. The scatter plots (Fig. 4 and left panel of Fig. 5) and the ρ-values suggest that: while a strong correlation exists between the $N_{\rm H,los}$ obtained from MyTorus and the other two models (as shown by points clustering around the 1:1 red dashed line), several sources lie above or below the line by substantial margins, especially at lower column densities. This deviation is particularly apparent at the Compton-thin to Compton-thick transition, suggesting that model geometry and assumptions may significantly influence classification at these thresholds. The vertical and horizontal magenta lines in Fig. 4 and 5 mark the CT threshold, showing that while most sources lie below this boundary in all models, a few are pushed into the CT-AGN regime by Borus02 or UXCLUMPY.

In summary, while all three models provide broadly consistent estimates for $N_{\rm H,los}$ over a wide range of column densities, Borus02 appears more inclined to identify sources as Compton-thick. This suggests that, while geometry may not drastically alter the overall trend of $N_{\rm H,los}$, it can critically influence classification at threshold values. Our result that estimates $N_{\rm H,los}$ remain consistent across MyTorus, Borus02, and UXCLUMPY is echoed in previous studies (e.g., Marchesi et al. 2018; LaMassa et al. 2019; Torres-Albà et al. 2023; Pizzetti et al. 2025), who also found strong agreement between MyTorus, and Borus02 in similar parameter regimes.

MyTorus, and Borus02 are widely used X-ray spectral models developed to characterize the obscuring torus in AGN. In both models, the average torus column density represents the global, line-of-sight-independent measurement of the torus matter distribution, derived primarily from modeling the reprocessed (reflected) emission components. To assess the consistency between the two models, we calculated $N_{\rm H,avg}$ values for a sample of 26 AGN using MyTorus, and Borus02. Within the uncertainties, the results show overall agreement, supported by a Spearman rank correlation coefficient of $\rho = 0.63$ with a highly significant p-value of 5.3×10^{-4}, as shown in the right panel of Fig. 5.

6.2. *Clumpy Torus Scenario*

We explored the difference between $N_{\rm H,avg}$ and $N_{\rm H,los}$ as obtained from the MyTorus and Borus02 models:

$$\Delta N_H = N_{\rm H,avg} - N_{\rm H,los} \tag{4}$$

Asymmetric uncertainties in both quantities were propagated in logarithmic space to estimate the upper and lower bounds on ΔN_H. A source was classified as having $N_{\rm H,avg} < N_{\rm H,los}$ if the lower limit of $N_{\rm H,los}$ (accounting for its upper error) exceeded the upper limit of $N_{\rm H,avg}$ (accounting for its upper error), and as $N_{\rm H,avg} > N_{\rm H,los}$ if the upper limit of $N_{\rm H,los}$ (from its lower error) was smaller than the lower limit of $N_{\rm H,avg}$. Sources for which the error ranges overlapped or included unknown (censored) bounds were conservatively assigned to an "uncertain" category.

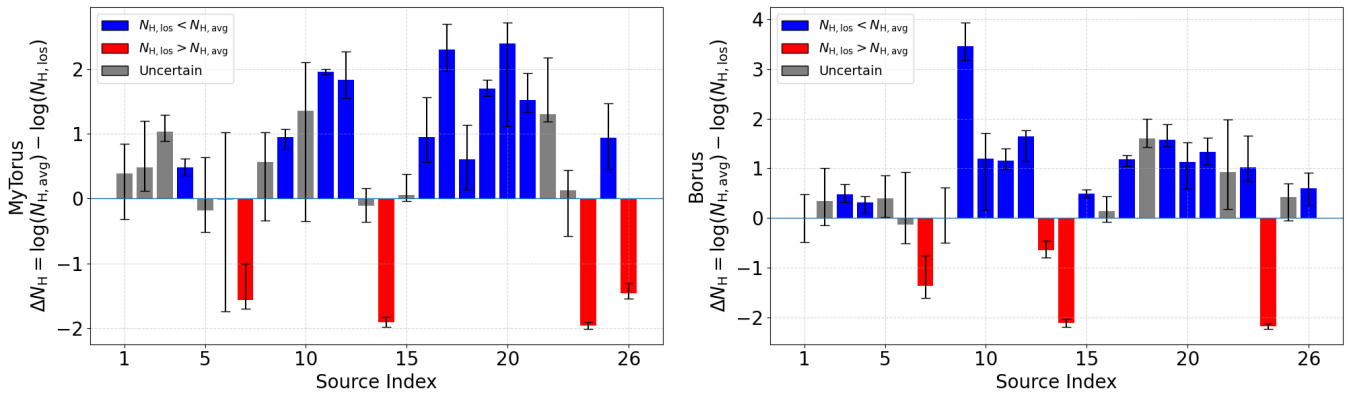

Figure 6. Bar plot showing the difference $\Delta N_H = N_{\rm H,avg} - N_{\rm H,los}$ for each source obtained using `MyTorus` (left panel) and `Borus02` (right panel), with vertical error bars representing the propagated asymmetric uncertainties in logarithmic space. Bars are color-coded by classification: red indicates sources with $N_{\rm H,los} > N_{\rm H,avg}$, blue denotes $N_{\rm H,los} < N_{\rm H,avg}$, and gray corresponds to sources with uncertain classification due to overlapping error ranges or censored (unknown) error values. The horizontal dashed line marks ΔN_H=0, where the line-of-sight and average torus column densities are equal.

Across the sample, the classification based on $\Delta N_{\rm H} = \log N_{\rm H,avg} - \log N_{\rm H,los}$ was generally consistent between the `MyTorus` and `Borus02` models, with no contradictions identified among the sources that could be reliably classified in both cases (see Fig. 6). Specifically, for `MyTorus`, we found that $N_{\rm H,los} > N_{\rm H,avg}$ in 4 out of 26 sources (15.4%), and $N_{\rm H,los} < N_{\rm H,avg}$ in 11 sources (42.3%), while the rest of 11 sources (42.3%) remained unclassified due to overlapping uncertainties or censored error bounds. Similarly, for `Borus02`, 4 sources (15.4%) showed $N_{\rm H,los} > N_{\rm H,avg}$, and 13 sources (50.0%) had $N_{\rm H,los} < N_{\rm H,avg}$, with 9 sources (34.6%) unclassified. We do not attempt to compare classifications for the unclassified cases, where uncertainties preclude meaningful interpretation. We note that in a few instances the $N_{\rm H,avg}$ values were pegged at very low limits; these cases mostly fall into the $N_{\rm H,los} > N_{\rm H,avg}$ category, and although pegged, they were still counted as classified rather than uncertain, since the inequality with respect to $N_{\rm H,los}$ is unambiguous. Only in a source `MyTorus` and `Borus02` produced opposite interpretation: 2MASX J00091156−0036551 (index-26), where `MyTorus` yielded $N_{\rm H,avg} < N_{\rm H,los}$, `Borus02` indicated the opposite, with $N_{\rm H,avg} > N_{\rm H,los}$. The discrepancy is driven by `MyTorus` pegging $N_{\rm H,avg}$ at a low value, while `Borus02` is able to constrain it.

The predominance of $N_{\rm H,los} < N_{\rm H,avg}$ may indicate that, for many AGN, our line of sight intercepts a less dense region of the torus, possibly near the edge of the torus opening, while the global structure remains more heavily obscured on average. This is naturally expected in a clumpy torus, where variations in orientation, covering factor, and anisotropic cloud distributions can lead to significant discrepancies between the global and line-of-sight column densities (Nenkova et al. 2008; Yaqoob 2012; Baloković et al. 2018). At the same time, an alternative explanation has been put forward by Torres-Albà et al. (2023), who argue that cases with $N_{\rm H,los} < N_{\rm H,avg}$ may instead reflect a dense, geometrically thin (possibly warped) disk-like structure that contributes strongly to reflection, even if the line of sight intersects less obscured gas. Together, these interpretations suggest that both clumpy and flattened dense reflector geometries can account for the observed trend, potentially coexisting in different sources.

The few cases where $N_{\rm H,los} > N_{\rm H,avg}$ could correspond to transient intersections with dense clumps, consistent with observed variability in some AGN. A representative example is NGC 1358, which was initially identified as a candidate $N_{\rm H,los}$–variable AGN due to its elevated $N_{\rm H,los}$ relative to $N_{\rm H,avg}$ and low covering factor. Subsequent monitoring with XMM-*Newton* and *NuSTAR* confirmed it as a changing-look AGN (Marchesi et al. 2022). This scenario is also supported by Torres-Albà et al. (2021), who suggest that when $N_{\rm H,los} > N_{\rm H,avg}$, the torus is likely clumpy rather than uniform. In this case, our line of sight happens to cross a particularly dense cloud, while the overall torus is less dense on average. This creates a "thin-reflector" situation, where the reflected X-ray emission mainly comes from the difference between dense clumps and the more diffuse gas around them.

As shown in Fig. 5 (right panel), the torus column densities for the majority of Compton-thin sources, as well as for the few CT-AGN in our sample extend into the 10^{24} cm^{-2} regime, indicating that Compton-thick reflectors are a common feature across both categories. A comparable trend has also been noted in previous works (e.g., Buchner et al. 2019b; Zhao et al. 2021). This behavior, also highlighted by Torres-Albà et al. (2023),

suggests that while line-of-sight obscuration can fluctuate due to clumpy clouds, the global torus structure remains consistently Compton-thick, providing a stable reflective component.

As mentioned earlier, only one source (excluding the uncertain measurements) displayed conflicting behavior between models, suggesting that, despite differences in model assumptions, the overall trend of $N_{\rm H,avg} > N_{\rm H,los}$ observed in our sample is robust. This result supports the scenario reported in Zhao et al. (2021), where the authors found that $N_{\rm H,avg}$ is mostly constant across a wide range of $N_{\rm H,los}$, and is on average $\log N_{\rm H,avg} \sim 24.1$. Since most of the objects in this work have $\log N_{\rm H,los} < 24$, it makes sense that in most of them $N_{\rm H,los}$ is smaller than $N_{\rm H,avg}$.

6.3. *Testing the accuracy of different* $\rm N_{H,los}$ *predictors*

Asmus et al. (2015) leveraged the tight correlation between MIR and X-ray emission in AGN to estimate the line-of-sight column density. They compiled high-resolution 12μm MIR fluxes and 2-10 keV X-ray fluxes for 152 local AGN, finding a near-linear correlation across obscuration classes. Crucially, obscured AGN (Seyfert 2 and Compton-thick) deviate below this trend, i.e., their X-ray flux is relatively suppressed compared to MIR, because absorption reduces X-ray output. From this, Asmus et al. (2015) derived an empirical relation:

$$\log N_{\rm H} = (14.37 \pm 0.11) + (0.67 \pm 0.11) \log \left(\frac{F_{12\,\mu\rm m}}{F_{2-10\,\rm keV}} \right) \quad (5)$$

allowing $N_{\rm H,los}$ estimates directly from the IR–X-ray flux ratio ($\frac{F_{12\mu m}}{F_{2-10keV}}$). This method works best for heavily obscured AGN ($\log \rm N_H \gtrsim 23$), but its accuracy declines for less obscured sources.

Silver et al. (2023) introduced a supervised machine-learning (ML) approach using a multiple linear regression model trained on a set of 451 *Swift*-BAT AGN with known $N_{\rm H}$ values. Their feature set included: six WISE MIR color indices (e.g., W1-W2, W2-W3), the MIR/soft X-ray flux ratio, two soft X-ray hardness ratios from *Swift*-XRT, and count rates in multiple *Swift*-BAT energy bands. They demonstrated strong predictive performance, achieving a Spearman correlation of 0.86 and correctly classifying ∼75% of obscuration levels-even below $\log \rm N_H \lesssim 22.5$. This method highlighted that the two soft X-ray hardness ratios and the IR–X-ray flux ratio were the most significant predictors. Their method thus refines the Asmus et al. (2015) relation by combining IR–X-ray information with X-ray spectral diagnostics and broad-band count rates in a statistically robust, machine-learning framework.

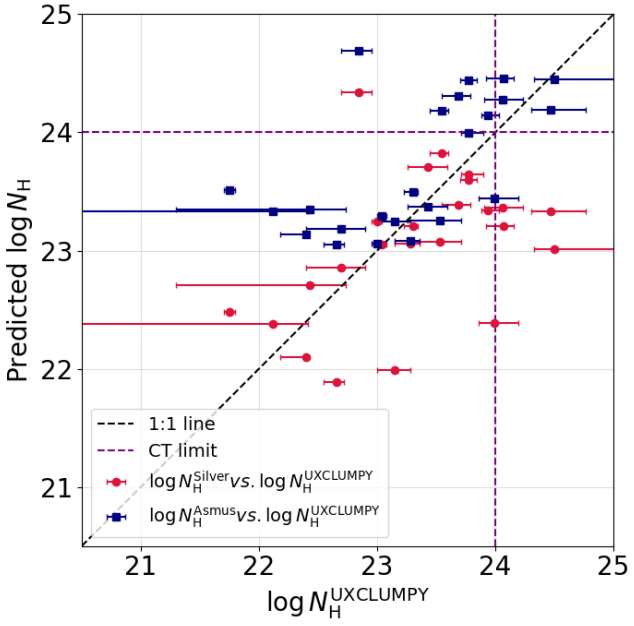

Figure 7. Predicted $N_{\rm H,los}$ from Asmus et al. (2015) (blue), and from the machine learning method (red) by Silver et al. (2023), as a function of the $N_{\rm H,los}$ obtained from the `UXCLUMPY` fits. The black dashed line marks the 1:1 relation between the predicted and `UXCLUMPY`–derived $N_{\rm H,los}$, while the purple dashed lines indicate the Compton-thick boundary.

We compared $N_{\rm H,los}$ values derived from our X-ray spectral fitting using three independent torus models (`MyTorus`, `Borus02` and `UXCLUMPY`) with predictions from two literature methods: (1) the IR–X-ray correlation from Asmus et al. (2015), and (2) the machine learning (ML) model from Silver et al. (2023). The predicted $N_{\rm H,los}$ values are given in Table 1. The consistency of $N_{\rm H,los}$ values across the three torus models (see Fig. 4, 5) suggest the robustness of the best-fit estimates. Therefore, we compare $N_{\rm H,los}$ obtained from `UXCLUMPY` model fits with the predicted values, and report this comparison in Fig. 7. We exclude two sources from the analysis: M 58 (source index - 9) was omitted since its `UXCLUMPY` column density was around $10^{20}\,\rm cm^{-2}$, below the lower threshold of $10^{21}\,\rm cm^{-2}$ used in the analysis of Silver et al. (2023). FRL 265 (source index - 17) was also excluded from the ML prediction because it lacked a W3 measurement, preventing an estimate of $N_{\rm H,los}$. We statistically tested the agreement between the `UXCLUMPY` line-of-sight column densities and the predictions from the ML and Asmus methods. Two complementary approaches were adopted:

1. Chi-square test: Here we tested the null hypothesis that the predicted values lie on the one-to-one relation with the `UXCLUMPY` measurements (y=x). Both compar-

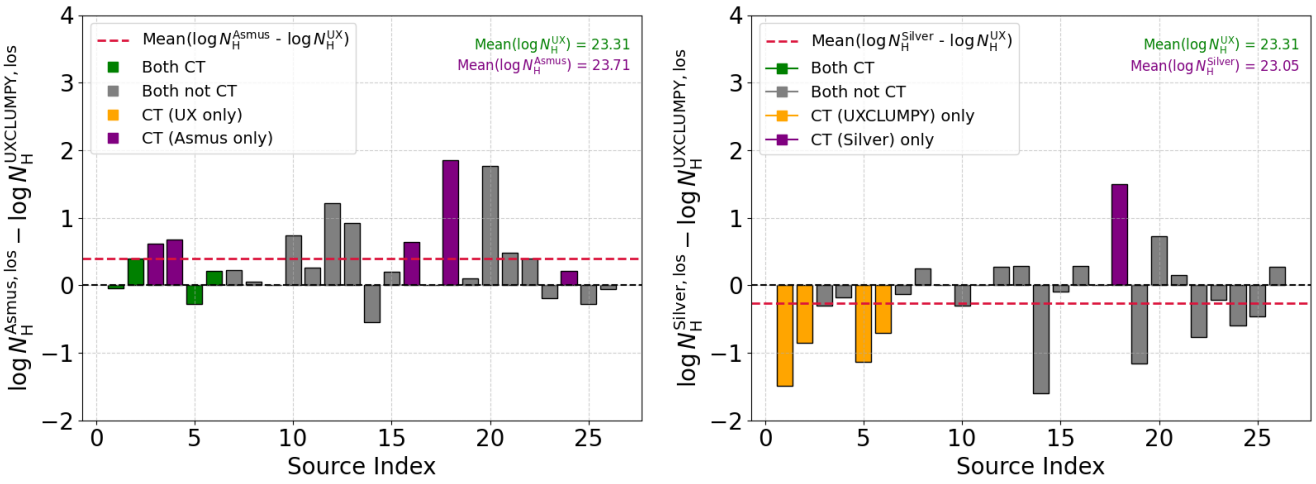

Figure 8. Comparison of the predicted $N_{\rm H,los}$ from Asmus et al. (2015) (left panel) and from the machine learning method by Silver et al. (2023) (right panel), with $N_{\rm H,los}$ obtained from `UXCLUMPY` fits. Colored bars indicate differences in source classification: green marks cases where both prediction and `UXCLUMPY` classify the source as CT-AGN, purple shows cases classified as CT only by the prediction, yellow as CT only by `UXCLUMPY`, and gray where both classify the source as non-CT. Source indices follow Table 1. The red dashed line indicates the offset between the mean predicted and mean derived $N_{\rm H,los}$.

isons yield very large chi-square values relative to the degrees of freedom (ML vs `UXCLUMPY` $\chi^2 = 1044$ for 24 dof; Asmus vs `UXCLUMPY` $\chi^2 = 3807$ for 24 dof), corresponding to vanishingly small p-values. This indicates that neither method is formally consistent with the one-to-one line.

2. Paired t-test: We also compared the mean offset between predicted and measured logN$_{\rm H}$. For the ML method, the mean difference is -0.26 dex with a p-value of 0.087, indicating no statistically significant systematic offset. In contrast, Asmus predictions show a larger positive offset (+0.40 dex) with a highly significant p-value (p = 0.003), suggesting a systematic overprediction relative to `UXCLUMPY`.

Taken together, while both prediction methods deviate from the derived `UXCLUMPY` values in a strict χ^2 sense, the mean comparison indicates that the ML predictions by Silver et al. (2023) (mean log $N_{\rm H,los} = 23.05$) lie closer to the `UXCLUMPY` mean (23.31) than the Asmus estimates (23.71). This is consistent with the t-test results, which suggest that the ML approach is statistically more compatible with the `UXCLUMPY` fits, whereas the Asmus predictions exhibit a more pronounced systematic offset.

The left panel of Fig. 8 shows differences between the IR–X-ray $N_{\rm H}$ predictions (Asmus et al. 2015) and the `UXCLUMPY`- based fits. A large number of sources, especially those tagged as Compton-thin by `UXCLUMPY` but Compton-thick by Asmus et al. (2015) (purple bars), indicate that the IR–X-ray method tends to overpredict $N_{\rm H}$, particularly for sources with lower intrinsic obscuration (logN$_{\rm H} \lesssim 23$ cm^{-2}) (see Fig. 7). This is consistent with the idea that MIR emission can remain strong even when the X-ray emission is weak due to moderate absorption, misleading the empirical correlation. Thus, false positives (CT, or high obscuration classification only by Asmus et al. 2015) are evident, making the method less reliable at lower $N_{\rm H,los}$.

The right panel of Fig. 8 shows differences between the ML-based predictions and the `UXCLUMPY` fits. The results demonstrate better alignment in the lower $N_{\rm H,los}$ regime (logN$_{\rm H} \lesssim 23.5$ cm^{-2}, see Fig. 7), with most sources clustering near zero. Only one source exhibits false CT classifications based solely on ML (purple bars in Fig. 8), and the ML predictions show less systematic bias than the Asmus method. However, a trend of underprediction is visible at high obscuration (logN$_{\rm H} \gtrsim 23.5$ cm^{-2}), possibly due to the limited dynamic range or fewer training samples in the Compton-thick regime. As data volume and quality increase (e.g., through future missions like `Athena`, `AXIS`, and deeper IR–X-ray coverage), ML methods will become even more effective. With better representation of CT-AGN in the training set, future models can be optimized to reduce current limitations in the high-$N_{\rm H}$ regime.

6.4. *comparison among* Γ *from* `MyTorus`, `Borus02`, *and* `UXCLUMPY`

The three panels in Fig. 9 compare the best-fit photon indices for the same AGN sample: `MyTorus` vs. `Borus02` (left), `MyTorus` vs. `UXCLUMPY` (middle), and `Borus02` vs. `UXCLUMPY` (right). The dashed blue line indicates the 1:1 relation. In both comparisons, the points scatter around the line, showing a decent overall agreement– typical Γ values cluster between approximately 1.6 and

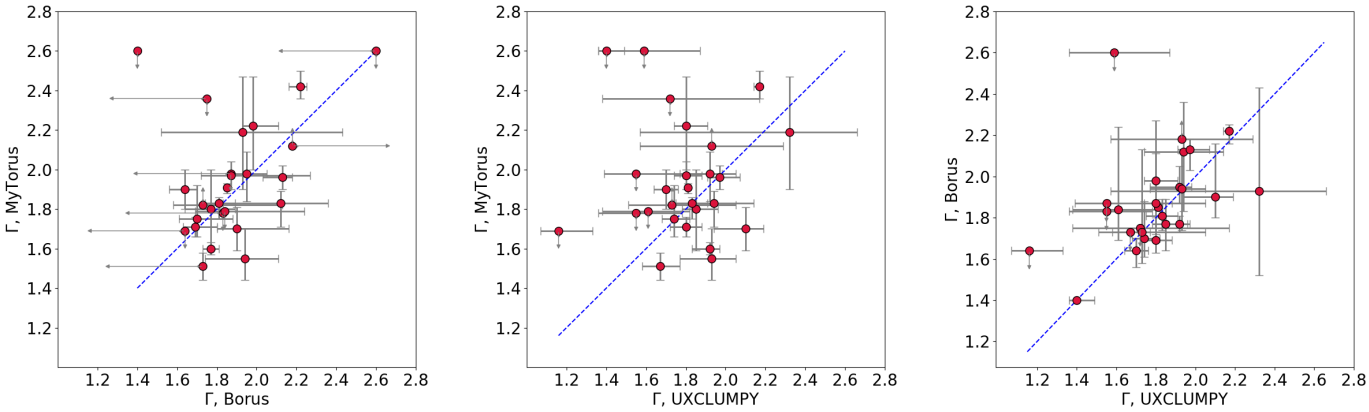

Figure 9. Comparison between best-fit photon index obtained from `MyTorus`, `Borus02`, and `UXCLUMPY`. The blue dashed line marks the 1:1 relation between the data points.

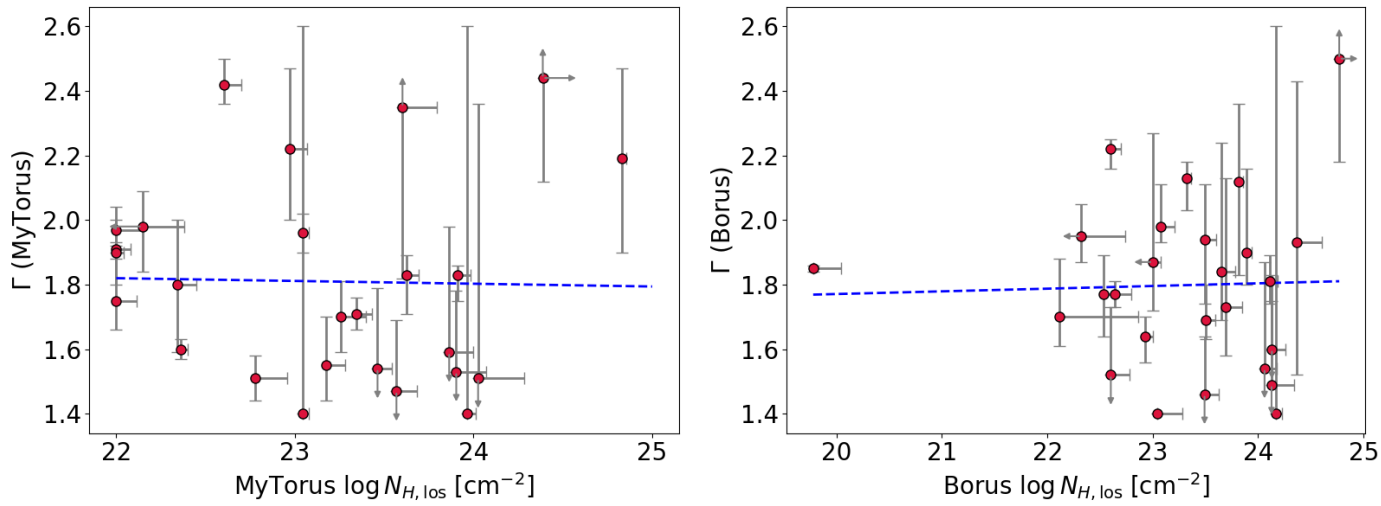

Figure 10. Correlation between the photon indices and the line-of-sight column densities obtained from `MyTorus` (left panel), and `Borus02` (right panel). The blue dashed line indicates the least-squares linear fit to the data.

2.2. However, the `MyTorus`–derived indices systematically exceed those from `UXCLUMPY`. We assessed the consistency of the Γ measurements with a chi–square test. For `MyTorus` vs. `Borus02` we obtain $\chi^2 = 39.66$ for $\nu = 26$ degrees of freedom ($\chi^2_\nu = 1.53$, $p = 0.042$), indicating modest but statistically significant tension at the ∼5% level. `MyTorus` vs. `UXCLUMPY` yields $\chi^2 = 60.84$ ($\nu = 26$; $\chi^2_\nu = 2.34$, $p = 1.29 \times 10^{-4}$), demonstrating an incompatibility. In contrast, `Borus02` vs. `UXCLUMPY` gives $\chi^2 = 21.626$ ($\nu = 26$; $\chi^2_\nu = 0.832$, $p = 0.709$), consistent with the null hypothesis of equal Γ. Overall, `Borus02` and `UXCLUMPY` agree best; `MyTorus` shows moderate tension with `Borus02` and the strongest disagreement with `UXCLUMPY`, likely indicating that model–specific assumptions and torus geometries can introduce systematic differences in Γ estimates.

In the literature, such cross-model comparisons have been reported. For example, Marchesi et al. (2018) compared `MyTorus` and `Borus02` across a sample of CT-AGN observed with *NuSTAR* and found generally good agreement in continuum parameters like Γ–though with increasing scatter at high obscuration. Other works exploring clumpy and smooth torus models (Tanimoto et al. 2019; Saha et al. 2022) caution that Γ may be biased if key geometrical parameters are poorly constrained or degenerate.

In addition to comparing photon indices values across torus models (Fig. 10), we also examined the relationship between Γ and the line-of-sight column density for each model. Our analysis shows no statistically significant correlation between these parameters, with Spearman's correlation coefficients, $r = -0.18$ (`MyTorus`), $r =$

-0.07 (`Borus02`), $r = -0.004$ (`UXCLUMPY`), and corresponding p-values well above 0.05, suggesting that Γ and $N_{\rm H,los}$ are effectively non-degenerate in all three models. These findings reinforce the idea that broadband X-ray coverage– such as that provided by *NuSTAR*– enables robust, independent constraints on both spectral slope and absorption. This is consistent with the conclusions of Marchesi et al. (2018), who demonstrated that the inclusion of high–energy data can decouple Γ and $N_{\rm H,los}$, especially in Compton-thick AGN. Similar results have also been reported by Baloković et al. (2018); Tanimoto et al. (2019), where modeling with geometrically flexible or clumpy torus structures reduced the degeneracy between continuum and absorption parameters. Overall, the absence of a significant Γ–$N_{\rm H,los}$ correlation in our sample supports the reliability of spectral fits across different torus models, provided that broadband X-ray spectral coverage with adequate count statistics is available.

6.5. *Correlations Between Torus Covering Fraction and Other AGN Properties*

We investigated the possible correlations between the torus covering fraction and several AGN parameters, including the $N_{\rm H,los}$, $N_{\rm H,avg}$, their difference, the intrinsic 2–10 keV X-ray luminosity ($\rm L_{2-10keV}$), and the Eddington ratio ($\lambda_{\rm Edd}$). Across all cases, we find no statistically significant correlations, primarily due to the limited sample size and the presence of large uncertainties and censored values in c_f.

As shown in Fig. 11, no clear trend is observed between c_f and $N_{\rm H,los}$ or $N_{\rm H,avg}$. The data show large scatter, and covering fractions span a wide range at both low and high column densities. For c_f versus $N_{\rm H,los}$, the Spearman's rank correlation coefficient is $\rho = -0.56$ with $p = 0.03$, and for c_f versus $N_{\rm H,avg}$, $\rho = 0.24$ with $p = 0.24$, indicating no statistically significant correlation. For $\Delta \rm N_H = \log N_{H,avg} - \log N_{H,los}$, shown in Fig. 12, sources with $\Delta \rm N_H < 0$ (i.e., $N_{\rm H,los} > N_{\rm H,avg}$) all have very low c_f values pegged at the lower bound in the model, rendering these values unreliable and the apparent trend physically uninformative. For this, the Spearman's rank correlation coefficient is $\rho = 0.40$ with $p = 0.04$, dominated by sources with unconstrained c_f.

Figure 13 (left panel) examines the relationship between c_f and the absorption-corrected 2–10 keV luminosity derived from the `Borus02` model. The Spearman's rank correlation does not confirm any statistically significant correlation between these two parameters ($\rho = 0.04$, $p = 0.85$). The best-fit regression:

$$c_f = a * log\rm L_{2-10keV} + b$$

yields $a = -0.01$ and $b = 1.19$.

We also examined the correlation between c_f and the Eddington ratio. The bolometric correction factors, $K_X = \rm L_{bol}/L_{2-10\,keV}$, were derived following the prescription of Duras et al. (2020). In their work, K_X is parametrized as a function of the bolometric luminosity with separate relations for type 1 and type 2 AGN, calibrated using a large multi-wavelength sample. We adopted their best-fit analytic forms (eqs. 4 and 5 in Duras et al. 2020) to compute K_X for each source, using the intrinsic 2–10 keV luminosities obtained from our spectral fits. For each source, the bolometric luminosity was then determined as $\rm L_{bol} = K_X \times L_{2-10\,keV}$. The procedure thus accounts for the luminosity dependence of the bolometric correction, and provides separate estimates for type 1 and type 2 populations. The derived parameters, such as, the bolometric luminosities, bolometric correction factors, and Eddington luminosities for the type 1 and type 2 AGN samples are given in Table 4 and 5 in Appendix B.

The Eddington luminosity is calculated as:

$$\rm L_{Edd} = 1.3 \times 10^{38} \left(\frac{M_{BH}}{M_\odot}\right) erg\,s^{-1},$$

from which the Eddington ratio is defined:

$$\lambda_{\rm Edd} = \frac{\rm L_{bol}}{\rm L_{Edd}}.$$

Figure 13 (right panel) shows the c_f–$\lambda_{\rm Edd}$ relation for 19 sources with available black hole mass estimates. The best-fit linear regression line has a slope of 0.11 and an intercept = 0.91. The Spearman's rank correlation yields $\rho = 0.20$ and $p = 0.41$.

In conclusion, none of the investigated parameters exhibit a robust or statistically significant correlation with the torus covering fraction in our sample. The results are limited by small sample size, large scatter, and poorly constrained or censored c_f values. A larger sample with better c_f constraints is required to test any potential correlations.

7. CONCLUSION AND SUMMARY

In this study, we performed a detailed broadband X-ray spectral analysis of 26 local ($z < 0.1$) obscured AGN selected from the Swift-BAT 150-month catalog. The sources were selected based on mid-infrared to X-ray flux diagnostics and observed with NuSTAR and complementary soft X-ray telescopes (XMM-*Newton*, *Chandra*, *Swift*-XRT). We employed three physically motivated torus models — `MyTorus`, `Borus02`, and `UXCLUMPY` — to constrain key obscuration parameters including the line-of-sight column density, the average torus column density, and the torus covering factor.

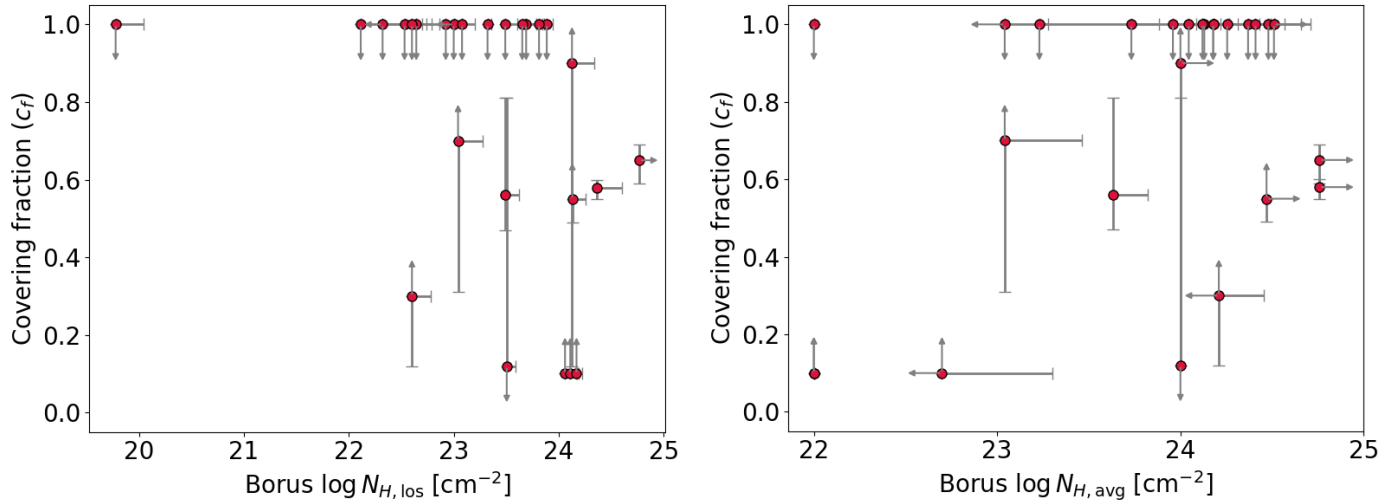

Figure 11. Left panel: Correlation between covering factor (c_f) and the line-of-sight column densities obtained from `Borus02`. Right panel: Correlation between covering factor (c_f) and the average column densities obtained from `Borus02`.

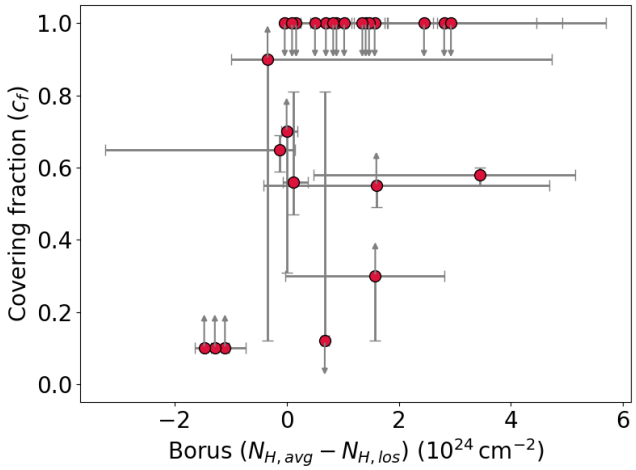

Figure 12. Correlation between covering factor (c_f) and the difference between average and line-of-sight column densities as obtained from `Borus02`.

—Despite markedly different geometric assumptions, the three torus models tested here — `MyTorus`, `Borus02`, and `UXCLUMPY`— deliver broadly consistent line-of-sight column densities for the 26 AGN. Pairwise comparisons of $N_{\rm H,los}$ are tightly correlated ($\rho = 0.95$, 0.97, and 0.93 for `MyTorus` vs. `Borus02`, `MyTorus` vs. `UXCLUMPY`, and `Borus02` vs. `UXCLUMPY`), indicating that this quantity is largely robust to the choice of geometry (see Fig. 4, and Fig. 5). The places where the models start to part ways are exactly where one would expect: near the Compton-thick boundary. There, `Borus02` tends to flag more CT candidates than `MyTorus` or `UXCLUMPY`, underscoring how geometry and covering factor assumptions can tip borderline cases across the threshold. According to all three models, ESO 362-8 is robustly classified as a confirmed CT-AGN.

—Using $\Delta N_{\rm H} = \log N_{\rm H,avg} - \log N_{\rm H,los}$ to compare line-of-sight and global obscuration, we find a clear prevalence of $N_{\rm H,avg} > N_{\rm H,los}$ among sources that can be reliably classified. In `MyTorus`, 11/26 (42.3%) sources show $N_{\rm H,avg} > N_{\rm H,los}$ versus 4/26 (15.4%) with the opposite trend (11/26, 42.3% uncertain); restricting to classified objects, this corresponds to 11/15 (73.3%). In `Borus02`, the numbers are 13/26 (50.0%) vs. 4/26 (15.4%) (9/26, 34.6% uncertain), i.e. 13/17 (76.5%) among the classified (see Fig. 6). This pattern – together with the frequent extension of $N_{\rm H,avg}$ into the $10^{24}\,{\rm cm}^{-2}$ regime even for many Compton-thin lines of sight – supports a picture in which the global torus is typically more heavily obscured than the particular sight line, as expected for a clumpy and anisotropic structure (with occasional $N_{\rm H,los} > N_{\rm H,avg}$ events plausibly linked to transient dense clouds). Overall, the two models deliver consistent classifications where constraints are robust, indicating the view that a clumpy, globally Compton-thick reflector commonly coexists with sight lines of lower column density.

—We evaluated the performance of mid-IR/X-ray diagnostics from Asmus et al. (2015) against machine learning (ML) predictions for $N_{\rm H,los}$, based on multi-wavelength observables by Silver et al. (2023) (Fig. 7, 8). We found that while the Asmus method provides a broadly reliable first-order prediction, especially for heavily obscured sources ($\log {\rm N_H} \gtrsim 23.5$ cm^{-2}), the ML approach– when trained on a diverse parameter space– achieves improved accuracy in estimating $N_{\rm H}$, specially for Compton-thin to moderately thick regions ($\log {\rm N_H} \lesssim$

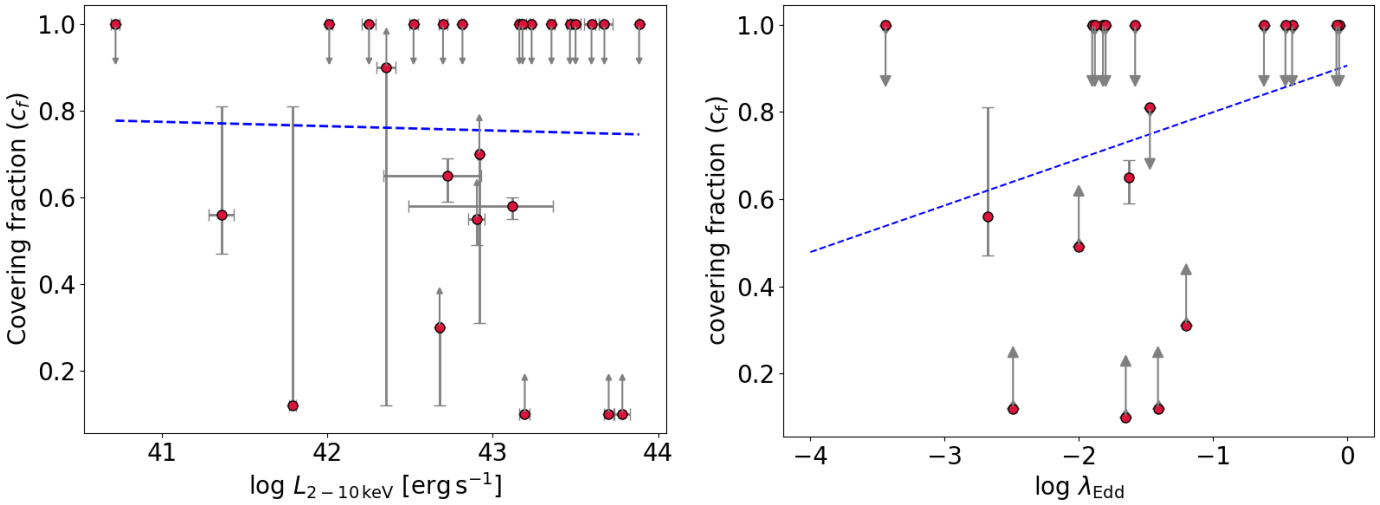

Figure 13. Left panel: Correlation between 2-10 keV intrinsic luminosity and the covering factor. Right panel: Correlation between the covering fraction and the Eddington ratio. The blue dashed line shows the linear regression fit to the data.

23.5 cm^{-2}). This highlights the potential of data-driven techniques to complement or refine empirical diagnostics in AGN classification and obscuration studies.

—Across the sample, the photon indices inferred from the three torus models show overall qualitative agreement, with most sources clustering around the one-to-one relation (Fig. 9). Nonetheless, `MyTorus` tends to return systematically steeper continua than `UXCLUMPY`, whereas `Borus02` and `UXCLUMPY` are mutually more consistent. We do not find evidence for a correlation between Γ and $N_{\mathrm{H,los}}$ in any model (Fig. 10), indicating that spectral slope and line-of-sight obscuration are effectively decoupled in our broadband fits.

—Finally, we find no robust correlations between c_f and $N_{\mathrm{H,los}}$, $N_{\mathrm{H,avg}}$, 2–10 keV intrinsic luminosity, or Eddington ratio; formal rank tests either are not significant or are driven by poorly constrained/censored c_f values.

In summary, our analysis supports a clumpy torus structure as a dominant geometry in obscured AGN, provides new constraints on the physical parameters of the obscuring material, and demonstrates the utility of modern ML techniques in predicting AGN column densities. These findings contribute to a more nuanced understanding of obscured accretion and AGN unification, and motivate future multiwavelength follow-up studies to capture the nature of AGN torus.

ACKNOWLEDGMENTS

IP, MA, IC acknowledge funding under NASA contract 80NSSC24K0633 and SAO contract AR4-25009X. This research made use of data obtained with the *NuSTAR* mission, a project led by the California Institute of Technology, managed by the Jet Propulsion Laboratory, and funded by the National Aeronautics and Space Administration (NASA). It also made use of observations from XMM-*Newton*, an ESA science mission with instruments and contributions funded by ESA Member States and NASA. In addition, this work is based on data obtained with the *Chandra* X-ray Observatory. The authors further acknowledge the use of public data from the *Swift* data archive.

Facilities: *NuSTAR*, XMM-*Newton*, *Chandra*, *Swift*

Software: HEASoft (Nasa High Energy Astrophysics Science Archive Research Center (Heasarc) 2014)), XSPEC (Arnaud 1996), NUSTARDAS (https://heasarc.gsfc.nasa.gov/docs/nustar/analysis/), SAS (Gabriel et al. 2004), CIAO (Fruscione et al. 2006)

APPENDIX

A. SOURCE DESCRIPTION

In the appendix, we describe the results obtained via X-ray spectral fitting, and compare them to previous determinations (when available).

MRK 1073: MRK 1073 is a nearby ($z = 0.0233$) Seyfert 2 AGN, with a black hole mass of $\log(M_{\rm BH}/M_\odot) = 7.78\pm0.50$ (Dasyra et al. 2011). The bolometric luminosity ($L_{\rm bol}$) and Eddington ratio ($\lambda_{\rm Edd}$) reported by Yamada et al. (2020) are $7.8^{+4.4}_{-3.8} \times 10^{43}$ erg s^{-1} and $0.10^{+0.25}_{-0.07}$, respectively. In this work, we analyze archival *NuSTAR* and XMM-*Newton* observations of MRK 1073 spanning from 2002 to 2020. One *NuSTAR* observation was obtained in 2014, while among the three XMM-*Newton* observations, one in 2002 and the remaining two in 2020. Previous X-ray analyses have suggested that MRK 1073 hosts a CT-AGN (Guainazzi et al. 2005; Fukazawa et al. 2011; Yamada et al. 2020; Ricci et al. 2021). Using the `XCLUMPY` model (Tanimoto et al. 2019), Yamada et al. (2020) analyzed the *NuSTAR* data along with one XMM-*Newton* observation (ObsID: 0002942401) and reported $N_{\rm H,los} = 5.4^{+7.0}_{-3.1} \times 10^{24}$ cm^{-2} and $N_{\rm H,avg} = 15.0^{+19.0}_{-9.0} \times 10^{24}$ cm^{-2}, thereby supporting the Compton-thick nature of the source. Our analysis of the joint *NuSTAR* and XMM-*Newton* spectra of MRK 1073 using the `UXCLUMPY` model is consistent with the CT classification reported in previous studies with $N_{\rm H,los} = 3.16^{+7.84}_{-1.04} \times 10^{24}$ cm^{-2} (see Table 3). However, `MyTorus` and `Borus02` yielded $N_{\rm H,los}$ of $2.44^{+u}_{-0.78} \times 10^{24}$ cm^{-2} and $5.88^{+u}_{-2.41} \times 10^{24}$ cm^{-2}, respectively, leaving the CT classification uncertain due to the unconstrained upper limits. While, the IR–X-ray correlation analysis in Asmus et al. (2015) classified this source as CT with $\log(N_{\rm H,l.o.s}/{\rm cm}^{-2}) = 24.45$, the ML algorithm (Silver et al. 2023), retrieved a lower value for $\log(N_{\rm H,l.o.s}/{\rm cm}^{-2}) = 23.01$. To account for the additional nuclear emission in the soft X-ray band, we include a `mekal` component in our analysis. To model the Fe Kβ emission line around ∼7.1 keV, we add a Gaussian component (`zgauss`) with a fixed line width of $\sigma = 100$ eV. The best-fit line energy we obtained is $6.77^{+0.57}_{-0.19}$ keV. Allowing the line width to vary during the fitting process does not significantly affect the fit statistics. Furthermore, the common parameters obtained from modeling the source spectra using three different torus models show good agreement with each other, strengthening the robustness of our results.

UGC 5101: This nearby Seyfert 2 AGN ($z = 0.0393$) was observed by *NuSTAR* twice, in 2014 and 2020, respectively. It hosts a supermassive black hole with a mass of $\log(M_{\rm BH}/M_\odot) \sim 8.35$ (Koss et al. 2017), and an Eddington ratio of $\lambda_{\rm Edd} = 0.014$ (Tanimoto et al. 2022). For the soft X-ray (0.5-10 keV) spectral analysis, we use archival *Chandra* observation taken in 2001. Using the `XCLUMPY` model, Tanimoto et al. (2022) analyzed *NuSTAR* and *Suzaku* data of this source, and reported $N_{\rm H,los} = 1.53^{+0.53}_{-0.09} \times 10^{24}$ cm^{-2} and $N_{\rm H,avg} = 1.72^{+0.51}_{-0.66} \times 10^{24}$ cm^{-2}. Similarly, Oda et al. (2017) utilized XMM-*Newton*, *NuSTAR*, and *Suzaku* observations, and derived $N_{\rm H,los} = 1.31^{+0.31}_{-0.36} \times 10^{24}$ cm^{-2}. More recently, Osorio-Clavijo et al. (2022) analyzed one of the *NuSTAR* observations (ObsID: 60001068002) and reported a line-of-sight column density of $\log(N_{\rm H,l.o.s}/{\rm cm}^{-2}) = 23.84^{+0.06}_{-0.06}$. $N_{\rm H,los}$ and $N_{\rm H,avg}$ obtained from our joint spectral modeling using the `MyTorus`, `Borus02`, and `UXCLUMPY` torus models are both $\sim 10^{24}$ cm^{-2}, indicating a Compton-thick (CT) nature. Using `MyTorus`, `Borus02` and `UXCLUMPY` we obtained $N_{\rm H,los} = 0.80^{+0.38}_{-0.16} \times 10^{24}$ cm^{-2}, $1.35^{+0.45}_{-0.48} \times 10^{24}$ cm^{-2} and $1.17^{+0.27}_{-0.34} \times 10^{24}$ cm^{-2} respectively. Our results are in good agreement with previous studies of the source. The IR–X-ray correlation performed in Asmus et al. (2015) classified the source as CT with $\log(N_{\rm H,l.o.s}/{\rm cm}^{-2}) = 24.46$, while Silver et al. (2023), marked the source as non-CT with $\log(N_{\rm H,l.o.s}/{\rm cm}^{-2}) = 23.21$.

NGC 7674: We used the *NuSTAR*, XMM-*Newton* and *Chandra* observations taken in 2014, 2004 and 2020, respectively, of this source for our analysis. This nearby AGN ($z = 0.02903$) is classified as a type 2 Seyfert with $\log(M_{\rm BH}/M_\odot) \sim 7.73$ (Kammoun et al. 2020). Fitting `MyTorus` in decoupled patchy mode, using *NuSTAR* and XMM-*Newton* observations, Kammoun et al. (2020) reported $N_{\rm H,los} = 0.31^{+0.05}_{-0.07} \times 10^{24}$ cm^{-2} and $N_{\rm H,avg} = 5.7^{+1.0}_{-2.3} \times 10^{24}$ cm^{-2}. Similar results are reported in Jana et al. (2023), who used the `Borus02` model to fit the *NuSTAR* and XMM-*Newton* data, reported $\log(N_{\rm H,l.o.s}/{\rm cm}^{-2}) = 23.61^{+0.25}_{-0.10}$ and $\log(N_{\rm H,avg}/{\rm cm}^{-2}) = 24.57^{+25.50}_{-1.02}$. Using the `XCLUMPY` model to fit the *Suzaku* and *NuSTAR* data Tanimoto et al. (2020) reported $N_{\rm H,los} = 0.24^{+0.22}_{-0.10} \times 10^{24}$ cm^{-2}. Fitting the *NuSTAR* spectrum alone with the `MyTorus` model in decoupled mode, Gandhi et al. (2017) also suggested a Compton-thin line of sight obscurer with $N_{\rm H,los} = 0.13^{+0.03}_{-0.03} \times 10^{24}$ cm^{-2} for NGC 7674. The previous results agree well with our spectral analysis with all three torus models suggested a clumpy nature of the obscuring medium, with $N_{\rm H,los} < 10^{24}$ cm^{-2} and $N_{\rm H,avg} \gtrsim 10^{24}$ cm^{-2} (see Table 3). The three torus models yielded broadly consistent results, with `MyTorus` giving $0.18^{+0.38}_{-0.16} \times 10^{24}$ cm^{-2}, `Borus02` yielding $0.77^{+0.45}_{-0.48} \times 10^{24}$ cm^{-2} and `UXCLUMPY` returning $0.49^{+0.12}_{-0.14} \times 10^{24}$ cm^{-2}. According to the IR–X-ray correlation presented in Asmus et al. (2015) the source was identified as CT-AGN with $\log(N_{\rm H,l.o.s}/{\rm cm}^{-2}) = 24.31$, in contrast to the findings of (Silver et al. 2023), which classified it as non-CT with $\log(N_{\rm H,l.o.s}/{\rm cm}^{-2}) = 23.01$. The spectra of NGC 7674 showed an excess at ∼ 7 keV that possibly corresponds to Fe XXVI. We modeled it by adding a Gaussian emission line. The soft X-ray emission is modeled with a `mekal` component.

IC 2227: The nearby Seyfert 2 galaxy IC 2227 (z = 0.0323) was recently targeted by *NuSTAR* (2022), XMM-*Newton* (2022), and *Chandra* (2021). In this work, we make use of all these observations to fit the source spectra with three different torus model. From an analysis of *NuSTAR* and XMM-*Newton* observations using `MyTorus` (decoupled Face-on), `Borus02`, and `UXCLUMPY`, Silver et al. (2022) reported $N_{\rm H,los}$ values of $0.6^{+0.11}_{-0.07} \times 10^{24}$ cm^{-2}, $0.64^{+0.05}_{-0.06} \times 10^{24}$ cm^{-2}, and $0.63^{+0.10}_{-0.04} \times 10^{24}$ cm^{-2}, respectively. The $N_{\rm H,avg}$ values obtained from the `MyTorus` and `Borus02` fits were $6.06^{+u}_{-2.84} \times 10^{24}$ cm^{-2} and $31.62^{+u}_{-26.00} \times 10^{24}$ cm^{-2}, respectively. The best-fitted parameters obtained from our analysis are in close agreement with the previous results with $N_{\rm H,los} = 0.42^{+0.07}_{-0.05} \times 10^{24}$ cm^{-2} using `MyTorus`, $0.65^{+0.07}_{-0.12} \times 10^{24}$ cm^{-2} from `Borus02` and $0.59^{+0.11}_{-0.09} \times 10^{24}$ cm^{-2} using `UXCLUMPY`. From spectral modeling with `MyTorus` and `Borus02` $N_{\rm H,avg}$ estimated to be $1.26^{+0.42}_{-0.27} \times 10^{24}$ cm^{-2} and $1.35^{+0.30}_{-0.53} \times 10^{24}$ cm^{-2}, suggesting a patchy torus scenario with a Compton-thin $N_{\rm H,los}$ and $N_{\rm H,avg} \gtrsim 10^{24}$ cm^{-2} (see Table 3). Based on the IR–X-ray correlation, Asmus et al. (2015) placed the source in the CT class with $\log(N_{\rm H,l.o.s}/{\rm cm}^{-2}) = 24.45$, whereas the ML algorithm in Silver et al. (2023) identified it as non-CT, finding $\log(N_{\rm H,l.o.s}/{\rm cm}^{-2}) = 23.60$. The soft X-ray emission in the spectra of IC 2227 is modeled with a `mekal` component with kT$_{\rm e} \sim 0.6$ keV.

ESO 362-8: This nearby ($z = 0.0150$) Sy 2 AGN has been observed once with *NuSTAR* in 2021 and twice with XMM-*Newton*in 2006 and 2021, respectively. We used all the observations to fit the source spectra using the three torus models. From the analysis of the *NuSTAR* and one XMM-*Newton* observation (Obs ID - 0890440101), Silver et al. (2022) reported $N_{\rm H,los} = 2.78^{+u}_{-0.65} \times 10^{24}$ cm^{-2}, $3.96^{+u}_{-1.30} \times 10^{24}$ cm^{-2} and $3.93^{+u}_{-1.41} \times 10^{24}$ cm^{-2} using `MyTorus` (decoupled Face-on), `Borus02` and `UXCLUMPY` respectively. The authors retrieved $N_{\rm H,avg}$ of $9.91^{+u}_{-5.66} \times 10^{24}$ cm^{-2} and $10.00^{+0.15}_{-4.75} \times 10^{24}$ cm^{-2}, using `MyTorus` and `Borus02`. Our analysis also revealed the CT nature of the source with both $N_{\rm H,los}$ and $N_{\rm H,avg} \gtrsim 10^{24}$ cm^{-2} (see Table 3. The best-fitted parameters obtained from the three models are in agreement, and retrieved a relatively soft spectrum with $\Gamma \sim 2.00$. Using `MyTorus`, `Borus02`, and `UXCLUMPY`, we derived $N_{\rm H,los} = 6.74^{+u}_{-6.20} \times 10^{24}$ cm^{-2}, $2.31^{+1.69}_{-0.72} \times 10^{24}$ cm^{-2} and $2.96^{+2.88}_{-0.95} \times 10^{24}$ cm^{-2}, respectively. While Asmus et al. (2015) used IR–X-ray scaling relations to classify the source as CT with $\log(N_{\rm H,l.o.s}/{\rm cm}^{-2}) = 24.19$, an analysis by Silver et al. (2023) assigned it to the non-CT category, estimating $\log(N_{\rm H,l.o.s}/{\rm cm}^{-2}) = 23.33$. Fitting the soft X-ray emission with `mekal` produced a plasma temperature (kT$_{\rm e}$) ~ 0.5 keV (see Table 3).

ESO 406-4: This nearby Sy 2 AGN ($z = 0.0297$), with $\log(M_{\rm BH}/M_{\odot}) \sim 8.02 \pm 0.02$ (Koss et al. 2022), is a well-studied source. In this work, we make use of observations from *NuSTAR*, XMM-*Newton*, and *Chandra*. The dataset includes two *NuSTAR* observations taken in 2016 and 2020, one XMM-*Newton* observation from 2021, and an earlier *Chandra* observation from 2012. The obscuration properties of this source have been debated: some studies suggest a CT-AGN classification based on spectral modeling with the torus model of Brightman & Nandra (2011), yielding $\log(N_{\rm H,l.o.s}/{\rm cm}^{-2}) = 24.74^{+u}_{-0.55}$ (Ricci et al. 2015), or based on spectral curvature estimates (Koss et al. 2016). More recent works, however, including Akylas et al. (2016); Tanimoto et al. (2022); Sengupta et al. (2023), do not confirm the CT nature of the obscurer. Using the torus model of Brightman & Nandra (2011), and fitting the *Swift*-XRT and `BAT` spectra, Akylas et al. (2016) reported a Compton-thin obscurer with $N_{\rm H,los} = 0.32^{+0.20}_{-0.11} \times 10^{24}$ cm^{-2}. Applying the `XCLUMPY` model to the Swift and *NuSTAR* data, Tanimoto et al. (2022) reported $N_{\rm H,los} = 0.54^{+5.82}_{-0.14} \times 10^{24}$ cm^{-2}. Similarly, Sengupta et al. (2023) reported $N_{\rm H,los} = 0.73^{+0.27}_{-0.14} \times 10^{24}$ cm^{-2} using `MyTorus` and $0.79^{+0.04}_{-0.12} \times 10^{24}$ cm^{-2} using `Borus02`, based on the two *NuSTAR* and one *Chandra* observations. In the present work, we include for the first time the XMM-*Newton* observation in a joint fit with the three torus models. We find consistent results across `MyTorus`, `Borus02`, and `UXCLUMPY`, with line-of-sight column densities of $1.06^{+0.87}_{-0.53} \times 10^{24}$ cm^{-2}, $1.34^{+0.85}_{-0.40} \times 10^{24}$ cm^{-2}, and $1.16^{+0.56}_{-0.35} \times 10^{24}$ cm^{-2}, respectively. Although the best-fit $N_{\rm H,los}$ values suggest a CT nature, the large uncertainties prevent a definitive confirmation. Likewise, the large error bars on $N_{\rm H,avg}$ hinder any firm conclusion on the clumpy nature of the torus, with $N_{\rm H,avg}$ estimated at $1.01^{+8.98}_{-0.99} \times 10^{24}$ cm^{-2} and $1.00^{+u}_{-0.51} \times 10^{24}$ cm^{-2} from the `MyTorus` and `Borus02` fits, respectively. Based on the IR–X-ray correlation, Asmus et al. (2015) placed the source in the CT class with $\log(N_{\rm H,l.o.s}/{\rm cm}^{-2}) = 24.28$; however, employing a ML technique, Silver et al. (2023) concluded that the source belongs to the non-CT class with $\log(N_{\rm H,l.o.s}/{\rm cm}^{-2}) = 23.360$.

2MFGC 13496: This nearby ($z = 0.0407$) emission line galaxy is observed by *NuSTAR*, XMM-*Newton* and *Chandra* between 2015 and 2019. The nature of the obscuration for this galaxy is studied for the first time in this work. Using the three models, we find that $N_{\rm H,los} \lesssim 10^{24}$ cm^{-2}, thus allowing us to flag this source as Compton-thin. In our fits, the estimated line-of-sight column densities spanned a narrow range: `MyTorus` indicated $0.73^{+0.27}_{-0.19} \times 10^{24}$ cm^{-2}, `Borus02` estimated $1.15^{+0.34}_{-0.25} \times 10^{24}$ cm^{-2}, and `UXCLUMPY` found $0.59^{+0.20}_{-0.08} \times 10^{24}$ cm^{-2}. However, the $N_{\rm H,avg}$ obtained from the `MyTorus` and `Borus02` fits is even smaller, being $2.00^{+5.00}_{-u} \times 10^{22}$ cm^{-2} and $5.00^{+15.00}_{-u} \times 10^{22}$ cm^{-2},

respectively, thus supporting a clumpy torus scenario. The IR–X-ray correlation presented in Asmus et al. (2015), reported $\log(N_{\rm H,l.o.s}/{\rm cm}^{-2}) = 23.99$, while Silver et al. (2023) estimated $\log(N_{\rm H,l.o.s}/{\rm cm}^{-2}) = 23.64$ using their ML algorithm.

2MASX J03585442+1026033: This nearby Seyfert 2 galaxy ($z = 0.031$) with $\log(M_{\rm BH}/M_{\odot}) \sim 7.75$ (Hernández-García et al. 2015) has been observed by *NuSTAR* once in 2014, twice by XMM-*Newton* in 2002 and 2003, and once by *Chandra* in 2008. From an analysis of the two XMM-*Newton* and one *Chandra* observations using an absorbed power-law, Hernández-García et al. (2015) classified the source as a Compton-thin AGN with $N_{\rm H,los} \sim 10^{22}$ cm^{-2}. We analyzed all the observations and our analysis using all three models features the Compton-thin nature of the source with $N_{\rm H,los} = 0.11^{+0.01}_{-0.01} \times 10^{24}$ cm^{-2} using `MyTorus`, $N_{\rm H,los} = 0.11^{+0.08}_{-0.07} \times 10^{24}$ cm^{-2} using `Borus02`, and $N_{\rm H,los} = 0.11^{+0.01}_{-0.01} \times 10^{24}$ cm^{-2} from `UXCLUMPY` fits. $N_{\rm H,avg}$ obtained from the `MyTorus` and `Borus02` analyses has the similar set of values ($N_{\rm H,avg} = 0.40^{+0.75}_{-0.35} \times 10^{24}$ cm^{-2} and $0.11^{+0.18}_{-0.07} \times 10^{24}$ cm^{-2}, respectively) as of $N_{\rm H,los}$, indicating an uniform density torus. Both the IR–X-ray correlation in Asmus et al. (2015) and the analysis of Silver et al. (2023) classified the source as non-CT, with $\log(N_{\rm H,l.o.s}/{\rm cm}^{-2}) = 23.06$ and 23.25, respectively. The soft part of the spectra is modeled using a `mekal` component with $kT_e \sim 0.30$ keV (see Table 3).

M 58: This well studied LINER Type 1.9 AGN ($z = 0.005$), with $\log(M_{\rm BH}/M_{\odot}) \sim 8.10$, has been observed once by *NuSTAR* in 2016 and twice by XMM-*Newton* and *Chandra*, respectively between 2000 and 2016. We have analyzed all the observations using three torus models. Previous analyses have suggested a very low line-of-sight column density. For instance, from the spectral analysis of the *NuSTAR* and one XMM-*Newton* observation (ObsID: 0790840201) using `Borus02`, Jana et al. (2023) reported $\log N_{\rm H,l.o.s/cm^{-2}} = 20.00$ (fixed) and $\log N_{\rm H,avg/cm^{-2}} = 23.80^{+0.17}_{-0.12}$. On the other hand, using an absorbed power-law with reflection component, Osorio-Clavijo et al. (2022), reported $\log N_{\rm H,los/cm^{-2}} = 22.34^{+0.09}_{-0.11}$. In our analysis, we similarly find evidence for a Compton-thin obscurer with $N_{\rm H,los} \lesssim 10^{22}$ cm^{-2}. Finally, we note that for this source we do not need an additional scattered component to fit the spectra, a result consistent with the almost unobscured nature of the source.

3C 371: This is the only BL LAC source analyzed in this work. This source, located at $z = 0.0495$, was observed once by *NuSTAR* in 2022, and once by *Chandra* in 2000. The three torus models yielded broadly consistent results, with `MyTorus` giving $N_{\rm H,los} = 0.022^{+0.006}_{-0.006} \times 10^{24}$ cm^{-2}, `Borus02` yielding $N_{\rm H,los} = 0.034^{+0.010}_{-0.018} \times 10^{24}$ cm^{-2}, and `UXCLUMPY` estimated $N_{\rm H,los} = 0.025^{+0.001}_{-0.010} \times 10^{24}$ cm^{-2}. the $N_{\rm H,avg}$ obtained from the `MyTorus` and `Borus02` fits are $0.50^{+0.010}_{-0.088} \times 10^{24}$ cm^{-2} and $0.54^{+0.010}_{-0.088} \times 10^{24}$ cm^{-2}, respectively. While the derived column densities differ–$\log N_{\rm H,los/cm^{-2}} = 23.14$ from Asmus et al. (2015) and 22.10 from Silver et al. (2023)– both studies ultimately classified the source as Compton-thin. The soft part of the spectra is modeled using a `mekal` component with $kT_e \sim 0.35$ keV (see Table 3).

IC 1198: IC 1198, a nearby ($z = 0.034$) Sy 1 galaxy, is been studied for the first time in this work to characterize its torus properties. It has a black hole mass of $\log(M_{\rm BH}/M_{\odot}) \sim 7.51$ (Mejía-Restrepo et al. 2022). This source is been observed once each by *NuSTAR* and XMM-*Newton* in 2017 and 2022, respectively. The spectral fit with the three models, `MyTorus`, `Borus02`, and `UXCLUMPY` agrees well and features a Compton-thin nature of the source with $N_{\rm H,los} = 0.11^{+0.01}_{-0.01} \times 10^{24}$ cm^{-2} using `MyTorus`, $0.21^{+0.02}_{-0.02} \times 10^{24}$ cm^{-2} using `Borus02` and $0.11^{+0.01}_{-0.01} \times 10^{24}$ cm^{-2} from the `UXCLUMPY` fits. However, from the `MyTorus` and `Borus02` analysis we obtain a much larger $N_{\rm H,avg}$ of $\gtrsim 10^{24}$ cm^{-2}, indicating a clumpy nature of the torus in IC 1198. Consistently, Asmus et al. (2015) and Silver et al. (2023) both identified the source as Compton-thin with $\log N_{\rm H,los/cm^{-2}} = 23.30$ and 23.05, respectively.

2MASX J09261742-8421330: This nearby ($z = 0.0643$) Sy 2 galaxy has been observed once by *NuSTAR* in 2015. The source has never been observed by either XMM-*Newton*, or *Chandra*. For the soft X-ray band (0.5-10 keV), we therefore used the simultaneous *Swift*-XRT observation with *NuSTAR*. This source has a black hole mass of $\log(M_{\rm BH}/M_{\odot}) = 7.10 \pm 0.02$ (Mejía-Restrepo et al. 2022). From the broadband spectral analysis of the *Swift*-BAT observations Ricci et al. (2017), reported $\log N_{\rm H,los/cm^{-2}} = 22.40^{+0.08}_{-0.12}$. Consistently with previous results reported in Ricci et al. (2017), we also find a Compton-thin line of sight obscuration with $N_{\rm H,los} = 1.4^{+1.0}_{-u} \times 10^{22}$ cm^{-2} using `MyTorus`, $2.1^{+3.4}_{-u} \times 10^{22}$ cm^{-2} using `Borus02`, and $1.3^{+1.3}_{-u} \times 10^{22}$ cm^{-2} from the `UXCLUMPY` fits. From `MyTorus` and `Borus02` we obtain a larger value of $N_{\rm H,avg} \sim 0.9 \times 10^{24}$ cm^{-2}, indicating a possible clumpy nature of the torus. While the derived column densities differ– $\log N_{\rm H,los/cm^{-2}} = 23.33$ from Asmus et al. (2015) and 22.38 from Silver et al. (2023)– both studies ultimately classified the source as non-CT AGN.

UGC 12348: This nearby ($z = 0.0253$) Seyfert 2 galaxy is analyzed for the first time in this study to explore the nature of its obscuration. It was observed simultaneously by *NuSTAR* and XMM-*Newton* in 2014, and later by *Chandra* in

2020. Our spectral analysis using all three datasets shows consistent values of $N_{\rm H,los}$ and $N_{\rm H,avg}$, suggesting a uniform torus structure. In our fits, the estimated line-of-sight column densities spanned a narrow range: `MyTorus` indicated $N_{\rm H,los} = 0.023^{+0.002}_{-0.001} \times 10^{24}$ cm^{-2}, , `Borus02` suggested $N_{\rm H,los} = 0.044^{+0.018}_{-0.015} \times 10^{24}$ cm^{-2}, and `UXCLUMPY` found $N_{\rm H,los} = 0.027^{+0.027}_{-0.025} \times 10^{24}$ cm^{-2}. Therefore, all models agree on a Compton-thin obscuration ($N_{\rm H,los} < 10^{24}$ cm^{-2}). The IR–X-ray correlation analysis by Asmus et al. (2015) and the more recent study by Silver et al. (2023) arrived at the same classification of the source as Compton-thin, with estimated column densities of $\log N_{\rm H,los/cm^{-2}} = 23.35$ and 22.71, respectively. To model the soft X-ray emission, we included a `mekal` component with kT$_{\rm e} \sim 0.70$ keV.

2MASX J02420381+0510061: This nearby Seyfert 2 AGN ($z = 0.073$) was observed simultaneously with *NuSTAR* and XMM-*Newton* in 2017, and later by *Chandra* in 2022. Previously Ricci et al. (2017) reported $N_{\rm H,los} = 3.16^{+2.46}_{-0.65} \times 10^{23}$ cm^{-2} using an absorbed cut-off power-law model. In our analysis, all three torus models yield a Compton-thin line-of-sight column density around 10^{23} cm^{-2}, with $N_{\rm H,los} = 8.1^{+1.5}_{-1.4} \times 10^{23}$ cm^{-2}. from `MyTorus`, $N_{\rm H,los} = 12.9^{+2.5}_{-2.2} \times 10^{23}$ cm^{-2} from `Borus02`, and $N_{\rm H,los} = 9.8^{+6.0}_{-2.5} \times 10^{24}$ cm^{-2} from `UXCLUMPY`. Despite yielding different numerical estimates– $\log N_{\rm H,los/cm^{-2}} = 23.45$ in Asmus et al. (2015) and 22.39 in Silver et al. (2023)– both analyses classified the source as non-CT candidate.

ESO 234-50: This Seyfert 2 AGN ($z = 0.009$) was observed by *NuSTAR* in May 2021 and by *Chandra* in March 2021. The black hole mass is estimated to be $\log(M_{\rm BH}/M_{\odot}) \sim 6.04 \pm 0.07$ Koss et al. (2022). From the broad-band spectral analysis of the Swift observations, Ricci et al. (2017) reported $N_{\rm H,los} = 1.20^{+0.38}_{-0.41} \times 10^{23}$ cm^{-2}. Our results for $N_{\rm H,los}$ - $0.22^{+0.05}_{-0.05} \times 10^{24}$ cm^{-2} from `MyTorus`, $0.32^{+0.07}_{-0.05} \times 10^{24}$ cm^{-2} from `Borus02`, and $0.20^{+0.02}_{-0.03} \times 10^{24}$ cm^{-2} from `UXCLUMPY`- are in agreement with this value. The IR–X-ray correlation analysis (Asmus et al. 2015) and the more recent study by Silver et al. (2023) arrived at the same classification of the source as Compton-thin, with estimated column densities of $\log N_{\rm H,los/cm^{-2}} = 23.50$ and 23.21, respectively.

NGC 2273: This nearby Seyfert 2 AGN ($z = 0.0061$) has multiple archival observations: one by *NuSTAR* in 2014, three by XMM-*Newton* in 2003, and one by *Chandra* in 2017. We used all of them in our joint spectral analysis. The black hole mass is $\log(M_{\rm BH}/M_{odot}) \sim 8.22 \pm 0.03$ (Koss et al. 2022). A *NuSTAR*-only analysis by Osorio-Clavijo et al. (2022), using a partial covering continuum model with a reflection component, classified the source as Compton-thick with $N_{\rm H,los} \sim 2 \times 10^{25}$ cm^{-2}. Williams et al. (2022) reported a cold absorber with $N_{\rm H} < 0.16 \times 10^{22}$ cm^{-2} and a warm absorber with $N_{\rm H} = 15.69^{+5.74}_{-8.36} \times 10^{22}$ cm^{-2}. In our fits, the estimated line-of-sight column densities spanned a narrow range: `MyTorus` indicated $N_{\rm H,los} = 0.37^{+0.11}_{-0.06} \times 10^{24}$ cm^{-2}, `Borus02` suggested $N_{\rm H,los} = 0.31^{+0.11}_{-0.13} \times 10^{24}$ cm^{-2}, and `UXCLUMPY` found $N_{\rm H,los} = 0.35^{+0.05}_{-0.07} \times 10^{24}$ cm^{-2}. To investigate the discrepancy with Osorio-Clavijo et al. (2022), we fitted the *NuSTAR* spectrum from 2014 and the XMM-*Newton* spectra from 2003 separately with the `UXCLUMPY` model to check for possible variability in $N_{\rm H,los}$. The *Chandra* data did not contain enough counts to allow a separate analysis. The individual *NuSTAR* and XMM-*Newton* fits with `UXCLUMPY` could not constrain most spectral parameters, including $N_{\rm H,los}$. The *NuSTAR*-only fit gave $N_{\rm H,los} = 5.02^{+u}_{-4.65} \times 10^{25}$ cm^{-2}, while the XMM-*Newton*-only fit yielded $N_{\rm H,los} = 4.47^{+u}_{-2.68} \times 10^{24}$ cm^{-2}. Although $N_{\rm H,los}$ is poorly constrained with the `UXCLUMPY` model and the lower limit prevents us from drawing firm conclusions about variability between observations, the discrepant values nonetheless make NGC 2273 a promising candidate for future studies of line-of-sight absorption variability with improved data quality. Based on the IR–X-ray correlation, Asmus et al. (2015) placed the source in the CT class with $\log N_{\rm H,los/cm^{-2}} = 24.18$, a later analysis by Silver et al. (2023), estimated $\log N_{\rm H,los/cm^{-2}} = 23.83$. The soft X-ray component of NGC 2273 was modeled using a `mekal` component with $kT_e \sim 0.30$ keV (see Table 3).

FRL 265: This type 1 Seyfert galaxy ($z = 0.0295$) was observed by *NuSTAR* in 2019. We did not use the 2022 XMM-*Newton* data due to contamination from extended emission. This is the first study of the circumnuclear matter in this source. The three torus models yielded broadly consistent results, with `MyTorus` producing $N_{\rm H,los} = 0.010^{+0.004}_{-u} \times 10^{24}$ cm^{-2}, `Borus02` yielding a upper-limit of $N_{\rm H,los} < 0.06 \times 10^{24}$ cm^{-2}, and `UXCLUMPY` estimating $N_{\rm H,los} = 0.01^{+0.23}_{-0.06} \times 10^{24}$ cm^{-2}. Using `MyTorus` and `Borus02`, we obtained $N_{\rm H,avg} = 2.00^{+2.95}_{-0.99} \times 10^{24}$ cm^{-2} and $1.51^{+0.34}_{-0.31} \times 10^{24}$ cm^{-2}, respectively. A clear difference between $N_{\rm H,los}$ and $N_{\rm H,avg}$ (from `MyTorus` and `Borus02`) suggests we observe the AGN through a less dense region, supporting a clumpy-torus model.

MRK 231: Located at $z = 0.042$, this Seyfert 1 galaxy is known for strong winds and outflows (Leighly et al. 2014; Yamada et al. 2024). It has been observed multiple times by *NuSTAR* and XMM-*Newton* (see Table 2). To avoid the complexity of the joint fit due to variable nature of soft X-ray source spectrum below 10 keV (Braito et al. 2004), we used only *NuSTAR* data for spectral analysis. However, results from joint *NuSTAR* and XMM-*Newton* fits are

consistent. Analysis of contemporaneous *Chandra* and *NuSTAR* broadband spectra Teng et al. (2014) revealed strong X-ray emission associated with a powerful circumnuclear starburst. The direct AGN emission is absorbed and scattered by a patchy, Compton-thin torus with $N_{\rm H} \sim 1.2^{+0.3}_{-0.3} \times 10^{23}$ cm^{-2}. In contrast, Braito et al. (2004) concluded, based on their modeling of the 0.5-50 keV broadband spectrum, that MRK 231 is a CT quasar with a column density of $\sim$ 1.8-2.6 $\times$ 10^{24} cm^{-2}. However, they also suggested that the variability observed below 10 keV is consistent with changes in the partial covering fraction of the Compton-thick absorber. Our analysis of only *NuSTAR* observations agrees well with the recent findings of Teng et al. (2014) with $N_{\rm H,los} = 0.06^{+0.03}_{-0.02} \times 10^{24}$ cm^{-2} from `MyTorus`, $0.10^{+0.02}_{-0.02}$ $\times$ 10^{24} cm^{-2} from `Borus02`, and $0.07^{+0.02}_{-0.02} \times 10^{24}$ cm^{-2} from `UXCLUMPY`. However, The IR–X-ray correlation analysis (Asmus et al. (2015)) and the more recent study by Silver et al. (2023) arrived at the same classification of the source as CT-AGN, with estimated column densities of $\log N_{\rm H,los/cm^{-2}} = 24.69$ and $\log N_{\rm H,los/cm^{-2}} = 24.34$, respectively.

PG 1211+143: This bright, nearby ($z = 0.081$) narrow-line Seyfert 1 galaxy has multiple observations from *NuSTAR* and XMM-*Newton*, that were taken in 2014. Reeves et al. (2018) reported variable soft X-ray outflows using XMM-*Newton* data, so we excluded the XMM-*Newton* observations from our analysis. Reverberation mapping results from Peterson et al. (2004) and Campitiello et al. (2020) estimate $\log(M_{\rm BH}/M_\odot) \sim 8.6$. The three torus models yielded broadly consistent results, with `MyTorus` giving $N_{\rm H,los} = 0.04^{+0.01}_{-0.01} \times 10^{24}$ cm^{-2}, `Borus02` yielding $N_{\rm H,los} = 0.04^{+0.01}_{-0.02}$ $\times$ 10^{24} cm^{-2}, and `UXCLUMPY` estimating $N_{\rm H,los} = 0.14^{+0.05}_{-0.04} \times 10^{24}$ cm^{-2} from `UXCLUMPY`. While Asmus et al. (2015) used IR–X-ray scaling relations to classify the source as Compton-thin with $\log N_{\rm H,los/cm^{-2}} = 23.25$, a later analysis by Silver et al. (2023) estimating a lower value for $\log N_{\rm H,los/cm^{-2}} = 21.99$.

MRK 376: MRK 376 is a nearby ($z = 0.056$) Seyfert 1.5 galaxy with a black hole mass $\log(M_{\rm BH}/M_\odot) \sim 8.22$ (Koss et al. 2022). This source was observed by *NuSTAR* and *Swift*-XRT in 2015. Ricci et al. (2017) reported a Compton-thin $N_{\rm H,los} \sim 8.71^{+5.41}_{-3.47} \times 10^{22}$ cm^{-2}, consistent with our findings. We also estimate a Compton-thick $N_{\rm H,avg} \sim 2.00 \times 10^{24}$ cm^{-2}, suggesting a patchy torus. Both the IR–X-ray correlation in Asmus et al. (2015) and the analysis of Silver et al. (2023) classified the source as Compton-thin, with $\log N_{\rm H,los/cm^{-2}} = 23.51$ and 22.48, respectively. The soft X-ray emission is modeled with a `mekal` component ($kT_e \sim 0.2$ keV).

NGC 7378: This type 2 AGN at $z = 0.009$ was observed by *NuSTAR* in December, 2018. For the soft X-ray analysis (0.5–10 keV), we used the *Swift*-XRT observations taken quasi-simultaneously with *NuSTAR* in between December and January of 2018. Koss et al. (2022) estimated $\log(M_{\rm BH}/M_\odot) = 5.49 \pm 0.16$, making this an AGN powered by an intermediate mass black hole . We find $N_{\rm H,los} \sim 10^{23}$ cm^{-2} and $N_{\rm H,avg} \sim 3 \times 10^{24}$ cm^{-2}, indicating a patchy torus. No previous $N_{\rm H}$ measurements are reported in the literature for this target. Consistently, Asmus et al. (2015) and Silver et al. (2023) both identified the source as Compton-thin AGN, with $\log N_{\rm H,los/cm^{-2}} = 23.18$ and 22.85, respectively.

2MASX J11462959+7421289: This nearby Seyfert 2 AGN ($z = 0.058$) was observed quasi-simultaneously by *NuSTAR* and *Swift*-XRT in 2013. Koss et al. (2022) reported $\log(M_{\rm BH}/M_\odot) = 8.22 \pm 0.03$. No previous $N_{\rm H}$ measurements are available. Our analysis suggests a quasi–unobscured nature for this target, with $N_{\rm H,los} \sim 10^{22}$ cm^{-2}. From spectral modeling with `MyTorus`, `Borus02`, and `UXCLUMPY`, the line-of-sight column densities were estimated to be $0.010^{+0.003}_{-u}$ $\times$ 10^{24} cm^{-2}, $0.013^{+0.060}_{-0.010} \times 10^{24}$ cm^{-2}, and $0.045^{+0.007}_{-0.010} \times 10^{24}$ cm^{-2}, respectively. The IR–X-ray correlation in Asmus et al. (2015) classified the source as Compton-thin AGN with $\log N_{\rm H,los/cm^{-2}} = 23.05$, while Silver et al. (2023) also reported it as Compton-thin with a lower $\log N_{\rm H,los/cm^{-2}} = 21.89$.

SWIFT J2006.5+5619: This Seyfert 2 AGN ($z = 0.044$) was observed by *NuSTAR* and by *Swift*-XRT in 2014. Its black hole mass is $\log(M_{\rm BH}/M_\odot) \sim 7.07 \pm 0.11$ Koss et al. (2022). Previous analyses by Ricci et al. (2017) and Panagiotou et al. (2021) found $N_{\rm H,los}$ values around 1.8–3.0 $\times$ 10^{23} cm^{-2}, consistent with our result of $N_{\rm H,los}$ as estimated to be $0.15^{+0.04}_{-0.03} \times 10^{24}$ cm^{-2}, $0.31^{+0.09}_{-0.11} \times 10^{24}$ cm^{-2}, and $0.19^{+0.04}_{-0.05} \times 10^{24}$ cm^{-2}, respectively, using `MyTorus`, `Borus02` and `UXCLUMPY`. Consistently, Asmus et al. (2015) and Silver et al. (2023) both identified the source as Compton-thin AGN, with $\log N_{\rm H,los/cm^{-2}} = 23.08$ and 23.06, respectively.

2MASX J06363227-2034532: This Seyfert 2 AGN at $z = 0.056$ was observed quasi-simultaneously by *NuSTAR* and *Swift*-XRT in Spetember, 2023. The black hole mass is $\log(M_{\rm BH}/M_\odot) \sim 8.44 \pm 0.15$ Koss et al. (2022). All three models indicate a Compton-thick nature with $N_{\rm H,los} \sim 1.0 \times 10^{24}$ cm^{-2} (Table 3), matching Sambruna et al. (1999) who found $N_{\rm H,los} = 7.9^{+12.9}_{-4.3} \times 10^{23}$ cm^{-2} from *ASCA* data. The soft X-rays are modeled using a `mekal` component ($kT_e \sim 0.20$ keV). According to the IR–X-ray correlation presented in Asmus et al. (2015), the source was identified as CT-AGN with $\log N_{\rm H,los/cm^{-2}} = 24.15$, in contrast to the findings of Silver et al. (2023), which classified it as Compton-thin with $\log N_{\rm H,los/cm^{-2}} = 23.34$.

2MASX J09034285-7414170: *NuSTAR* observed this nearby ($z = 0.093$) Seyfert 2 AGN in 2015, while in the soft band the source has been targeted multiple times by *Swift*-XRT in 2015. The black hole mass is $\log(M_{\rm BH}/M_{\odot}) = 7.88 \pm 0.17$ Koss et al. (2022). In our fits, the estimated line-of-sight column densities spanned a narrow range: `MyTorus` indicated $N_{\rm H,los} = 0.40^{+0.22}_{-0.21} \times 10^{24}$ cm^{-2}, `Borus02` suggested $N_{\rm H,los} = 0.49^{+0.21}_{-0.17} \times 10^{24}$ cm^{-2}, and `UXCLUMPY` estimated $N_{\rm H,los} = 0.34^{+0.17}_{-0.16} \times 10^{24}$ cm^{-2}. These findings are consistent with Ricci et al. (2017) who reported $N_{\rm H,los} \sim 3.89 \times 10^{23}$ cm^{-2} for this source. Our results suggest a patchy torus with $N_{\rm H,los} \sim 4.0 \times 10^{23}$ cm^{-2} and $N_{\rm H,avg} \sim 2.0 \times 10^{24}$ cm^{-2} from modeling the source spectra with `MyTorus` and `Borus02`. Consistently, Asmus et al. (2015) and Silver et al. (2023) both identified the source as Compton-thin AGN, with $\log N_{\rm H,los/cm^{-2}} = 23.25$ and 23.07, respectively.

2MASX J00091156-0036551: This Seyfert 2 AGN ($z = 0.073$) was observed by *NuSTAR* in 2015. *Swift*-XRT observed this source simultaneously with *NuSTAR* once in 2015. The black hole mass is $\log(M_{\rm BH}/M_{\odot}) = 8.54 \pm 0.11$ Koss et al. (2022). Our spectral analysis gives $N_{\rm H,los} \sim 3.0 \times 10^{23}$ cm^{-2}, consistent with Ricci et al. (2017) who found $N_{\rm H,los} \sim 4.07 \times 10^{23}$ cm^{-2}. The classification of this source is consistent across studies: Asmus et al. (2015) inferred $\log N_{\rm H,los/cm^{-2}} = 23.37$, whereas Silver et al. (2023) identified it as Compton-thin with $\log N_{\rm H,los/cm^{-2}} = 23.71$.

Table 2. Summary of the X-ray observations analyzed in this work, for the 26 sources in our sample. The columns are (1) serial number of source, (2) source name, (3) telescopes used for observation, (4) observation ID, (5) exposure time in sec., and (6) date of observation.

Index	Name	Telescope	Obs ID	Exposure (s)	Obs Date
1	MRK 1073	*NuSTAR*	60001161002	22199	2014-10-08
		XMM-Newton	0002942401	7868	2002-01-28
			0862510301	14900	2020-08-20
			0862510701	13800	2020-08-31
2	UGC 5101	*NuSTAR*	60001068004	23214	2020-04-17
		NuSTAR	60001068002	18291	2014-03-21
		Chandra	2033	49930	2001-05-28
3	NGC 7674	*NuSTAR*	60001151002	51997	2014-09-30
		XMM-Newton	0200660101	10420	2004-06-02
		Chandra	23715	2090	2020-09-29
4	IC 2227	*NuSTAR*	60701049002	52172	2022-03-28
		XMM-*Newton*	0890440201	38000	2022-03-27
		Chandra	23723	4380	2021-04-10
5	ESO 362−8	*NuSTAR*	60701048002	48531	2021-10-05
		XMM-*Newton*	0890440101	38000	2021-10-05
			0307001401	18308	2006-02-13
6	ESO 406-4	*NuSTAR*	60201039002	36317	2016-05-25
			60161799002	23719	2020-06-26
		XMM-Newton	0883210401	24000	2021-11-21
		Chandra	14050	5090	2012-06-07
7	2MFGC 13496	*NuSTAR*	60001145002	22866	2015-03-03
		XMM-Newton	0743010301	22800	2015-03-04
		Chandra	22059	10090	2019-01-27
8	2MASX J03585442+1026033	*NuSTAR*	60061042002	27331	2014-09-25
		XMM-Newton	0064600301	11914	2003-02-05
			0064600101	28904	2002-09-07
		Chandra	10234	32130	2008-12-24
9	M 58	*NuSTAR*	60201051002	117843	2016-12-06
		XMM-*Newton*	0790840201	23002	2016-12-06
			0112840101	23669	2003-06-12
		Chandra	406	2940	2000-02-23
			807	35640	2000-05-02
			9558	49450	2008-02-29
10	3C 371	*NuSTAR*	60801044002	17981	2022-06-12
		Chandra	841	10250	2000-03-21
11	IC 1198	*NuSTAR*	60361014002	26973	2017-05-07
		XMM-*Newton*	0903041301	32200	2022-08-29

Table 2 *continued*

Table 2 *(continued)*

Index	Name	Telescope	Obs ID	Exposure (s)	Obs Date
12	2MASX J09261742-8421330	*NuSTAR*	60160360002	35127	2015-11-30
		Swift-XRT	00081046001	5500	2015-11-30
13	UGC 12348	*NuSTAR*	60001147002	26702	2014-12-09
		XMM-*Newton*	0743010501	35700	2014-12-09
		Chandra	23719	2090	2020-11-25
14	2MASX J02420381+0510061	*NuSTAR*	60363003002	19800	2017-07-13
		XMM-*Newton*	0802200401	23000	2017-07-13
15	ESO 234-50	*NuSTAR*	60760005002	32271	2021-05-22
		Chandra	23814	20060	2021-03-14
16	NGC 2273	*NuSTAR*	60001064002	23230	2014-03-23
		XMM-Newton	0140950701	12551	2003-03-17
			0140951001	13016	2003-09-05
			0140950901	7857	2003-04-20
		Chandra	19377	10070	2017-08-17
17	FRL 265	*NuSTAR*	60360009002	29420	2019-06-10
		XMM-*Newton*	0903040501	23000	2022-04-23
18	MRK 231	*NuSTAR*	80302608002	82057	2017-10-19
			60002025002	41061	2012-08-26
			90102001002	31787	2015-04-02
			90102001006	30521	2015-05-28
			60002025004	28555	2013-05-09
			90102001004	28379	2015-04-19
19	PG 1211+143	*NuSTAR*	60001100002	111437	2014-02-18
			91001637002	83886	2024-12-01
			6000110000	74886	2014-07-07
			60001100005	64429	2014-04-09
			60001100004	48948	2014-04-08
20	MRK 376	*NuSTAR*	60160288002	24174	2015-04-07
		Swift-XRT	00081006001	2300	2015-04-07
			00081006002	3200	2015-04-08
21	NGC 7378	*NuSTAR*	60464202002	20301	2018-12-22
		Swift-XRT	00087196008	3700	2018-01-01
			00087196009	1300	2018-01-11
			00088600001	3300	2018-12-22
			00088600002	2800	2018-22-23
22	2MASX J11462959+7421289	*NuSTAR*	60061214002	22831	2013-12-10
		Swift-XRT	00080060001	5900	2013-12-07
23	SWIFT J2006.5+5619	*NuSTAR*	60061355002	21370	2014-06-30
		Swift-XRT	00080690001	5400	2014-07-01
24	2MASX J06363227-2034532	*NuSTAR*	60061069002	21436	2023-09-06
		Swift-XRT	00080375001	5900	2023-09-08

Table 2 *continued*

Table 2 *(continued)*

Index	Name	Telescope	Obs ID	Exposure (s)	Obs Date
25	2MASX J09034285-7414170	*NuSTAR*	60160346002	17038	2015-11-26
		Swift-XRT	00081040001	820	2015-11-26
			00081040002	3600	2015-11-27
			00081040003	1600	2015-12-02
26	2MASX J00091156-0036551	*NuSTAR*	60061002002	23533	2015-08-01
		Swift-XRT	00080001001	4100	2015-08-01

Table 3. Best-fit parameters as obtained from the spectral analysis of the 26 sources using `MyTorus`, `Borus02` and `UXCLUMPY`. The details of the fit parameters are given at the end of the table.

Parameter	`MyTorus`	`Borus02`	`UXCLUMPY`
	MRK 1073		
χ^2/dof	113/88	114/90	110/86
kT	$0.66^{+0.08}_{-0.05}$	$0.66^{+0.08}_{-0.08}$	$0.66^{+0.04}_{-0.04}$
Γ	$2.44^{+u}_{-0.32}$	$2.50^{+u}_{-0.32}$	$1.93^{+0.36}_{-0.36}$
norm $\times 10^{-2}$	$0.11^{+0.14}_{-0.07}$	$3.50^{+7.15}_{-2.04}$	$0.44^{+1.10}_{-0.35}$
c_f	...	$0.65^{+0.04}_{-0.06}$	...
CTKcover	...	...	$0.60^{+u}_{-0.19}$
TORsigma	...	...	$27.83^{+26.95}_{-}$
$N_{H,los}$	$2.44^{+u}_{-0.78}$	$5.88^{+u}_{-2.41}$	$3.16^{+7.84}_{-1.04}$
$N_{H,avg}$	$5.99^{+u}_{-0.37}$	$5.75^{+u}_{-1.95}$	...
$f_s \times 10^{-2}$	$2.35^{+4.77}_{-1.27}$	$0.15^{+0.98}_{-0.12}$	$4.66^{+9.66}_{-2.65}$
A_{90}	1.00*	...	...
A_0	1.00*	...	...
c_{nus}	$1.14^{+0.29}_{-0.23}$	$1.17^{+0.28}_{-0.23}$	$1.15^{+0.28}_{-0.23}$
c_{xmm1}	$0.92^{+0.28}_{-0.40}$	$0.81^{+0.48}_{-0.38}$	$0.90^{+0.38}_{-0.31}$
c_{xmm2}	$0.86^{+0.51}_{-0.38}$	$0.76^{+0.45}_{-0.36}$	$0.85^{+0.37}_{-0.29}$
c_{xmm3}	$0.78^{+0.48}_{-0.35}$	$0.68^{+0.41}_{-0.32}$	$0.77^{+0.34}_{-0.28}$
$F_{2-10\,keV}$	$1.08^{+0.14}_{-0.14} \times 10^{-13}$	$0.95^{+0.11}_{-0.11} \times 10^{-13}$	$0.92^{+0.12}_{-0.12} \times 10^{-13}$
$L_{2-10\,keV}$	$5.35^{+3.17}_{-3.17} \times 10^{42}$	$5.88^{+17.31}_{-u} \times 10^{43}$	$1.53^{+2.54}_{-1.32} \times 10^{43}$
	UGC 5101		
χ^2/dof	78/74	70/75	78/73
kT	...	...	...
Γ	$1.53^{+0.25}_{-u}$	$1.60^{+0.23}_{-u}$	$1.55^{+0.23}_{-0.19}$
norm $\times 10^{-2}$	$0.05^{+0.07}_{-0.02}$	$0.08^{+0.18}_{-0.05}$	$0.11^{+0.10}_{-0.04}$
c_f	...	$0.55^{+u}_{-0.06}$	...
CTKcover	...	...	$0.05^{+0.47}_{-u}$
TORsigma	...	...	$10.62^{+16.59}_{-u}$
$N_{H,los}$	$0.80^{+0.38}_{-0.16}$	$1.35^{+0.45}_{-0.48}$	$1.17^{+0.27}_{-0.34}$
$N_{H,avg}$	$2.43^{+u}_{-1.27}$	$2.95^{+u}_{-1.95}$	...
$f_s \times 10^{-2}$	$6.55^{+7.13}_{-4.16}$	$3.15^{+4.36}_{-1.97}$	5.00*
A_{90}	1.00*	...	...
A_0	1.00*	...	...
c_{nus1}	$0.88^{+0.18}_{-0.15}$	$0.88^{+0.17}_{-0.15}$	$1.00^{+0.19}_{-0.16}$
c_{nus2}	$0.96^{+0.17}_{-0.14}$	$0.96^{+0.17}_{-0.15}$	$0.94^{+0.17}_{-0.14}$
c_{nus2}	$0.95^{+0.17}_{-0.14}$	$0.96^{+0.17}_{-0.14}$	$0.93^{+0.17}_{-0.14}$
c_{chan}	$0.32^{+0.15}_{-0.11}$	$0.34^{+0.15}_{-0.07}$	$0.34^{+0.17}_{-0.14}$
$F_{2-10\,keV}$	$2.50^{+0.17}_{-0.17} \times 10^{-13}$	$2.67^{+0.18}_{-0.18} \times 10^{-13}$	$2.36^{+0.16}_{-0.16} \times 10^{-13}$

Table 3 *continued*

Table 3 *(continued)*

Parameter	MyTorus	Borus02	UXCLUMPY
$L_{2-10\,keV}$	$8.03^{+0.95}_{-0.95} \times 10^{42}$	$1.41^{+0.16}_{-0.16} \times 10^{43}$	$2.01^{+0.10}_{-0.08} \times 10^{43}$
NGC 7674			
χ^2/dof	190/132	218/133	213/133
kT	$0.32^{+0.10}_{-0.04}$	$0.20^{+0.07}_{-0.02}$	$0.24^{+0.03}_{-0.02}$
Γ	$1.70^{+0.11}_{-0.11}$	$1.90^{+0.26}_{-0.10}$	$2.10^{+0.09}_{-0.16}$
norm $\times 10^{-2}$	$0.02^{+0.07}_{-0.02}$	$0.10^{+0.18}_{-0.05}$	$0.18^{+0.11}_{-0.09}$
c_f	...	1.00(p)	...
CTKcover	...	...	$0.60^{+u}_{-0.03}$
TORsigma	...	...	$84.00^{+u}_{-3.16}$
$N_{H,los}$	$0.18^{+0.38}_{-0.16}$	$0.77^{+0.45}_{-0.48}$	$0.49^{+0.12}_{-0.14}$
$N_{H,avg}$	$1.93^{+1.32}_{-U}$	$2.34^{+1.37}_{-0.69}$	...
$f_s \times 10^{-2}$	$23.68^{+7.13}_{-4.16}$	$3.37^{+4.36}_{-1.97}$	$238.99^{+201.76}_{-92.78}$
A_{90}	<11.32	...	...
A_0	$7.41^{+4.39}_{-3.95}$	...	...
c_{nus1}	$0.97^{+0.18}_{-0.15}$	$0.98^{+0.17}_{-0.15}$	$0.97^{+0.08}_{-0.08}$
c_{xmm}	$0.67^{+0.15}_{-0.11}$	$0.57^{+0.15}_{-0.07}$	$0.66^{+0.10}_{-0.11}$
$F_{2-10\,keV}$	$6.32^{+0.29}_{-0.29} \times 10^{-13}$	$6.71^{+0.29}_{-0.29} \times 10^{-13}$	$7.08^{+0.29}_{-0.29} \times 10^{-13}$
$L_{2-10\,keV}$	$1.79^{+0.16}_{-0.16} \times 10^{42}$	$9.71^{+0.50}_{-0.50} \times 10^{42}$	$7.62^{+0.43}_{-0.42} \times 10^{42}$
IC 2227			
χ^2/dof	192/141	160/136	163/136
kT	$0.65^{+0.06}_{-0.06}$	$0.20^{+0.07}_{-0.08}$	$0.62^{+0.06}_{-0.08}$
Γ	$1.83^{+0.06}_{-0.12}$	$2.12^{+0.24}_{-0.29}$	$1.94^{+0.20}_{-0.20}$
norm $\times 10^{-2}$	$0.05^{+0.01}_{-0.01}$	$0.24^{+0.11}_{-0.06}$	$0.15^{+0.12}_{-0.06}$
c_f	...	1.00(p)	...
CTKcover	...	...	$0.60^{+u}_{-0.33}$
TORsigma	...	...	<30.20
$N_{H,los} \times 10^{24}$	$0.42^{+0.07}_{-0.05}$	$0.65^{+0.07}_{-0.12}$	$0.59^{+0.11}_{-0.09}$
$N_{H,avg} \times 10^{24}$	$1.26^{+0.42}_{-0.27}$	$1.35^{+0.30}_{-0.53}$	...
$f_s \times 10^{-2}$	$2.26^{+0.68}_{-0.54}$	$0.90^{+0.90}_{-0.41}$	$2.54^{+2.02}_{-1.20}$
A_{90}	$6.49^{+4.77}_{-3.94}$	...	...
A_0	<0.94	...	...
c_{nus}	$1.04^{+0.12}_{-0.11}$	$1.04^{+0.12}_{-0.11}$	$1.04^{+0.12}_{-0.11}$
c_{xmm}	$0.87^{+0.11}_{-0.09}$	$0.90^{+0.12}_{-0.11}$	$0.90^{+0.12}_{-0.11}$
$F_{2-10\,keV}$	$3.65^{+0.16}_{-0.16} \times 10^{-13}$	$3.66^{+0.16}_{-0.16} \times 10^{-13}$	$3.75^{+0.16}_{-0.16} \times 10^{-13}$
$L_{2-10\,keV}$	$5.01^{+0.30}_{-0.30} \times 10^{42}$	$6.45^{+0.38}_{-0.38} \times 10^{42}$	$1.00^{+0.37}_{-0.16} \times 10^{43}$
ESO 362-8			
χ^2/dof	107/115	108/114	110/114
kT	$0.54^{+0.07}_{-0.06}$	$0.51^{+0.06}_{-0.05}$	$0.51^{+0.07}_{-0.06}$
Γ	$2.19^{+0.28}_{-0.29}$	$1.93^{+0.50}_{-0.41}$	$2.32^{+0.34}_{-0.75}$
norm $\times 10^{-2}$	$1.04^{+1.14}_{-0.99}$	$0.17^{+1.11}_{-0.13}$	$1.09^{+4.00}_{-0.98}$
c_f	...	$0.58^{+0.02}_{-0.03}$	...

Table 3 *continued*

Table 3 *(continued)*

Parameter	MyTorus	Borus02	UXCLUMPY
CTKcover	...	...	0.60(p)
TORsigma	...	...	$56.35^{+20.49}_{-56.32}$
$N_{H,los} \times 10^{24}$	$6.74^{+0.43}_{-5.20}$	$2.31^{+1.69}_{-0.72}$	$2.96^{+2.88}_{-0.95}$
$N_{H,avg} \times 10^{24}$	$4.47^{+u}_{-2.40}$	$5.75^{+u}_{-2.87}$	...
$f_s \times 10^{-2}$	$0.10^{+0.24}_{-0.06}$	$0.48^{+0.95}_{-0.27}$	$1.21^{+5.06}_{-0.89}$
A_0	1.00(f)	...	...
A_{90}	$0.18^{+1.46}_{-0.07}$	...	...
c_{nus}	$1.06^{+0.25}_{-0.20}$	$1.05^{+0.24}_{-0.20}$	$1.07^{+0.25}_{-0.21}$
c_{xmm1}	$0.95^{+0.52}_{-0.34}$	$1.18^{+0.48}_{-0.36}$	$1.04^{+0.39}_{-0.30}$
c_{xmm2}	$0.92^{+0.48}_{-0.22}$	$1.16^{+0.44}_{-0.38}$	$1.02^{+0.37}_{-0.28}$
$F_{2-10\,keV}$	$9.25^{+0.79}_{-0.79} \times 10^{-14}$	$8.00^{+0.71}_{-0.71} \times 10^{-14}$	$8.52^{+0.75}_{-0.75} \times 10^{-14}$
$L_{2-10\,keV}$	$1.31^{+1.00}_{-1.00} \times 10^{43}$	$2.52^{+0.61}_{-0.61} \times 10^{43}$	$9.61^{+1.24}_{-1.23} \times 10^{42}$
ESO 406-4			
χ^2/dof	58/65	59/66	59/66
kT	$0.46^{+0.11}_{-0.13}$	$0.45^{+0.11}_{-0.13}$	$0.46^{+0.11}_{-0.16}$
Γ	$1.51^{+0.85}_{-u}$	$1.49^{+0.26}_{-u}$	$1.72^{+0.45}_{-0.34}$
norm $\times 10^{-2}$	$0.02^{+0.22}_{-0.02}$	$0.02^{+0.09}_{-0.01}$	$0.05^{+18}_{-0.04}$
c_f	...	$0.90^{+u}_{-0.78}$	...
CTKcover	...	...	>0.03
TORsigma	...	...	$34.38^{+u}_{-23.83}$
$N_{H,los} \times 10^{24}$	$1.06^{+0.87}_{-0.53}$	$1.34^{+0.85}_{-0.40}$	$1.16^{+0.56}_{-0.35}$
$N_{H,avg} \times 10^{24}$	$1.01^{+8.98}_{-0.99}$	$1.00^{+u}_{-0.51}$	...
$f_s \times 10^{-2}$	$5.74^{+10.33}_{-5.39}$	$7.42^{+4.27}_{-4.41}$	$11.18^{+66.18}_{-7.96}$
A_0	$1.00^{+53.35}_{-u}$	...	...
A_{90}	>2.16	...	...
c_{nus1}	$0.91^{+0.34}_{-0.25}$	$0.91^{+0.34}_{-0.25}$	$0.91^{+0.32}_{-0.25}$
c_{nus2}	$2.27^{+0.65}_{-0.44}$	$2.27^{+0.65}_{-0.43}$	$2.26^{+0.64}_{-0.43}$
c_{xmm}	$0.64^{+0.32}_{-0.23}$	$0.63^{+0.30}_{-0.22}$	$0.67^{+0.31}_{-0.23}$
$F_{2-10\,keV}$	$1.49^{+0.12}_{-0.97} \times 10^{-13}$	$1.50^{+0.22}_{-1.50} \times 10^{-13}$	$1.45^{+1.82}_{-0.11} \times 10^{-13}$
$L_{2-10\,keV}$	$2.28^{+0.30}_{-0.30} \times 10^{42}$	$1.79^{+0.30}_{-0.30} \times 10^{42}$	$3.94^{+0.25}_{-0.24} \times 10^{42}$
2MFGC 13496			
χ^2/dof	50/36	50/37	56/37
kT	–	–	–
Γ	$1.59^{+0.39}_{-u}$	$1.54^{+0.33}_{-u}$	$1.55^{+0.50}_{-0.16}$
norm $\times 10^{-2}$	$0.09^{+0.29}_{-0.04}$	$0.11^{+0.24}_{-0.05}$	$0.07^{+0.22}_{-0.04}$
c_f	...	0.10(f)	...
CTKcover	...	...	$0.25^{+0.26}_{-u}$
TORsigma	...	...	$6.99^{+44.20}_{-u}$
$N_{H,los} \times 10^{24}$	$0.73^{+0.27}_{-0.19}$	$1.15^{+0.34}_{-0.25}$	$0.59^{+0.20}_{-0.08}$
$N_{H,avg} \times 10^{24}$	$0.02^{+0.05}_{-u}$	$0.05^{+0.15}_{-u}$	...
$f_s \times 10^{-2}$	$0.59^{+1.03}_{-0.50}$	$0.40^{+0.66}_{-0.18}$	$1.72^{+2.51}_{-1.17}$

Table 3 *continued*

Table 3 *(continued)*

Parameter	MyTorus	Borus02	UXCLUMPY
A_0	$1.01^{+3.75}_{-u}$	...	...
A_{90}	<1.63	...	...
c_{nus}	$1.16^{+0.20}_{-0.17}$	$1.16^{+0.20}_{-0.17}$	$1.16^{+0.19}_{-0.16}$
c_{xmm}	$0.93^{+0.23}_{-0.10}$	$0.97^{+0.24}_{-0.20}$	$0.90^{+0.20}_{-0.18}$
$F_{2-10\,keV}$	$3.74^{+0.29}_{-1.94} \times 10^{-13}$	$3.74^{+0.46}_{-2.69} \times 10^{-13}$	$3.83^{+0.37}_{-2.77} \times 10^{-13}$
$L_{2-10\,keV}$	$1.56^{+0.12}_{-0.12} \times 10^{43}$	$2.08^{+0.15}_{-0.15} \times 10^{43}$	$1.38^{+0.16}_{-0.19} \times 10^{43}$
2MASX J03585442+1026033			
χ^2/dof	357/318	368/320	361/320
kT	$0.33^{+0.26}_{-0.06}$	$0.30^{+0.08}_{-0.05}$	$0.30^{+0.10}_{-0.05}$
Γ	$1.40^{+1.20}_{-u}$	1.40(p)	$1.40^{+0.09}_{-0.04}$
norm $\times 10^{-2}$	$0.06^{+0.01}_{-0.01}$	$0.06^{+0.01}_{-0.01}$	$0.24^{+0.06}_{-0.06}$
c_f	...	$0.70^{+u}_{-0.39}$	...
CTKcover	...	...	$0.014^{+0.030}_{-u}$
TORsigma	...	...	$1.80^{+0.84}_{-0.72}$
$N_{H,los} \times 10^{24}$	$0.11^{+0.01}_{-0.01}$	$0.11^{+0.08}_{-0.07}$	$0.10^{+0.01}_{-0.01}$
$N_{H,avg} \times 10^{24}$	$0.40^{+0.75}_{-0.35}$	$0.11^{+0.18}_{-0.07}$	...
$f_s \times 10^{-2}$	$1.49^{+0.36}_{-0.28}$	$1.49^{+0.37}_{-0.53}$	1.00(f)
A_0	$1.19^{+1.42}_{-u}$	...	...
A_{90}	<1.17	...	...
c_{nus}	$0.97^{+0.05}_{-0.06}$	$0.98^{+0.06}_{-0.06}$	$0.97^{+0.06}_{-0.06}$
c_{xmm1}	$1.21^{+0.08}_{-0.07}$	$1.18^{+0.07}_{-0.07}$	$1.21^{+0.08}_{-0.07}$
c_{xmm2}	$0.54^{+0.07}_{-0.07}$	$0.53^{+0.07}_{-0.06}$	$0.54^{+0.07}_{-0.07}$
c_{chan}	$0.79^{+0.06}_{-0.05}$	$0.76^{+0.05}_{-0.05}$	$0.78^{+0.06}_{-0.05}$
$F_{2-10\,keV}$	$2.29^{+0.41}_{-0.57} \times 10^{-12}$	$2.36^{+0.05}_{-0.07} \times 10^{-12}$	$2.29^{+0.20}_{-0.09} \times 10^{-12}$
$L_{2-10\,keV}$	$8.31^{+0.19}_{-0.19} \times 10^{42}$	$8.89^{+0.20}_{-0.20} \times 10^{42}$	$3.43^{+0.14}_{-0.25} \times 10^{43}$
M 58			
χ^2/dof	2466/2095	2497/2095	2643/2097
kT	$0.65^{+0.03}_{-0.03}$	$0.61^{+0.04}_{-0.05}$	$0.61^{+0.04}_{-0.04}$
Γ	$1.91^{+0.02}_{-0.03}$	$1.85^{+0.01}_{-0.01}$	$1.81^{+0.01}_{-0.01}$
norm $\times 10^{-2}$	$0.03^{+0.01}_{-0.02}$	$0.23^{+0.06}_{-0.05}$	$0.29^{+0.02}_{-0.01}$
c_f	...	1.00(p)	...
CTKcover	...	...	–
TORsigma	...	...	$2.92^{+1.65}_{-1.92}$
$N_{H,los} \times 10^{24}$	$0.010^{+0.002}_{-u}$	$0.00006^{+0.00005}_{-0.00004}$	$0.0001^{+0.0000}_{-u}$
$N_{H,avg} \times 10^{24}$	$0.09^{+0.03}_{-0.03}$	$0.17^{+0.02}_{-0.03}$	...
$f_s \times 10^{-2}$	...	...	...
A_0	$49.90^{+105.27}_{-20.86}$	...	...
A_{90}	1.00(f)	...	...
c_{nus}	$1.00^{+0.02}_{-0.02}$	$1.00^{+0.02}_{-0.03}$	$1.00^{+0.02}_{-0.02}$
c_{xmm}	$0.51^{+0.01}_{-0.01}$	$0.50^{+0.01}_{-0.02}$	$0.49^{+0.01}_{-0.01}$
c_{xmm}	$0.80^{+0.02}_{-0.02}$	$0.79^{+0.03}_{-0.01}$	$0.78^{+0.02}_{-0.02}$

Table 3 *continued*

Table 3 *(continued)*

Parameter	MyTorus	Borus02	UXCLUMPY
c_{chan}	$0.55^{+0.02}_{-0.02}$	$0.54^{+0.03}_{-0.02}$	$0.53^{+0.02}_{-0.02}$
$F_{2-10\,keV}$	$7.91^{+0.06}_{-1.73} \times 10^{-12}$	$7.88^{+0.08}_{-0.10} \times 10^{-12}$	$8.06^{+0.74}_{-0.14} \times 10^{-12}$
$L_{2-10\,keV}$	$5.25^{+0.33}_{-0.33} \times 10^{40}$	$4.10^{+0.02}_{-0.02} \times 10^{41}$	$5.43^{+0.05}_{-0.09} \times 10^{41}$
3C 371			
χ^2/dof	203/173	203/176	203/176
kT	$0.37^{+0.49}_{-0.14}$	0.37(p)	0.33(f)
Γ	$1.80^{+0.20}_{-0.21}$	$1.77^{+0.12}_{-0.13}$	$1.85^{+0.11}_{-0.07}$
norm $\times 10^{-2}$	$0.06^{+0.03}_{-0.03}$	$0.05^{+0.02}_{-0.02}$	$0.13^{+0.08}_{-0.03}$
c_f	...	1.00(p)	...
CTKcover	...	...	0.60(p)
TORsigma	...	...	$1.91^{+3.21}_{-u}$
$N_{H,los} \times 10^{24}$	$0.022^{+0.006}_{-0.006}$	$0.034^{+0.010}_{-0.018}$	$0.025^{+0.001}_{-0.010}$
$N_{H,avg} \times 10^{24}$	$0.50^{+2.22}_{-0.49}$	$0.54^{+0.78}_{-0.49}$	...
$f_s \times 10^{-2}$	$41.30^{+25.72}_{-14.42}$	$41.40^{+17.85}_{-11.12}$	$99.30^{+44.74}_{-87.14}$
A_0	$3.11^{+78.22}_{-20.86}$	...	...
A_{90}	<76.13	...	...
c_{nus}	$1.03^{+0.11}_{-0.10}$	$1.03^{+0.11}_{-0.10}$	$1.03^{+0.11}_{-0.10}$
c_{chan}	$0.80^{+0.10}_{-0.09}$	$0.80^{+0.10}_{-0.09}$	$0.80^{+0.08}_{-0.10}$
$F_{2-10\,keV}$	$2.55^{+0.39}_{-0.19} \times 10^{-12}$	$2.43^{+0.06}_{-0.34} \times 10^{-12}$	$2.53^{+0.22}_{-1.11} \times 10^{-12}$
$L_{2-10\,keV}$	$1.45^{+0.05}_{-0.05} \times 10^{43}$	$1.36^{+0.04}_{-0.04} \times 10^{43}$	$2.40^{+0.06}_{-0.07} \times 10^{43}$
IC 1198			
χ^2/dof	438/338	425/340	443/340
kT	–	–	–
Γ	$1.96^{+0.06}_{-0.06}$	$2.13^{+0.05}_{-0.10}$	$1.97^{+0.10}_{-0.06}$
norm $\times 10^{-2}$	$0.25^{+0.03}_{-0.03}$	$0.40^{+0.06}_{-0.08}$	$1.25^{+0.12}_{-0.10}$
c_f	...	1.00(p)	...
CTKcover	...	...	<0.03
TORsigma	...	...	$1.87^{+0.78}_{-0.84}$
$N_{H,los} \times 10^{24}$	$0.11^{+0.01}_{-0.01}$	$0.21^{+0.02}_{-0.02}$	$0.11^{+0.01}_{-0.01}$
$N_{H,avg} \times 10^{24}$	10.00(p)	$3.02^{+2.11}_{-1.02}$	...
$f_s \times 10^{-2}$	$3.64^{+0.61}_{-0.50}$	$2.31^{+0.56}_{-0.32}$	1.00(f)
A_0	$3.11^{+5.89}_{-u}$	...	...
A_{90}	$0.99^{+1.00}_{-0.67}$	...	...
c_{nus}	$1.03^{+0.06}_{-0.05}$	$1.02^{+0.06}_{-0.05}$	$1.03^{+0.06}_{-0.05}$
c_{xmm}	$0.30^{+0.02}_{-0.02}$	$0.30^{+0.02}_{-0.02}$	$0.31^{+0.02}_{-0.02}$
$F_{2-10\,keV}$	$3.42^{+0.10}_{-0.10} \times 10^{-12}$	$3.47^{+0.09}_{-0.11} \times 10^{-12}$	$3.47^{+0.91}_{-0.01} \times 10^{-12}$
$L_{2-10\,keV}$	$1.72^{+0.04}_{-0.04} \times 10^{43}$	$2.27^{+0.06}_{-0.06} \times 10^{43}$	$8.88^{+0.05}_{-0.06} \times 10^{43}$
2MASX J09261742-8421330			
C-stat/dof	265/265	264/266	267/266
kT	–	–	–
Γ	$1.98^{+0.11}_{-0.14}$	$1.95^{+0.10}_{-0.08}$	$1.92^{+0.06}_{-0.15}$

Table 3 *continued*

Table 3 *(continued)*

Parameter	MyTorus	Borus02	UXCLUMPY
norm $\times 10^{-2}$	$0.25^{+0.10}_{-0.05}$	$0.21^{+0.07}_{-0.03}$	$0.29^{+0.05}_{-0.08}$
c_f	...	1.00(p)	...
CTKcover	...	...	<0.50
TORsigma	...	...	$83.42^{+u}_{-77.44}$
$N_{H,los} \times 10^{24}$	$0.014^{+0.010}_{-u}$	$0.021^{+0.034}_{-u}$	$0.013^{+0.013}_{-u}$
$N_{H,avg} \times 10^{24}$	$0.95^{+1.67}_{-0.28}$	$0.91^{+0.31}_{-0.43}$	...
$f_s \times 10^{-2}$	–	–	–
A_0	$2.62^{+3.45}_{-u}$	...	...
A_{90}	<1.46	...	...
c_{nus}	$0.99^{+0.04}_{-0.04}$	$0.99^{+0.04}_{-0.04}$	$0.99^{+0.04}_{-0.04}$
c_{xrt}	$0.90^{+0.06}_{-0.11}$	$0.91^{+0.13}_{-0.10}$	$0.90^{+0.11}_{-0.14}$
$F_{2-10\,keV}$	$5.61^{+0.06}_{-4.89} \times 10^{-12}$	$5.38^{+0.16}_{-0.16} \times 10^{-12}$	$5.31^{+-0.04}_{-5.24} \times 10^{-12}$
$L_{2-10\,keV}$	$4.73^{+0.56}_{-0.56} \times 10^{43}$	$1.57^{+0.04}_{-0.04} \times 10^{43}$	$8.32^{+0.45}_{-0.46} \times 10^{43}$
UGC 12348			
χ^2/dof	760/772	751/774	733/773
kT	$0.71^{+0.11}_{-0.14}$	0.70(f)	0.70(f)
Γ	$1.60^{+0.03}_{-0.03}$	$1.77^{+0.04}_{-0.04}$	$1.92^{+0.05}_{-0.09}$
norm $\times 10^{-2}$	$0.10^{+0.01}_{-0.01}$	$0.16^{+0.02}_{-0.01}$	$0.26^{+0.03}_{-0.04}$
c_f	...	1.00(p)	...
CTKcover	...	...	0.6(p)
TORsigma	...	...	$23.64^{+40.36}_{-08.30}$
$N_{H,los} \times 10^{24}$	$0.023^{+0.002}_{-0.001}$	$0.044^{+0.018}_{-0.015}$	$0.027^{+0.027}_{-0.025}$
$N_{H,avg} \times 10^{24}$	$0.018^{+0.015}_{-0.008}$	0.01(p)	...
$f_s \times 10^{-2}$	1.00(f)	$1.01^{+0.30}_{-0.30}$	$3.10^{+0.06}_{-0.01}$
A_0	$16.92^{+13.16}_{-6.07}$	...	...
A_{90}	<3.69	...	...
c_{nus}	$1.03^{+0.05}_{-0.05}$	$1.02^{+0.05}_{-0.05}$	$1.03^{+0.05}_{-0.05}$
c_{xmm}	$1.06^{+0.05}_{-0.05}$	$1.05^{+0.05}_{-0.05}$	$1.04^{+0.05}_{-0.05}$
c_{chan}	$0.54^{+0.07}_{-0.07}$	$0.46^{+0.05}_{-0.05}$	$0.46^{+0.07}_{-0.06}$
$F_{2-10\,keV}$	$4.21^{+1.34}_{-0.03} \times 10^{-12}$	$4.56^{+0.15}_{-0.14} \times 10^{-12}$	$4.61^{+0.06}_{-2.26} \times 10^{-12}$
$L_{2-10\,keV}$	$6.56^{+0.09}_{-0.09} \times 10^{42}$	$8.30^{+0.10}_{-0.10} \times 10^{42}$	$1.09^{+0.25}_{-0.69} \times 10^{43}$
2MASX J02420381+0510061			
χ^2/dof	188/218	187/217	192/218
kT	–	–	–
Γ	$1.83^{+0.03}_{-0.08}$	$1.81^{+0.08}_{-0.07}$	$1.83^{+0.08}_{-0.08}$
norm $\times 10^{-2}$	$0.16^{+0.03}_{-0.05}$	$0.20^{+0.04}_{-0.04}$	$7.44^{+1.13}_{-1.04}$
c_f	...	0.1(p)	...
CTKcover	...	...	0.6(p)
TORsigma	...	...	$0.15^{+1.48}_{-0.06}$
$N_{H,los} \times 10^{24}$	$0.81^{+0.15}_{-0.14}$	$1.29^{+0.25}_{-0.22}$	$0.98^{+0.60}_{-0.25}$
$N_{H,avg} \times 10^{24}$	0.01(p)	0.01(p)	...

Table 3 *continued*

Table 3 *(continued)*

Parameter	MyTorus	Borus02	UXCLUMPY
$f_s \times 10^{-2}$	$17.78^{+8.43}_{-5.39}$	$12.27^{+6.07}_{-2.88}$	1.00(f)
A_0	1.00 (f)	...	...
A_{90}	1.00(f)	...	...
c_{nus}	$1.00^{+0.14}_{-0.12}$	$1.00^{+0.14}_{-0.12}$	$0.99^{+0.13}_{-0.12}$
c_{xmm}	$5.03^{+0.71}_{-0.60}$	$5.13^{+0.74}_{-0.62}$	$4.89^{+0.68}_{-0.57}$
$F_{2-10\,keV}$	$1.15^{+0.06}_{-0.18} \times 10^{-12}$	$1.14^{+0.03}_{-0.18} \times 10^{-12}$	$1.16^{+0.07}_{-0.08} \times 10^{-12}$
$L_{2-10\,keV}$	$6.08^{+0.67}_{-0.67} \times 10^{43}$	$8.80^{+0.95}_{-0.94} \times 10^{43}$	$4.88^{+1.25}_{-2.96} \times 10^{44}$
ESO 234-50			
χ^2/dof	137/132	136/132	137/131
kT	–	–	–
Γ	$1.71^{+0.05}_{-0.05}$	$1.69^{+0.11}_{-0.06}$	$1.80^{+0.08}_{-0.08}$
norm $\times 10^{-2}$	$0.090^{+0.06}_{-0.03}$	$0.094^{+0.05}_{-0.03}$	$0.099^{+0.095}_{-0.011}$
c_f	...	$0.12^{+0.69}_{-u}$	...
CTKcover	...	...	$0.22^{+0.15}_{-u}$
TORsigma	...	...	$6.86^{+22.32}_{-6.66}$
$N_{H,los} \times 10^{24}$	$0.22^{+0.05}_{-0.05}$	$0.32^{+0.07}_{-0.05}$	$0.20^{+0.02}_{-0.03}$
$N_{H,avg} \times 10^{24}$	<0.50	1.00(p)	...
$f_s \times 10^{-2}$	$4.53^{+3.02}_{-1.88}$	$4.15^{+1.01}_{-1.47}$	$7.99^{+0.03}_{-0.08}$
A_0	1.00 (f)	...	...
A_{90}	1.00(f)	...	...
c_{nus}	$1.04^{+0.08}_{-0.07}$	$1.04^{+0.08}_{-0.07}$	$1.04^{+0.08}_{-0.07}$
c_{xmm}	$0.33^{+0.05}_{-0.05}$	$0.33^{+0.05}_{-0.05}$	$0.33^{+0.05}_{-0.05}$
$F_{2-10\,keV}$	$1.45^{+0.87}_{-0.43} \times 10^{-12}$	$1.45^{+0.06}_{-0.14} \times 10^{-12}$	$1.45^{+1.05}_{-0.16} \times 10^{-12}$
$L_{2-10\,keV}$	$6.17^{+0.26}_{-0.26} \times 10^{41}$	$6.85^{+0.29}_{-0.29} \times 10^{41}$	$4.45^{+0.21}_{-0.32} \times 10^{41}$
NGC 2273			
χ^2/dof	195/161	194/168	207/168
kT	$0.35^{+0.18}_{-0.08}$	$0.36^{+0.11}_{-0.06}$	$0.34^{+0.09}_{-0.05}$
Γ	$1.47^{+0.22}_{-u}$	$1.46^{+0.18}_{-u}$	$1.16^{+0.17}_{-0.09}$
norm $\times 10^{-2}$	$0.043^{+0.049}_{-0.009}$	$0.21^{+0.11}_{-0.02}$	$0.23^{+0.04}_{-0.04}$
c_f	...	$0.56^{+0.25}_{-0.09}$	...
CTKcover	...	...	$0.03^{+0.03}_{-0.02}$
TORsigma	...	...	<1.00
$N_{H,los} \times 10^{24}$	$0.37^{+0.11}_{-0.06}$	$0.31^{+0.11}_{-0.13}$	$0.35^{+0.05}_{-0.07}$
$N_{H,avg} \times 10^{24}$	$3.30^{+u}_{-1.90}$	$0.43^{+0.23}_{-0.14}$	...
$f_s \times 10^{-2}$	$5.09^{+0.03}_{-0.02}$	$0.85^{+0.22}_{-0.28}$	1.00(f)
A_0	1.00(f)	...	...
A_{90}	1.00(f)	...	...
c_{nus}	$1.04^{+0.10}_{-0.12}$	$1.04^{+0.12}_{-0.11}$	$1.03^{+0.11}_{-0.10}$
c_{xmm}	$0.94^{+0.13}_{-0.12}$	$0.95^{+0.13}_{-0.12}$	$0.94^{+0.13}_{-0.11}$
$c_{chandra}$	$0.93^{+0.20}_{-0.17}$	$0.97^{+0.17}_{-0.16}$	$0.97^{+0.17}_{-0.14}$
$F_{2-10\,keV}$	$1.02^{+0.06}_{-0.75} \times 10^{-12}$	$1.02^{+0.11}_{-0.24} \times 10^{-12}$	$1.02^{+1.29}_{-0.02} \times 10^{-12}$

Table 3 *continued*

Table 3 *(continued)*

Parameter	MyTorus	Borus02	UXCLUMPY
$L_{2-10\,keV}$	$2.31^{+0.40}_{-0.40} \times 10^{41}$	$1.07^{+0.32}_{-0.32} \times 10^{42}$	$3.98^{+1.25}_{-0.69} \times 10^{42}$
FRL 265			
χ^2/dof	180/171	177/173	173/170
kT	$0.18^{+0.30}_{-0.07}$	–	$0.15^{+0.56}_{-u}$
Γ	$1.97^{+0.07}_{-0.07}$	$1.87^{+0.40}_{-0.15}$	$1.80^{+0.08}_{-0.06}$
norm $\times 10^{-2}$	$0.10^{+0.02}_{-0.01}$	$0.08^{+0.30}_{-0.06}$	$0.10^{+0.70}_{-0.30}$
c_f	...	1.00(p)	...
CTKcover	...	...	$0.36^{+0.08}_{-0.05}$
TORsigma	...	...	$8.01^{+2.25}_{-7.18}$
$N_{H,los} \times 10^{24}$	$0.010^{+0.004}_{-u}$	<0.06	$0.01^{+0.23}_{-0.06}$
$N_{H,avg} \times 10^{24}$	$2.00^{+2.95}_{-0.99}$	$1.51^{+0.34}_{-0.31}$	...
$f_s \times 10^{-2}$	–	–	–
A_0	1.00(f)	...	...
A_{90}	1.00(f)	...	...
c_{nus}	$1.06^{+0.09}_{-0.08}$	$1.06^{+0.09}_{-0.08}$	$1.05^{+0.09}_{-0.08}$
c_{xmm}	$0.79^{+0.07}_{-0.06}$	$0.83^{+0.07}_{-0.06}$	$0.78^{+0.07}_{-0.06}$
$F_{2-10\,keV}$	$2.53^{+0.18}_{-0.16} \times 10^{-12}$	$2.59^{+0.18}_{-0.15} \times 10^{-12}$	$2.48^{+-0.17}_{-2.48} \times 10^{-12}$
$L_{2-10\,keV}$	$3.32^{+0.20}_{-0.20} \times 10^{43}$	$4.12^{+2.59}_{-2.59} \times 10^{43}$	$1.42^{+0.73}_{-0.64} \times 10^{43}$
MRK 231			
χ^2/dof	556/539	557/541	558/540
kT	–	–	–
Γ	$1.51^{+0.07}_{-0.07}$	$1.52^{+0.21}_{-u}$	$1.67^{+0.10}_{-0.09}$
norm $\times 10^{-2}$	$0.023^{+0.006}_{-0.004}$	$0.025^{+0.003}_{-0.002}$	$0.043^{+0.013}_{-0.012}$
c_f	...	$0.30^{+u}_{-0.18}$	...
CTKcover	...	...	<0.54
TORsigma	...	...	$50.90^{+u}_{-40.04}$
$N_{H,los} \times 10^{24}$	$0.06^{+0.03}_{-0.02}$	$0.10^{+0.02}_{-0.02}$	$0.07^{+0.02}_{-0.02}$
$N_{H,avg} \times 10^{24}$	$0.24^{+0.53}_{-0.15}$	$1.62^{+1.24}_{-u}$	...
$f_s \times 10^{-2}$	1.00(F)	1.00(f)	1.00(f)
A_0	1.00(f)	...	...
A_{90}	1.00(f)	...	...
c_{nus1}	$0.94^{+0.10}_{-0.11}$	$0.94^{+0.10}_{-0.11}$	$0.94^{+0.10}_{-0.11}$
c_{nus2}	$1.00^{+0.10}_{-0.11}$	$1.00^{+0.10}_{-0.11}$	$1.00^{+0.10}_{-0.11}$
c_{nu3}	$0.98^{+0.11}_{-0.10}$	$0.98^{+0.11}_{-0.10}$	$0.98^{+0.11}_{-0.10}$
c_{nu4}	$1.04^{+0.11}_{-0.10}$	$1.04^{+0.11}_{-0.10}$	$1.04^{+0.11}_{-0.10}$
c_{nu5}	$1.07^{+0.10}_{-0.09}$	$1.07^{+0.10}_{-0.09}$	$1.07^{+0.10}_{-0.09}$
c_{nu6}	$0.90^{+0.10}_{-0.09}$	$0.90^{+0.10}_{-0.09}$	$0.90^{+0.10}_{-0.09}$
c_{nu7}	$0.82^{+0.10}_{-0.09}$	$0.82^{+0.10}_{-0.09}$	$0.82^{+0.10}_{-0.09}$
c_{nu8}	$0.91^{+0.10}_{-0.09}$	$0.91^{+0.10}_{-0.09}$	$0.91^{+0.10}_{-0.09}$
c_{nu9}	$0.90^{+0.10}_{-0.09}$	$0.90^{+0.10}_{-0.09}$	$0.90^{+0.10}_{-0.09}$
c_{nu10}	$1.25^{+0.11}_{-0.09}$	$1.25^{+0.11}_{-0.09}$	$1.25^{+0.11}_{-0.09}$

Table 3 *continued*

Table 3 *(continued)*

Parameter	MyTorus	Borus02	UXCLUMPY
c_{nu11}	$1.20^{+0.10}_{-0.09}$	$1.20^{+0.10}_{-0.09}$	$1.20^{+0.10}_{-0.09}$
$F_{2-10\,keV}$	$7.61^{+4.20}_{-7.54} \times 10^{-13}$	$7.37^{+0.43}_{-0.47} \times 10^{-13}$	$7.27^{+0.30}_{-2.25} \times 10^{-13}$
$L_{2-10\,keV}$	$4.78^{+0.10}_{-0.10} \times 10^{42}$	$5.12^{+0.11}_{-0.11} \times 10^{42}$	$2.95^{+0.43}_{-0.46} \times 10^{43}$
PG 1211+143			
χ^2/dof	1616/1647	1654/1648	1662/1647
kT	–	–	–
Γ	$2.42^{+0.08}_{-0.06}$	$2.22^{+0.03}_{-0.06}$	$2.17^{+0.01}_{-0.03}$
norm $\times 10^{-2}$	$0.39^{+0.07}_{-0.05}$	$0.25^{+0.02}_{-0.04}$	$0.30^{+0.03}_{-0.02}$
c_f	...	1.00(p)	...
CTKcover	...	...	$0.30^{+0.09}_{-0.05}$
TORsigma	...	...	$84.00^{+u}_{-7.42}$
$N_{H,los} \times 10^{24}$	$0.04^{+0.01}_{-0.01}$	$0.04^{+0.01}_{-0.02}$	$0.14^{+0.05}_{-0.04}$
$N_{H,avg} \times 10^{24}$	$1.99^{+0.21}_{-0.22}$	$1.51^{+0.31}_{-0.33}$	...
$f_s \times 10^{-2}$	1.00(F)	1.00(f)	1.00(f)
A_0	$3.89^{+1.13}_{-0.85}$	...	...
A_{90}	1.00(f)	...	...
c_{nus1}	$0.98^{+0.03}_{-0.03}$	$0.99^{+0.03}_{-0.03}$	$0.99^{+0.03}_{-0.03}$
c_{nus2}	$1.33^{+0.04}_{-0.04}$	$1.34^{+0.04}_{-0.04}$	$1.34^{+0.05}_{-0.04}$
c_{nu3}	$1.32^{+0.05}_{-0.04}$	$1.32^{+0.04}_{-0.04}$	$1.32^{+0.05}_{-0.04}$
c_{nu4}	$1.48^{+0.04}_{-0.04}$	$1.49^{+0.04}_{-0.04}$	$1.49^{+0.04}_{-0.04}$
c_{nu5}	$1.41^{+0.04}_{-0.04}$	$1.41^{+0.04}_{-0.04}$	$1.41^{+0.04}_{-0.04}$
c_{nu6}	$1.03^{+0.03}_{-0.03}$	$1.03^{+0.03}_{-0.03}$	$1.03^{+0.03}_{-0.03}$
c_{nu7}	$0.99^{+0.03}_{-0.03}$	$0.99^{+0.03}_{-0.03}$	$0.99^{+0.03}_{-0.03}$
$F_{2-10\,keV}$	$3.52^{+0.05}_{-0.07} \times 10^{-12}$	$3.59^{+0.06}_{-0.07} \times 10^{-12}$	$3.64^{+0.21}_{-0.51} \times 10^{-12}$
$L_{2-10\,keV}$	$7.68^{+0.07}_{-0.07} \times 10^{43}$	$7.09^{+0.06}_{-0.06} \times 10^{43}$	$4.88^{+0.11}_{-0.15} \times 10^{43}$
Mrk 376			
C-stat/dof	201/199	198/201	210/205
kT	$0.23^{+0.03}_{-0.03}$	$0.20^{+0.04}_{-0.02}$	$0.19^{+0.02}_{-0.01}$
Γ	$1.90^{+0.10}_{-0.10}$	$1.64^{+0.06}_{-0.08}$	$1.70^{+0.06}_{-0.06}$
norm $\times 10^{-2}$	$0.18^{+0.03}_{-0.03}$	$0.10^{+0.01}_{-0.01}$	$0.87^{+0.64}_{-0.54}$
c_f	...	1.00(p)	...
CTKcover	...	...	$0.45^{+0.04}_{-0.05}$
TORsigma	...	...	$1.50^{+2.87}_{-0.74}$
$N_{H,los} \times 10^{24}$	$0.010^{+0.001}_{-u}$	$0.084^{+0.017}_{-0.020}$	$0.0056^{+0.0007}_{-0.0005}$
$N_{H,avg} \times 10^{24}$	$2.46^{+2.79}_{-2.33}$	$1.11^{+1.59}_{-0.78}$	...
$f_s \times 10^{-2}$	1.00(f)	1.00(f)	1.00(f)
A_0	<3.06	...	...
A_{90}	$1.64^{+0.84}_{-1.39}$	...	...
c_{nus}	$1.01^{+0.06}_{-0.06}$	$1.01^{+0.06}_{-0.06}$	$1.01^{+0.06}_{-0.06}$
c_{xrt}	$0.84^{+0.08}_{-0.08}$	$0.33^{+0.09}_{-0.09}$	$0.88^{+0.09}_{-0.08}$
$F_{2-10\,keV}$	$4.58^{+0.15}_{-0.32} \times 10^{-12}$	$4.56^{+0.13}_{-0.39} \times 10^{-12}$	$4.58^{+0.12}_{-0.82} \times 10^{-12}$

Table 3 *continued*

Table 3 *(continued)*

Parameter	MyTorus	Borus02	UXCLUMPY
$L_{2-10\,keV}$	$2.93^{+0.12}_{-0.12} \times 10^{43}$	$3.33^{+0.09}_{-0.09} \times 10^{43}$	$2.62^{+1.24}_{-1.83} \times 10^{44}$
NGC 7378			
C-stat/dof	87/103	89/104	96/106
kT	–	–	–
Γ	$2.22^{+0.25}_{-0.22}$	$1.98^{+0.13}_{-0.05}$	$1.80^{+0.11}_{-0.06}$
norm $\times 10^{-2}$	$0.31^{+0.15}_{-0.12}$	$0.20^{+0.08}_{-0.04}$	$0.48^{+0.21}_{-0.17}$
c_f	...	1.00(p)	...
CTKcover	...	...	$0.46^{+0.01}_{-0.03}$
TORsigma	...	...	<1.17
$N_{H,los} \times 10^{24}$	$0.094^{+0.023}_{-0.026}$	$0.12^{+0.04}_{-0.03}$	$0.050^{+0.029}_{-0.025}$
$N_{H,avg} \times 10^{24}$	$3.13^{+4.61}_{-0.99}$	$2.57^{+2.00}_{-1.06}$	...
$f_s \times 10^{-2}$	$0.80^{+0.64}_{-0.50}$	$1.03^{+0.74}_{-0.71}$	1.00(f)
A_0	$7.11^{+6.94}_{-5.47}$	...	...
A_{90}	$0.23^{+2.00}_{-u}$	...	...
c_{nus}	$1.09^{+0.09}_{-0.08}$	$1.10^{+0.09}_{-0.08}$	$1.10^{+0.09}_{-0.08}$
c_{xrt}	$0.55^{+0.09}_{-0.08}$	$0.55^{+0.09}_{-0.09}$	$0.53^{+0.08}_{-0.08}$
$F_{2-10\,keV}$	$2.80^{+0.15}_{-0.22} \times 10^{-12}$	$2.82^{+0.05}_{-0.21} \times 10^{-12}$	$2.87^{+2.33}_{-0.72} \times 10^{-12}$
$L_{2-10\,keV}$	$1.03^{+0.04}_{-0.04} \times 10^{42}$	$9.46^{+0.37}_{-0.37} \times 10^{41}$	$2.97^{+0.78}_{-1.29} \times 10^{42}$
2MASX J11462959+7421289			
C-stat/dof	107/96	108/96	116/96
kT	–	–	–
Γ	$1.75^{+0.17}_{-0.09}$	$1.70^{+0.18}_{-0.09}$	$1.74^{+0.08}_{-0.06}$
norm $\times 10^{-2}$	$0.083^{+0.032}_{-0.012}$	$0.070^{+0.029}_{-0.012}$	$0.86^{+0.89}_{-0.44}$
c_f	...	1.00(p)	...
CTKcover	...	...	$0.36^{+0.05}_{-0.17}$
TORsigma	...	...	$0.79^{+1.71}_{-0.44}$
$N_{H,los} \times 10^{24}$	$0.010^{+0.003}_{-u}$	$0.013^{+0.060}_{-0.010}$	$0.045^{+0.007}_{-0.010}$
$N_{H,avg} \times 10^{24}$	$0.20^{+1.29}_{-u}$	$0.11^{+0.65}_{-u}$	...
$f_s \times 10^{-2}$	1.00(f)	1.00(f)	1.00(f)
A_0	1.00(f)	...	...
A_{90}	1.00(f)	...	...
c_{nus}	$1.03^{+0.08}_{-0.08}$	$1.03^{+0.09}_{-0.08}$	$1.03^{+0.09}_{-0.08}$
c_{xrt}	$0.86^{+0.16}_{-0.11}$	$0.84^{+0.18}_{-0.16}$	$0.62^{+0.12}_{-0.11}$
$F_{2-10\,keV}$	$2.79^{+0.03}_{-0.21} \times 10^{-12}$	$2.75^{+0.02}_{-0.46} \times 10^{-12}$	$2.85^{+0.12}_{-1.37} \times 10^{-12}$
$L_{2-10\,keV}$	$2.27^{+0.09}_{-0.09} \times 10^{43}$	$2.08^{+0.11}_{-0.11} \times 10^{43}$	$2.62^{+0.15}_{-0.09} \times 10^{43}$
SWIFT J2006.5+5619			
C-stat/dof	84/74	108/96	116/96
kT	–	–	–
Γ	$1.55^{+0.15}_{-0.11}$	$1.94^{+0.17}_{-0.20}$	$1.93^{+0.12}_{-0.16}$
norm $\times 10^{-2}$	$0.070^{+0.017}_{-0.024}$	$0.19^{+0.14}_{-0.10}$	$0.22^{+0.09}_{-0.08}$
c_f	...	1.00(p)	...

Table 3 *continued*

Table 3 *(continued)*

Parameter	MyTorus	Borus02	UXCLUMPY
CTKcover	...	...	$0.60^{+u}_{-0.42}$
TORsigma	...	...	84.00(p)
$N_{H,los} \times 10^{24}$	$0.15^{+0.04}_{-0.03}$	$0.31^{+0.09}_{-0.11}$	$0.19^{+0.04}_{-0.05}$
$N_{H,avg} \times 10^{24}$	$0.20^{+0.20}_{-0.16}$	$3.24^{+u}_{-1.46}$	...
$f_s \times 10^{-2}$	1.00(f)	1.00(f)	1.00(f)
A_0	1.00(f)	...	...
A_{90}	1.00(f)	...	...
c_{nus}	$0.99^{+0.09}_{-0.08}$	$0.99^{+0.09}_{-0.08}$	$0.99^{+0.09}_{-0.08}$
c_{xrt}	$0.83^{+0.19}_{-0.17}$	$1.04^{+0.18}_{-0.16}$	$1.04^{+0.21}_{-0.19}$
$F_{2-10\,keV}$	$1.67^{+0.06}_{-0.26} \times 10^{-12}$	$1.80^{+0.33}_{-1.46} \times 10^{-12}$	$1.69^{+0.11}_{-0.21} \times 10^{-12}$
$L_{2-10\,keV}$	$1.51^{+0.07}_{-0.07} \times 10^{43}$	$2.69^{+0.15}_{-0.15} \times 10^{43}$	$2.82^{+0.12}_{-0.11} \times 10^{43}$
2MASX J06363227-2034532			
C-stat/dof	44/45	44/45	43/45
kT	$0.23^{+0.25}_{-0.08}$	$0.22^{+0.10}_{-0.06}$	$0.20^{+0.08}_{-0.05}$
Γ	$1.40^{+1.2}_{-u}$	$1.40^{+1.2}_{-u}$	$1.59^{+0.28}_{-0.23}$
norm $\times 10^{-2}$	$0.11^{+0.12}_{-0.09}$	$0.17^{+0.04}_{-0.03}$	$0.15^{+0.29}_{-0.05}$
c_f	...	0.10(p)	...
CTKcover	...	...	$0.60^{+u}_{-0.50}$
TORsigma	...	...	$28.07^{+29.03}_{-25.09}$
$N_{H,los} \times 10^{24}$	$0.92^{+0.11}_{-0.11}$	$1.48^{+0.21}_{-0.17}$	$0.86^{+0.22}_{-0.10}$
$N_{H,avg} \times 10^{24}$	0.01(p)	0.01(p)	...
$f_s \times 10^{-2}$	$1.09^{+1.16}_{-0.51}$	$0.78^{+0.72}_{-0.74}$	$7.85^{+13.32}_{-0.05}$
A_0	1.00(f)	...	...
A_{90}	1.00(f)	...	...
c_{nus}	$1.00^{+0.12}_{-0.12}$	$1.00^{+0.11}_{-0.08}$	$1.02^{+0.13}_{-0.12}$
c_{xrt}	$0.64^{+0.28}_{-0.24}$	$0.68^{+0.25}_{-0.21}$	$0.62^{+0.24}_{-0.22}$
$F_{2-10\,keV}$	$4.83^{+1.39}_{-1.54} \times 10^{-13}$	$4.82^{+1.06}_{-2.40} \times 10^{-13}$	$4.92^{+2.23}_{-3.31} \times 10^{-13}$
$L_{2-10\,keV}$	$5.03^{+0.33}_{-0.33} \times 10^{43}$	$7.94^{+0.52}_{-0.52} \times 10^{43}$	$5.37^{+0.65}_{-0.72} \times 10^{43}$
2MASX J09034285-7414170			
C-stat/dof	89/101	99/101	99/100
kT	–	–	–
Γ	$2.35^{+u}_{-0.53}$	$1.73^{+0.40}_{-0.15}$	$1.73^{+0.32}_{-0.22}$
norm $\times 10^{-2}$	$0.40^{+0.67}_{-0.33}$	$0.10^{+0.30}_{-0.06}$	$0.13^{+0.21}_{-0.06}$
c_f	...	1.00(p)	...
CTKcover	...	...	$0.30^{+0.30}_{-u}$
TORsigma	...	...	$84.00^{+u}_{-37.92}$
$N_{H,los} \times 10^{24}$	$0.40^{+0.22}_{-0.21}$	$0.49^{+0.21}_{-0.17}$	$0.34^{+0.17}_{-0.16}$
$N_{H,avg} \times 10^{24}$	$3.50^{+5.69}_{-2.27}$	$1.32^{+0.74}_{-0.86}$	...
$f_s \times 10^{-2}$	$0.14^{+1.22}_{-u}$	$0.67^{+1.38}_{-0.48}$	1.00(f)
A_0	$9.89^{+13.60}_{-u}$	...	...
A_{90}	$1.59^{+u}_{-2.32}$	...	...

Table 3 *continued*

Table 3 *(continued)*

Parameter	MyTorus	Borus02	UXCLUMPY
c_{nus}	$1.00^{+0.12}_{-0.11}$	$1.01^{+0.13}_{-0.11}$	$1.01^{+0.13}_{-0.11}$
c_{xrt}	$0.74^{+0.23}_{-0.20}$	$0.83^{+0.27}_{-0.24}$	$0.84^{+0.26}_{-0.24}$
$F_{2-10\,keV}$	$1.02^{+0.16}_{-0.18} \times 10^{-12}$	$1.01^{+0.07}_{-0.77} \times 10^{-12}$	$1.02^{+0.03}_{-0.73} \times 10^{-12}$
$L_{2-10\,keV}$	$3.96^{+0.40}_{-0.40} \times 10^{43}$	$8.06^{+0.58}_{-0.58} \times 10^{43}$	$1.09^{+0.40}_{-0.06} \times 10^{43}$
2MASX J00091156-0036551			
C-stat/dof	53/48	53/50	53/49
kT	–	–	–
Γ	$1.54^{+0.25}_{-u}$	$1.84^{+0.40}_{-0.15}$	$1.61^{+0.21}_{-0.23}$
norm $\times 10^{-2}$	$0.05^{+0.15}_{-0.06}$	$0.09^{+0.30}_{-0.06}$	$0.12^{+0.02}_{-0.05}$
c_f	...	1.00(p)	...
CTKcover	...	...	$0.13^{+0.24}_{-0.06}$
TORsigma	...	...	<9.71
$N_{H,los} \times 10^{24}$	$0.29^{+0.06}_{-0.09}$	$0.45^{+0.16}_{-0.16}$	$0.27^{+0.12}_{-0.09}$
$N_{H,avg} \times 10^{24}$	0.01(p)	$1.80^{+1.32}_{-0.92}$	...
$f_s \times 10^{-2}$	$1.23^{+1.62}_{-1.23}$	$0.67^{+1.72}_{-0.48}$	1.00(f)
A_0	1.00(p)	...	...
A_{90}	$0.98^{+12.95}_{-u}$	...	...
c_{nus}	$0.88^{+0.13}_{-0.12}$	$1.01^{+0.13}_{-0.11}$	$0.88^{+0.13}_{-0.12}$
c_{xrt}	$0.83^{+0.26}_{-0.22}$	$0.83^{+0.24}_{-0.21}$	$0.84^{+0.23}_{-0.20}$
$F_{2-10\,keV}$	$7.84^{+1.00}_{-1.54} \times 10^{-13}$	$6.95^{+0.96}_{-3.66} \times 10^{-13}$	$7.77^{+10.58}_{-2.24} \times 10^{-13}$
$L_{2-10\,keV}$	$3.17^{+0.22}_{-0.22} \times 10^{43}$	$3.90^{+0.31}_{-0.31} \times 10^{43}$	$7.26^{+0.35}_{-0.36} \times 10^{43}$

NOTE—χ^2/dof: χ^2 divided by degrees of freedom (total fit statistics).
C-stat/dof: Cash statistics divided by degrees of freedom (total fit statistics).
kT: `mekal` model temperature in units of keV.
Γ: Power law photon index.
norm: the main power-law normalization (in units of photons cm^{-2} s^{-1} keV^{-1} $\times$ 10^{-2}, measured at 1 keV).
c_f: Covering factor of the torus.
`CTKcover`: Covering factor of the inner ring of clouds.
`TORsigma`: Cloud dispersion factor, computed with `UXCLUMPY`.
$N_{H,los}$: line-of-sight torus hydrogen column density, in units of 10^{24} cm^{-2}.
$N_{H,avg}$: Average torus hydrogen column density, in units of 10^{24} cm^{-2}.
f_s: Fraction of scattered continuum.
A_{90}: Relative weighs of the `MYTS` and `MYTL` component for $\theta_{obs} = 90°$.
A_0: Relative weighs of the `MYTS` and `MYTL` component for $\theta_{obs} = 00°$.
c: The cross-normalization constant between the instruments.
$F_{2-10\,keV}$: Observed flux in the 2–10 keV band with units of erg cm^{-2} s^{-1}.
$L_{2-10\,keV}$: Intrinsic luminosity in the 2–10 keV band with units of erg s^{-1}.
$*$: Indicates the parameter was frozen to this value during fitting.
u: The parameter is unconstrained.
p: The parameter is pegged.

B. SUPPLEMENTARY TABLES

We list in Tables 4 and 5 the derived bolometric luminosities, bolometric correction factors, and Eddington luminosities for the type 1 and type 2 AGN samples. The values illustrate the range of corrections applied from the intrinsic 2-10 keV luminosity, following the prescriptions described above.

Table 4. Bolometric luminosity, correction factor, and Eddington luminosity for type 1 sources.

Source name	$\log L_{bol}$	K_X	$\log L_{Edd}$
UGC 5101	44.46	14.36	46.46
IC 1198	45.21	18.37	45.62
MRK 231	44.64	14.95	46.05
PG 1211+143	44.90	16.09	46.71
MRK 376	45.88	28.64	46.33

Table 5. Bolometric luminosity, correction factor, and Eddington luminosity for type 2 sources.

Source name	$\log L_{bol}$	K_X	$\log L_{Edd}$
MRK 1073	44.27	12.12	45.89
NGC 7674	43.94	11.54	45.84
ESO 406−4	43.65	11.23	46.13
2MASX J03585442+1026033	44.66	13.47	45.86
M58	42.77	10.91	46.21
2MASX J09261742−8421330	45.15	17.03	45.21
ESO 234−50	42.69	10.90	44.15
NGC 2273	43.65	11.24	46.33
NGC 7378	43.52	11.15	43.60
2MASX J11462959+7421289	44.53	12.90	46.33
SWIFT J2006.5+5619	44.57	13.04	45.18
2MASX J06363227−2034532	44.90	14.85	46.55
2MASX J09034285−7414170	44.11	11.79	45.99
2MASX J00091156−0036551	45.07	16.23	46.65

C. BEST-FIT SPECTRA

The best-fitted unfolded spectra and the data-to-model residuals of 25 sources are presented in the following section. The modeling is carried out using `MyTorus` and presented in Fig. 14.

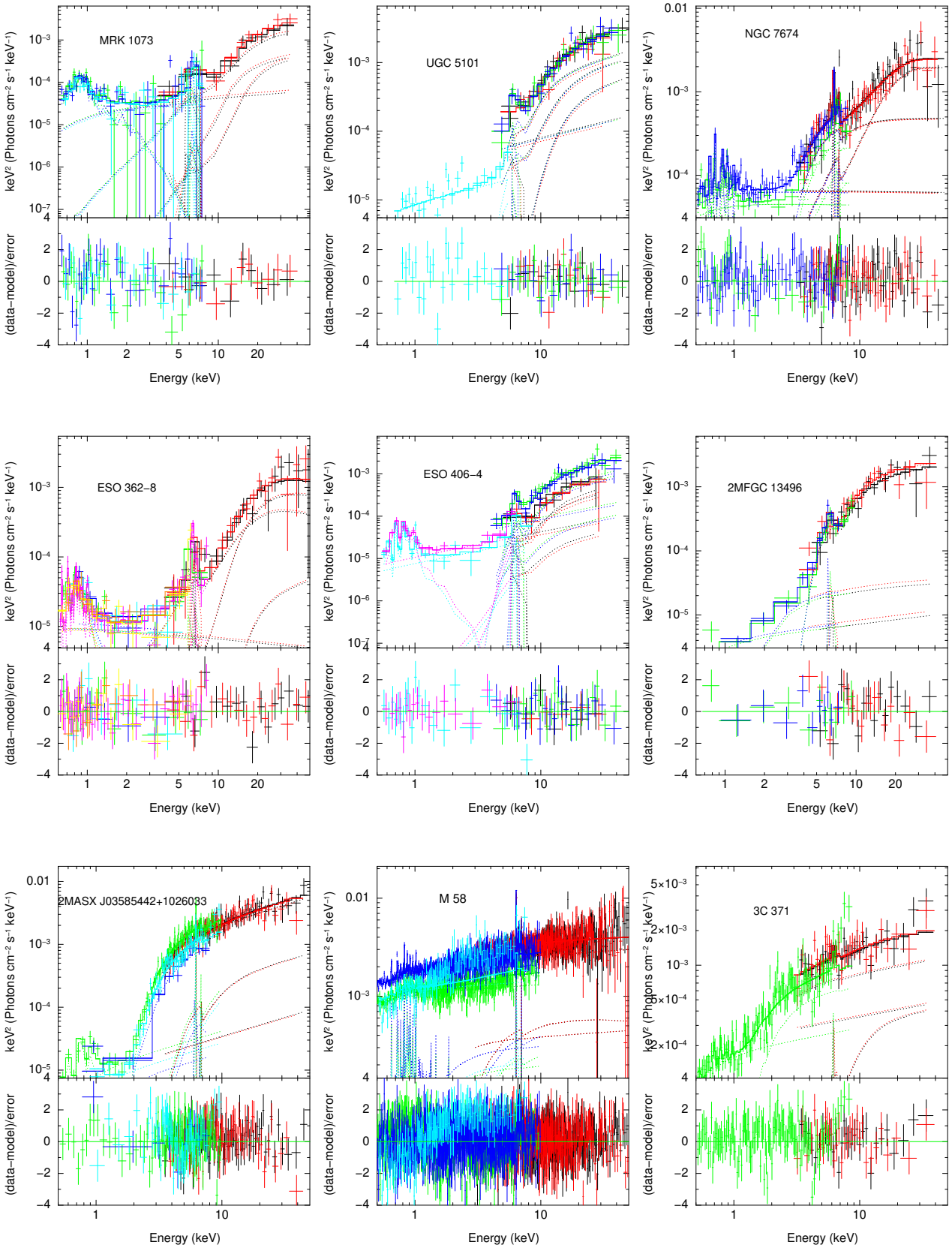
MRK 1073
UGC 5101
NGC 7674
ESO 362–8
ESO 406–4
2MFGC 13496
2MASX J03585442+1026033
M 58
3C 371
keV² (Photons cm⁻² s⁻¹ keV⁻¹)
(data−model)/error
Energy (keV)

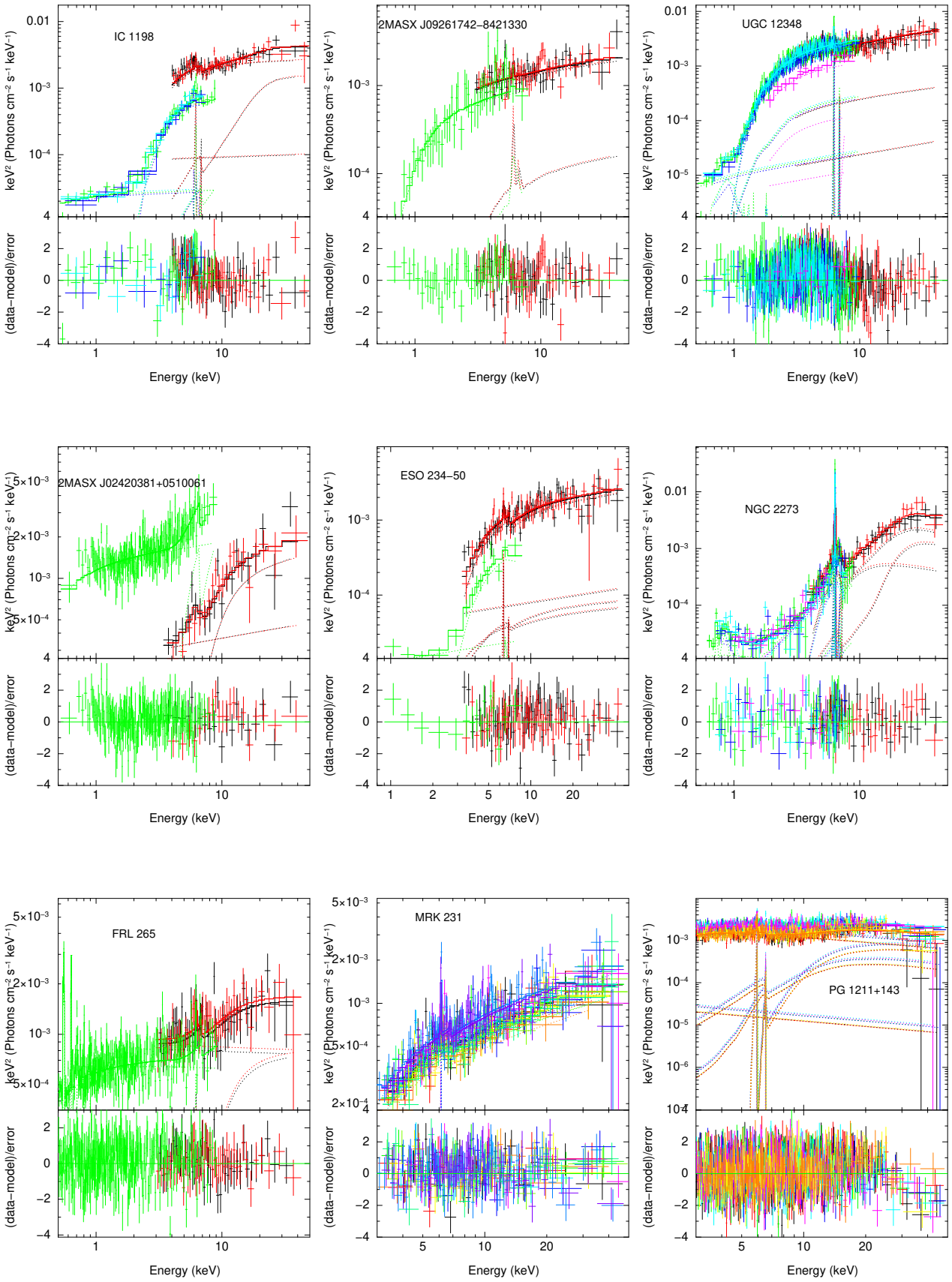
IC 1198
2MASX J09261742−8421330
UGC 12348
2MASX J02420381+0510061
ESO 234−50
NGC 2273
FRL 265
MRK 231
PG 1211+143
keV² (Photons cm⁻² s⁻¹ keV⁻¹)
(data−model)/error
Energy (keV)

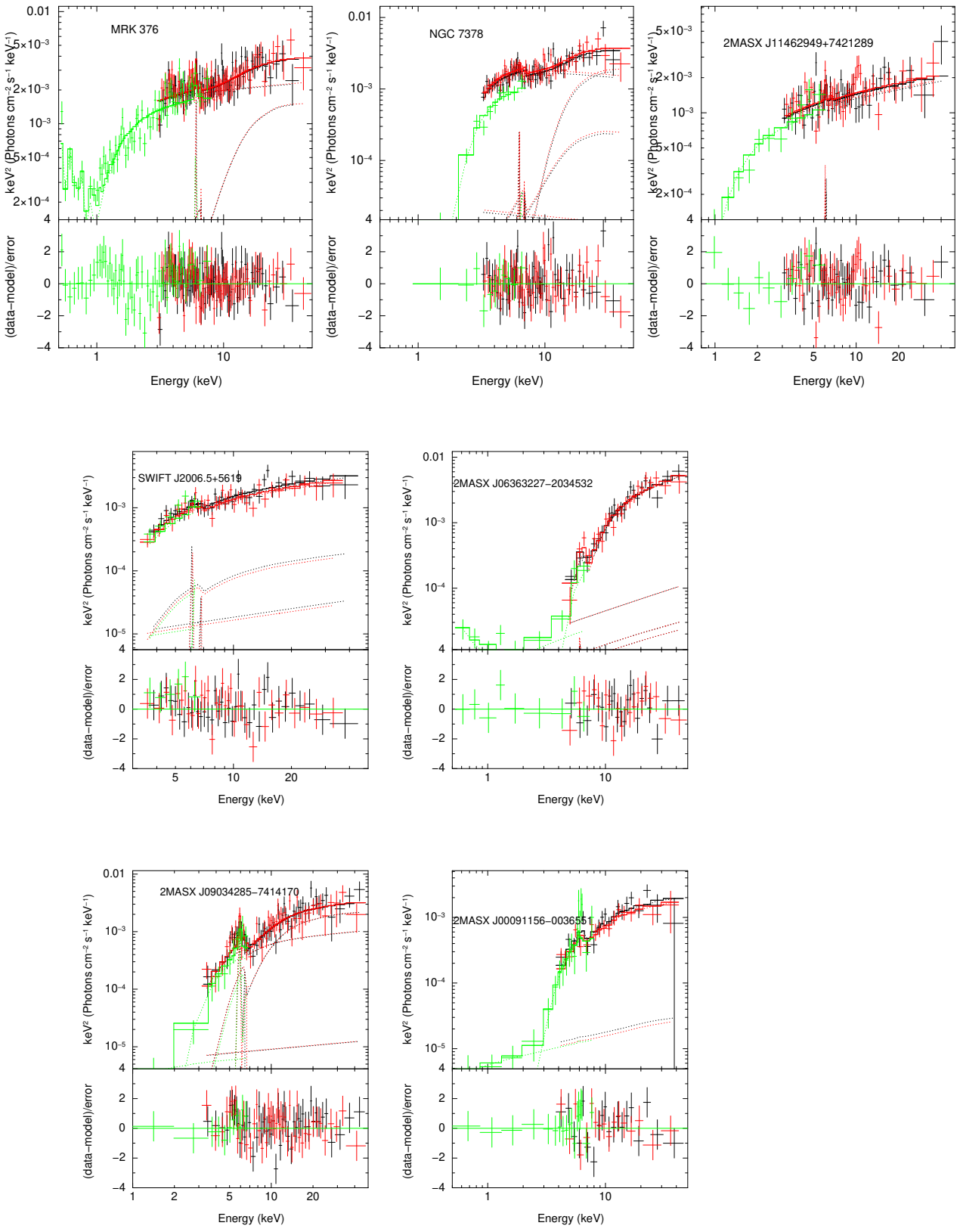

Figure 14. Best-fit unfolded spectra and residuals obtained with the `MyTorus` model for 25 sources. The source names are indicated in the plot legends.

REFERENCES

Ajello, M., Greiner, J., Sato, G., et al. 2008, ApJ, 689, 666, doi: 10.1086/592595

Akylas, A., Georgantopoulos, I., Ranalli, P., et al. 2016, A&A, 594, A73, doi: 10.1051/0004-6361/201628711

Alexander, D. M., Bauer, F. E., Brandt, W. N., et al. 2003, AJ, 126, 539, doi: 10.1086/376473

Ananna, T. T., Treister, E., Urry, C. M., et al. 2019, ApJ, 871, 240, doi: 10.3847/1538-4357/aafb77

Arnaud, K. A. 1996, in Astronomical Society of the Pacific Conference Series, Vol. 101, Astronomical Data Analysis Software and Systems V, ed. G. H. Jacoby & J. Barnes, 17

Asmus, D., Gandhi, P., Hönig, S. F., Smette, A., & Duschl, W. J. 2015, MNRAS, 454, 766, doi: 10.1093/mnras/stv1950

Baloković, M., Brightman, M., Harrison, F. A., et al. 2018, ApJ, 854, 42, doi: 10.3847/1538-4357/aaa7eb

Boorman, P. G., Gandhi, P., Buchner, J., et al. 2025, ApJ, 978, 118, doi: 10.3847/1538-4357/ad8236

Braito, V., Della Ceca, R., Piconcelli, E., et al. 2004, A&A, 420, 79, doi: 10.1051/0004-6361:20040061

Brightman, M., & Nandra, K. 2011, MNRAS, 413, 1206, doi: 10.1111/j.1365-2966.2011.18207.x

Brightman, M., Baloković, M., Stern, D., et al. 2015, ApJ, 805, 41, doi: 10.1088/0004-637X/805/1/41

Buchner, J., Brightman, M., Nandra, K., Nikutta, R., & Bauer, F. E. 2019a, A&A, 629, A16, doi: 10.1051/0004-6361/201834771

—. 2019b, A&A, 629, A16, doi: 10.1051/0004-6361/201834771

Buchner, J., Georgakakis, A., Nandra, K., et al. 2015, ApJ, 802, 89, doi: 10.1088/0004-637X/802/2/89

Burlon, D., Ajello, M., Greiner, J., et al. 2011, ApJ, 728, 58, doi: 10.1088/0004-637X/728/1/58

Burrows, D. N., Hill, J. E., Nousek, J. A., et al. 2005, SSRv, 120, 165, doi: 10.1007/s11214-005-5097-2

Campitiello, S., Celotti, A., Ghisellini, G., & Sbarrato, T. 2020, A&A, 640, A39, doi: 10.1051/0004-6361/201936218

Corral, A., Della Ceca, R., Caccianiga, A., et al. 2011, A&A, 530, A42, doi: 10.1051/0004-6361/201015227

Dasyra, K. M., Ho, L. C., Netzer, H., et al. 2011, ApJ, 740, 94, doi: 10.1088/0004-637X/740/2/94

Decarli, R., Dotti, M., Fontana, M., & Haardt, F. 2008, MNRAS, 386, L15, doi: 10.1111/j.1745-3933.2008.00451.x

Duras, F., Bongiorno, A., Ricci, F., et al. 2020, A&A, 636, A73, doi: 10.1051/0004-6361/201936817

Elitzur, M., & Shlosman, I. 2006, ApJL, 648, L101, doi: 10.1086/508158

Evans, P. A., Beardmore, A. P., Page, K. L., et al. 2009, MNRAS, 397, 1177, doi: 10.1111/j.1365-2966.2009.14913.x

Fruscione, A., McDowell, J. C., Allen, G. E., et al. 2006, in Society of Photo-Optical Instrumentation Engineers (SPIE) Conference Series, Vol. 6270, Observatory Operations: Strategies, Processes, and Systems, ed. D. R. Silva & R. E. Doxsey, 62701V, doi: 10.1117/12.671760

Fukazawa, Y., Hiragi, K., Mizuno, M., et al. 2011, ApJ, 727, 19, doi: 10.1088/0004-637X/727/1/19

Gabriel, C., Denby, M., Fyfe, D. J., et al. 2004, in Astronomical Society of the Pacific Conference Series, Vol. 314, Astronomical Data Analysis Software and Systems (ADASS) XIII, ed. F. Ochsenbein, M. G. Allen, & D. Egret, 759

Gandhi, P., Annuar, A., Lansbury, G. B., et al. 2017, MNRAS, 467, 4606, doi: 10.1093/mnras/stx357

Gaspari, M., & Sądowski, A. 2017, ApJ, 837, 149, doi: 10.3847/1538-4357/aa61a3

Gehrels, N., Chincarini, G., Giommi, P., et al. 2004, ApJ, 611, 1005, doi: 10.1086/422091

Gilli, R., Comastri, A., & Hasinger, G. 2007, A&A, 463, 79, doi: 10.1051/0004-6361:20066334

Guainazzi, M., Matt, G., & Perola, G. C. 2005, A&A, 444, 119, doi: 10.1051/0004-6361:20053643

Harrison, F. A., Craig, W. W., Christensen, F. E., et al. 2013, ApJ, 770, 103, doi: 10.1088/0004-637X/770/2/103

Hernández-García, L., Masegosa, J., González-Martín, O., & Márquez, I. 2015, A&A, 579, A90, doi: 10.1051/0004-6361/201526127

Jaffe, W., Meisenheimer, K., Röttgering, H. J. A., et al. 2004, Nature, 429, 47, doi: 10.1038/nature02531

Jana, A., Chatterjee, A., Chang, H.-K., et al. 2023, MNRAS, 524, 4670, doi: 10.1093/mnras/stad2140

Kammoun, E. S., Miller, J. M., Koss, M., et al. 2020, ApJ, 901, 161, doi: 10.3847/1538-4357/abb29f

Koss, M., Trakhtenbrot, B., Ricci, C., et al. 2017, ApJ, 850, 74, doi: 10.3847/1538-4357/aa8ec9

Koss, M. J., Assef, R., Baloković, M., et al. 2016, ApJ, 825, 85, doi: 10.3847/0004-637X/825/2/85

Koss, M. J., Ricci, C., Trakhtenbrot, B., et al. 2022, ApJS, 261, 2, doi: 10.3847/1538-4365/ac6c05

LaMassa, S. M., Yaqoob, T., Boorman, P. G., et al. 2019, ApJ, 887, 173, doi: 10.3847/1538-4357/ab552c

Leighly, K. M., Terndrup, D. M., Baron, E., et al. 2014, ApJ, 788, 123, doi: 10.1088/0004-637X/788/2/123

Marchesi, S., Ajello, M., Marcotulli, L., et al. 2018, ApJ, 854, 49, doi: 10.3847/1538-4357/aaa410

Marchesi, S., Ajello, M., Zhao, X., et al. 2019, ApJ, 872, 8, doi: 10.3847/1538-4357/aafbeb
Marchesi, S., Zhao, X., Torres-Albà, N., et al. 2022, ApJ, 935, 114, doi: 10.3847/1538-4357/ac80be
Matt, G., Bianchi, S., de Rosa, A., Grandi, P., & Perola, G. C. 2006, A&A, 445, 451, doi: 10.1051/0004-6361:20054013
Mejía-Restrepo, J. E., Trakhtenbrot, B., Koss, M. J., et al. 2022, ApJS, 261, 5, doi: 10.3847/1538-4365/ac6602
Murphy, K. D., & Yaqoob, T. 2009, MNRAS, 397, 1549, doi: 10.1111/j.1365-2966.2009.15025.x
Nasa High Energy Astrophysics Science Archive Research Center (Heasarc). 2014, HEAsoft: Unified Release of FTOOLS and XANADU, Astrophysics Source Code Library, record ascl:1408.004. http://ascl.net/1408.004
Nenkova, M., Sirocky, M. M., Nikutta, R., Ivezić, Ž., & Elitzur, M. 2008, ApJ, 685, 160, doi: 10.1086/590483
Oda, S., Tanimoto, A., Ueda, Y., et al. 2017, ApJ, 835, 179, doi: 10.3847/1538-4357/835/2/179
Osorio-Clavijo, N., González-Martín, O., Sánchez, S. F., et al. 2022, MNRAS, 510, 5102, doi: 10.1093/mnras/stab3752
Panagiotou, C., Walter, R., & Paltani, S. 2021, A&A, 653, A162, doi: 10.1051/0004-6361/202140379
Peterson, B. M., Ferrarese, L., Gilbert, K. M., et al. 2004, ApJ, 613, 682, doi: 10.1086/423269
Pfeifle, R. W., Ricci, C., Boorman, P. G., et al. 2022, ApJS, 261, 3, doi: 10.3847/1538-4365/ac5b65
Pizzetti, A., Torres-Albà, N., Marchesi, S., et al. 2025, ApJ, 979, 170, doi: 10.3847/1538-4357/ad9c64
Reeves, J. N., Lobban, A., & Pounds, K. A. 2018, ApJ, 854, 28, doi: 10.3847/1538-4357/aaa776
Ricci, C., Beckmann, V., Audard, M., & Courvoisier, T. J. L. 2010, A&A, 518, A47, doi: 10.1051/0004-6361/200912509
Ricci, C., Ueda, Y., Koss, M. J., et al. 2015, ApJL, 815, L13, doi: 10.1088/2041-8205/815/1/L13
Ricci, C., Trakhtenbrot, B., Koss, M. J., et al. 2017, ApJS, 233, 17, doi: 10.3847/1538-4365/aa96ad
Ricci, C., Privon, G. C., Pfeifle, R. W., et al. 2021, MNRAS, 506, 5935, doi: 10.1093/mnras/stab2052
Risaliti, G., Elvis, M., Fabbiano, G., et al. 2007, ApJL, 659, L111, doi: 10.1086/517884
Saha, T., Markowitz, A. G., & Buchner, J. 2022, MNRAS, 509, 5485, doi: 10.1093/mnras/stab3250
Sambruna, R. M., Eracleous, M., & Mushotzky, R. F. 1999, ApJ, 526, 60, doi: 10.1086/307981
Sengupta, D., Marchesi, S., Vignali, C., et al. 2023, A&A, 676, A103, doi: 10.1051/0004-6361/202245646
Silver, R., Torres-Albà, N., Zhao, X., et al. 2023, A&A, 675, A65, doi: 10.1051/0004-6361/202345980
—. 2022, ApJ, 940, 148, doi: 10.3847/1538-4357/ac9bf8
Strüder, L., Briel, U., Dennerl, K., et al. 2001, A&A, 365, L18, doi: 10.1051/0004-6361:20000066
Tanimoto, A., Ueda, Y., Odaka, H., et al. 2019, ApJ, 877, 95, doi: 10.3847/1538-4357/ab1b20
—. 2020, ApJ, 897, 2, doi: 10.3847/1538-4357/ab96bc
Tanimoto, A., Ueda, Y., Odaka, H., Yamada, S., & Ricci, C. 2022, ApJS, 260, 30, doi: 10.3847/1538-4365/ac5f59
Teng, S. H., Brandt, W. N., Harrison, F. A., et al. 2014, ApJ, 785, 19, doi: 10.1088/0004-637X/785/1/19
Tombesi, F., Meléndez, M., Veilleux, S., et al. 2015, Nature, 519, 436, doi: 10.1038/nature14261
Torres-Albà, N., Marchesi, S., Zhao, X., et al. 2023, A&A, 678, A154, doi: 10.1051/0004-6361/202345947
—. 2021, ApJ, 922, 252, doi: 10.3847/1538-4357/ac1c73
Treister, E., Urry, C. M., & Virani, S. 2009, ApJ, 696, 110, doi: 10.1088/0004-637X/696/1/110
Ueda, Y., Akiyama, M., Hasinger, G., Miyaji, T., & Watson, M. G. 2014, ApJ, 786, 104, doi: 10.1088/0004-637X/786/2/104
Verner, D. A., Ferland, G. J., Korista, K. T., & Yakovlev, D. G. 1996, ApJ, 465, 487, doi: 10.1086/177435
Weisskopf, M. C., Tananbaum, H. D., Van Speybroeck, L. P., & O'Dell, S. L. 2000, in Society of Photo-Optical Instrumentation Engineers (SPIE) Conference Series, Vol. 4012, X-Ray Optics, Instruments, and Missions III, ed. J. E. Truemper & B. Aschenbach, 2–16, doi: 10.1117/12.391545
Williams, D. R. A., Pahari, M., Baldi, R. D., et al. 2022, MNRAS, 510, 4909, doi: 10.1093/mnras/stab3310
Willingale, R., Starling, R. L. C., Beardmore, A. P., Tanvir, N. R., & O'Brien, P. T. 2013, MNRAS, 431, 394, doi: 10.1093/mnras/stt175
Wilms, J., Allen, A., & McCray, R. 2000, ApJ, 542, 914, doi: 10.1086/317016
Yamada, S., Ueda, Y., Tanimoto, A., et al. 2020, ApJ, 897, 107, doi: 10.3847/1538-4357/ab94b1
Yamada, S., Kawamuro, T., Mizumoto, M., et al. 2024, ApJS, 274, 8, doi: 10.3847/1538-4365/ad5961
Yaqoob, T. 2012, MNRAS, 423, 3360, doi: 10.1111/j.1365-2966.2012.21129.x
Yaqoob, T., Tatum, M. M., Scholtes, A., Gottlieb, A., & Turner, T. J. 2015, MNRAS, 454, 973, doi: 10.1093/mnras/stv2021
Zhao, X., Marchesi, S., Ajello, M., Baloković, M., & Fischer, T. 2020, ApJ, 894, 71, doi: 10.3847/1538-4357/ab879d
Zhao, X., Marchesi, S., Ajello, M., et al. 2021, A&A, 650, A57, doi: 10.1051/0004-6361/202140297